Femtosecond Laser Modification of Fe^{3+} doped Calcium Phosphates

A study of laser parameters on the densification of calcium phosphates for dental and orthopaedic applications.

Robert Mathieson

Submitted in accordance with the requirements for the degree of;

Doctor of Philosophy

The University of Leeds

School of Chemical and Process Engineering

July 2018

The candidate confirms that the work submitted is his/her own and that appropriate credit has been given where reference has been made to the work of others.

Acknowledgements

I would like to thank all those who have helped mentor and guide my way through the last few years. I would like to give special thanks to Dr. Billy Richards, Dr. James Addis and Dr. Antonios Anastasiou, who I could not quite have done without.

I'd also like to thank Claudio Amorese, Cesare Di Chio, Michele Panteleo, Francesco Tedeschi, Maria Caputo, and Zamira Kalemaj for being great hosts and company during my stay to utilise their facilities in Italy. Likewise up in Scotland, thanks to Tom Brown, Tom Edwards and Caroline Thompson.

I would of course also like to thank all my family and friends for their support, humour and for being generally quite distracting throughout. You all know who you are. Cheers.

Abstract

Calcium phosphate based biominerals are the main inorganic constituent of bone and teeth. Therefore, the processing of these minerals provides a unique solution for a bioactive, structural material which can be used inside the body instead of typical bioinert materials. Dental enamel, a highly crystalline calcium phosphate, is prone to acid erosion and wear, which affects all ages, an early sign of which is hypersensitivity. Calcium phosphate minerals also play an important role in bone restoration and growth, and with an increased ageing population the number of hip and knee replacement revision surgeries are becoming more common. In this study, the main objective was to investigate the use of femtosecond pulsed lasers for sintering and processing of modified calcium phosphate minerals in order to analyse the efficacy of these methods for interfacial bonding and adhesion to titanium implant materials and dental enamel.

Calcium phosphate minerals, specifically hydroxyapatite ($Ca_{10}(PO_4)_6OH_2$), were synthesised through the wet chemistry synthesis method, and were modified with the substitution of Fe^{3+} ions in various doping regimes. These materials were characterised via XRD, SEM, FTIR, Raman spectroscopy, UV-vis-NIR spectroscopy, particle size analysis and TGA/DSC.

The following materials where then irradiated with near infrared sources in a variety of pulse repetition rates ranging from single shot to 1GHz. Ablation thresholds of the materials were found to remain relatively constant despite the addition of Fe^{3+} impurities into the structure. And working in lower repetition rate regimes, did not allow for successful sintering of the materials, however, it

could be bonded to the titanium substrates relatively in this regime. Higher repetition rates regimes allowed for reasonable heat accumulation in the material which then generated more successful sintering and bonding onto dental enamel surfaces.

Table of Contents

List of Tables

List of figures

1 Introduction

The musculoskeletal system of the human body is a complex and substantial organ consisting of 206 bones, approximately 650 different muscles and cartilage, tendons and ligaments. Its primary functions of biomechanical movement, support and protection of internal organs can often be hindered by trauma and disease. Despite the capability of bones and hard tissues to regenerate themselves naturally, certain environmental conditions may arise in which natural processes cannot occur; such as large enough voids between tissues, poor remineralisation conditions, poor interfacing between the tissues, and degenerative disease.

As the elderly population grows and their longevity increases, hip replacement surgeries are becoming more and more abundant [1]. Osteoporosis and other osseous diseases also mean that these initial surgeries fail at a fairly high rate, with 9.8% of replacements causing complications within the first 90 days, and 22.75% of total hip replacements requiring revision surgery [2]. These revision surgeries occur due to several factors including infection, dislocation, and chronic pain which is often due to loosening of the implant, osteolysis (the loss of bone due to inflammatory responses to the implant itself) and subsequent periprosthetic fractures, where the relative stresses on the bone by the implant are too great [3].

The current methodologies utilised in hip implant technologies fail in these means due to two main factors; poor osseointegration of the implant into the joint, and the utilisation of standardised parts [4]. Each hip and patients' needs are invariably different, and more effective means of treatment would require a form of personalised medicine. Luckily, as rapid prototyping technologies advance so does the reduction in cost for personalised part production and treatments, making these methods more affordable to the general population [5]. However, the production of these complex parts still loose in a further utility if they are poor at osseointegration and cause osteolysis.

The modern western diet, currently involves the consumption of large amounts of sugary and acidic food and drink stuffs that readily erodes the dental surface. This type of erosion is irreversible and causes the enamel to become thin or even disappear, exposing the underlying dentin or tooth root causing hypersensitivity and further problems such as carie formation and periodontal disease [6]. Oral care standards can also exacerbate these instances as it utilises abrasive techniques for general maintenance, which if done excessively can lead to gingival recession and further exposure of the dentin or root surfaces of the tooth. Current methods of treatment for dentin hypersensitivity or enamel loss are relatively poor in the long term, consisting of methods of nerve desensitisation, plugging of the dentinal tubules, or adhesive sealers. Neither of which offer a qualitative solution, or really solve the problem of demineralisation of the enamel or dentin surfaces [7].

There is therefore a need, in aide of medical development, to investigate methods in which we may coat personalised anatomically shaped implants that

integrate efficiently into the skeletal system, for more successful implant surgeries, patient satisfaction and reduction in the overall cost. Additionally, the restoration of dental enamel to teeth presents a solution to the ever growing problem of excessive wear, erosion and periodontal disease.

There are several types of materials that have been utilised in each of these cases, such as synthetic polymers, metals and ceramics [8], [9]. However, in light of the frictions that may be observed in the biomechanical use of joints and mastication with teeth, fragments due to wear can escape the parts and cause problems as foreign particulates can enter the blood stream or remain in the extracellular fluid, causing inflammation [10].

Modern employed materials then tend to have certain biological properties such as being bioinert, bioactive or bioresorbable materials, to aid in the reduction of inflammation should wear particulates be emitted [10]. The latter two material types become more favourably prominent when considering what material to use for this purpose. The use of bioactive materials that allow for reabsorption through natural mechanisms, utilises osseointegration, and prevention of osteolysis, should consequently be key properties for the material choice.

Calcium phosphates are therefore an attractive material to modify for the solution to the outlined problems, as they are the major inorganic ceramic component of natural bones and teeth, and many varieties of the types of these biominerals have the properties aforementioned [11].

The use of lasers in the modification of materials has been a widely studied area since their invention in the 1960's. Continuous wave lasers have formed the basis for many modern processing and manufacturing techniques. It was only

until the invention of Q-switching and then mode-locking that ultra-fast pulsed lasers could be realised. This was an added advantage to the laser processing of materials field as it was seen that the peak power within each pulse could be much greater than that of continuous wave lasers. Specifically lasers in the sub-picosecond, or femtosecond regime, revealed new material responses as the pulse durations are able to generate non-linear processes in materials.

Near infrared lasers also posit an interesting application in the medical field as the photon energy is of a significantly low value to maintain limited damage levels in biological tissue compared to that of ultraviolet or visible laser sources. This 'biological window' is a bandwidth within the near infrared, from 650-1350nm in wavelength, where there is very limited absorption by biological media [12]. This presents a plausibility of these types of sources to be used in situ.

We therefore intend to use calcium phosphates with near infrared ultrafast lasers sources to attempt to generate a solution to the problems of prosthetic osseointegration and dental enamel restoration.

The aims of this study follow the previous work completed within the literature, to choose a suitable calcium phosphate mineral and modify it to interact adequately with near infrared laser sources. A variety of sources should be implemented and tested to produce coatings on prosthetic material substrates and dental enamel substrates. The objectives then are realised within the following thesis outline:

1.1 Thesis outline

Chapter 2 is an outline of the literature that leads up to this thesis and discussion on the various methods in relation to the aims and objectives. There is some theory outlined which pertains to the characteristics of lasers in this regime, and a discussion of the previous work.

Chapter 3 provides information on the materials, methods and subsequent characterisations measured of the chosen materials, and a rationale for their choice.

Chapter 4 details and investigation into the upper energy limit that may be prescribed with the laser sources employed, due to the high energy limits which are discussed in chapter 2.

Chapter 5, 6 and 7 outlines the use of near infrared laser sources with varying repetition rate, and processing conditions toward the aims and objectives of this thesis, and details the experiments conducted in order to sinter the produced materials.

Chapter 8 is an overview discussion and assessment of the completed work, summary of the conclusions and suggestions for future work.

2 Literature review

The following chapter is a review of the relevant literature given the presented aims and objectives. Section 2.1 looks at calcium phosphates and some common methods that utilise these materials toward these aims. Section 2.2 then describes some of the theory behind laser matter interactions, particularly toward the femtosecond regime, and femtosecond processing of materials. Section 2.3 is an overview of the previous work, and finally, section 2.4 is a summary of the literature.

2.1 Calcium phosphates

Calcium phosphates are a well-known group of ceramics as they form the major inorganic component of animal hard tissues and have uses in an assortment of areas such as; acid and base catalysts, germicides, nutrient supplements, medicines, dentifrices, and stabilizers for plastics [13].

Materials used in clinical applications can be placed into two categories: Bioinert and bioactive. Bioinert ceramics, when placed into living tissue, have no consequential effects. Alumina or zirconia is an example of a bioinert material [11]. Bioactive materials, however, may interact with living tissue by bonding or instigating growth. Bioinert materials tend to exhibit slow reaction kinetics, and

it is for this reason that they appear to be inert, as they do not appear to react with live tissue. Bioactive ceramics are different in this manner, as they tend to instigate reactions when in the presence of physiological fluids [11], and respond chemically toward the creation of new bone or tissue. Several types of calcium phosphates and certain types of glasses have been shown to display these properties [14].

2.1.1 Properties and structure of calcium phosphates

There are many types of calcium phosphates (CaP's) which form several varieties of compounds dependent on the ratio of calcium to phosphate present, and in some cases the addition of various ions/hydrate groups. Table 1 shows a list of calcium phosphates as per their Ca/P ratio and functional group.

Table 2.1: The various calcium phosphates and their respective Ca/P ratios and formulas [15]

Ca/P	Name	Formula	Acronym
2,0	Tetracalcium phosphate	$Ca_4O(PO_4)_2$	TetCP
1,67	Hydroxyapatite	$Ca_{10}O(PO_4)_6(OH)_2$	OHAp
	Amorphous calcium phosphate	$Ca_{10-x}H_{2x}(PO_4)_6(OH)_2$	ACP
1,50	Tricalcium phosphate (α,β,γ)	$Ca_3(PO_4)_2$	TCP
1,33	Octacalcium phosphate	$Ca_8H_2(PO_4)_6{\cdot}5H_2O$	OCP
1,0	Dicalcium phosphate dihydrate	$CaHPO_4{\cdot}2H_2O$	DCPD
1,0	Dicalcium phosphate	$CaHPO_4$	DCPA
1,0	Calcium pyrophosphate (α,β,γ)	$Ca_2P_2O_7$	CPP
1,0	Calcium pyrophosphate dihydrate	$Ca_2P_2O_7{\cdot}2H_2O$	CPPD
0,7	Heptacalcium phosphate	$Ca_7(P_5O_{16})_2$	HCP
0,67	Tetracalcium dihydrogen phosphate	$Ca_4H_2P_6O_{20}$	TDHP
0,5	Monocalcium phosphate monohydrate	$Ca(H_2PO_4)_2{\cdot}H_2O$	MCPM
0,5	Calcium metaphosphate (α,β,γ)	$Ca(PO_3)_2$	CMP

A variety of studies have been accomplished surrounding these materials and have found that CaP's with a ratio of less than 1 are not suitable for in vivo implantation, as materials such as monocalcium phosphate monohydrate and dicalcium phosphate dihydrate (brushite) are not biocompatible with osseous tissue [16]. Calcium phosphates with Ca/P ratios higher than 1 have been found to be more biocompatible, tricalcium phosphate (TCP) has shown a more

favourable response to bone [17], [18]. Hydroxyapatite is the most investigated calcium phosphate in the region of clinical applications due to its good biocompatibility with soft [19]–[21] and hard tissues [22], [23].

Hydroxyapatite is the most famous of the apatites as it is the most similar to the biological apatites found in bone and tooth enamel. It has the formula $Ca_{10}(PO_4)_6(OH)_2$, which is a Ca/P ratio of 1.67. The other apatites have a similar formula except the OH- ion is substituted by other halogens or carbonate groups. Stoichiometric OHAp is in a hexagonal lattice structure, with space group $P6_3/m$, this is categorised by a six fold c-axis normal to three a-axes at 120° to one another with a = 0.9418nm and c = 0.6884nm (JCPDS #09-0432). The unit cell of OHAp is shown in Figure 2.1, Four columnar Ca(I) atoms are in two levels at z = 0 and z = 0.5. The remaining Ca(II) atoms create a triangular arrangement, one group of three at z = 0.25 and the others at z = 0.75. The consecutive Ca(II) triangles are rotated 60° from one another and form 'channels' which are parallel to the crystal c-axis. In these channels the apatite functional group (in the case of OHAp, ^{-}OH) lie, at the corner of each unit cell.

It is natural then to evaluate the use of hydroxyapatite for the use of augment coating for hip replacement procedures. For acid erosion, it would fall into the current implications of its natural use in enamel as it stands. However, it is apparent that OHAp would still be an effective choice. Other studies have concluded that tooth enamel (predominantly OHAp) converts to dicalcium phosphate dihydrate in the equilibration of acidic solutions [24], [25]. In fact, dicalcium phosphate dihydrate and dicalcium phosphate are the most stable

forms of calcium phosphates in acidic conditions [26], and so make a good candidate for acid erosion purposes.

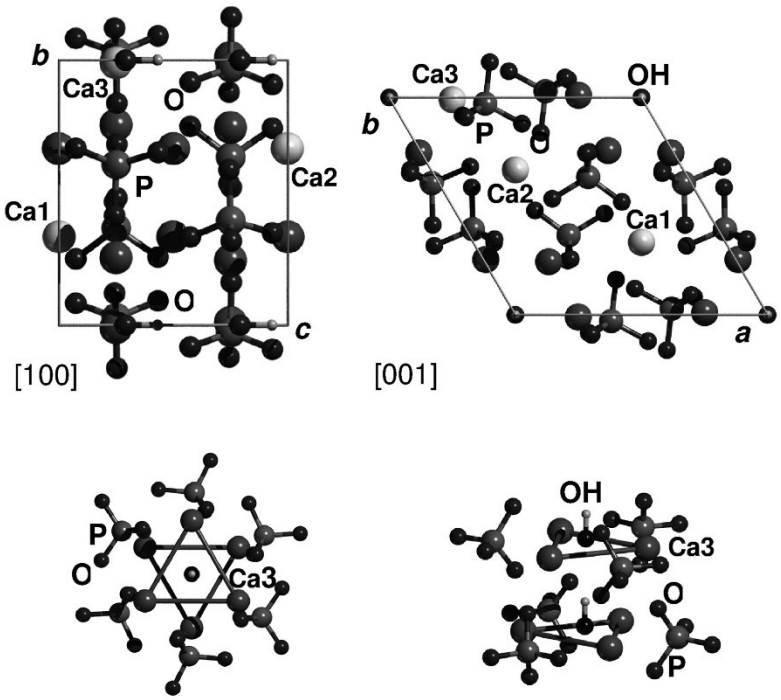

Figure 2.1: The Unit cell of hydroxyapatite [27]

Brushite (Dicalcium phosphate dihydrate; $CaHPO_4 \bullet 2H_2O$) forms a monoclinic crystal lattice structure, with a space group of I_2/a, with lattice parameters a = 0.588nm, b = 1.515nm and c = 0.637nm (JCPDS #72-0713). The unit cell of brushite is shown in Figure 2.2. It is a layered structure bound together by hydrogen bonding, with a zig-zag type links of Ca-O polyhedra which are parallel to the b axis, these are bound together with linking similarly zig-zag phosphate ion tetrahedra. This results in weakly bound 'sheets' through the hydrogen bonded associated water molecules [28].

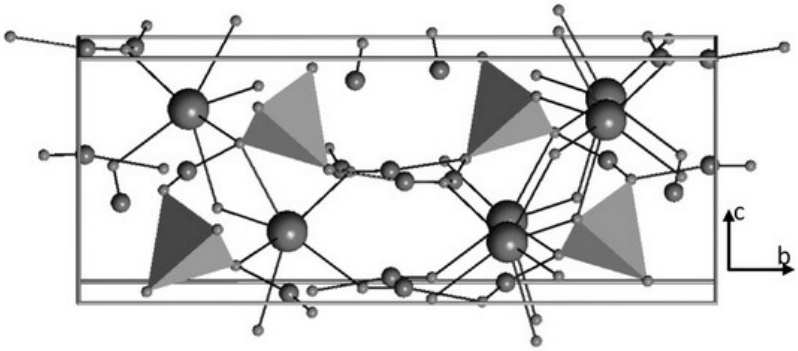

Figure 2.2: The unit cell of Brushite [28]

However, as stated earlier, calcium phosphates with a Ca/P ratio of 1 or less are not good for osseointegration [16], and the weak bonding of its 'sheets' due to the zig-zag formation of its phosphate ion tetrahedra, also make it a poor choice for a mechanically stable enamel coating material.

2.1.2 Calcium phosphates in dentistry

Considering that the natural structures of tooth enamel and dentine consists mainly of apatites, calcium phosphates become a natural choice in material for dental work. Most of the studies in this field have been made with either hydroxyapatite or β-TCP, using these materials mainly as bone substitute or bone-graft. They are used in the following ways: Immediate tooth replacement, augment construction for denture fitting, bone cement for periodontal repair, and metal implant coating [29].

Calcium phosphate coatings of implants for dental applications fall under many of the descriptions of §2.1.3. Their main other use is in calcium phosphate cements, these consist of calcium phosphate mixtures with other polymers or composites. The elasticity and strength of bone is due mainly impart to collagen fibrils, rather than the apatite calcium phosphate phase, therefore the development of cements has been to add strength to the calcium phosphate

composite mixture and cure in a readily available time [30]. The other benefit of cements is that it then creates an easily malleable paste for dentists to work with which may be able to fit into periodontal caries or lesions easily and set. Developments in this area tend to surround calcium silicate and sulphate based cements [31], PMMA medical cements [32] and collagen [33], [34].

Despite the large amount of studies undertaken toward calcium phosphate cements, there are still a large number of basic properties of the cements that need to be investigated in order to create successful products in dental applications [31]. The investigations of this study therefore present an opportunity of exploitation into this sector, where current methods are stalling.

2.1.3 Calcium Phosphate Coatings onto Metallic implant materials.

The relatively poor mechanical properties of bulk CaP ceramics means that much of the research in recent years has been focused on techniques that involve coating other materials, such as titanium alloys such as Ti-6Al-4V [35]. The following is an outline of these methods.

2.1.3.1 Spraying techniques

Plasma spraying involves the creation of plasma through passing a mixed gas through a direct current arc, this ionises the gas and accelerates it toward a target. It is then possible to suspend a metallic, ceramic or polymeric powder in the gas volume to be fired at the target. Due to the high temperature that is generated in these plasmas (up to 20,000K), the thermodynamic stability of calcium phosphate conveys an important role in the properties of the final product. Preferably, the outer most layer of each particle is the only region to suffer being heated to a molten plastic state, which inevitably undergoes a phase

transformation. To ensure dense and adhesive coatings, this plastic state is necessary, although by tuning parameters such as; type of gas, plasma speed, particle size and cooling of the coated surface, it is possible to obtain desirable coatings of crystallinity and calcium phosphate phase [36], [37].

Vacuum plasma spraying employs a similar technique but in low pressure environment. This has some advantages over atmospheric plasma spraying as particle/plasma gas velocity can be increased to almost three times the speed of sound [38] which results in a good coating and few pores. However, due to being in vacuum it is difficult to reduce the substrate temperature which can cause phase challenges as per the normal plasma spraying technique [39].

High velocity oxy fuel spraying adopts a fairly similar methodology to the plasma spray, except instead of ionising the gas mixture with a high voltage arc, oxygen and a fuel are pumped into an area and ignited to produce a high temperature and pressure and thus high velocity particles. The exhaust flow of 1700 m/s may be reached (~Mach 5, almost hypersonic), and flame temperature is limited to the combustion temperature of the oxy-fuel mix, which tends to be around 3000°C. This results in high hardness and improved bond strength with a lot of coatings, however, with hydroxyapatite; there is high level of porosity of the coating layer [40].

2.1.3.2 Wet techniques

Electrophoretic deposition of calcium phosphates onto titanium alloys can produce uniform coatings. Traditionally these coatings are then sintered in a high vacuum, the resultant coating contains multiple phases. Cracking and shrinkage of the coating can occur because of the sintering, also producing

thermal stresses due to the difference in thermal expansion of the substrate and the film [41], [42].

Sol-gel deposition has shown to produce dense coatings with strong adherence to the substrate by mixing reagents as a colloid of inorganic particles or metal alkoxides, the coatings are then fired at temperatures of up to 1000°C [43].

Electrochemical deposition involves an aqueous Ca and P ion containing electrolyte that is decomposed with a current onto the substrate. As a result the Ca and PO_4 crystals nucleate on the substrate surface. The surface is then treated at temperature for up to 6 hours [44]. The crystallites formed are slow developing, but is composed of small crystals, and can produce dense coatings [45].

2.1.3.3 Sputtering techniques

Sputter deposition is accomplished by bombarding a target with high energy ions under vacuum. This is a slow technique in the order of 1-1.5μm/hr [46], however, it is able to produce very dense and uniform coatings [47].

Pulsed laser deposition is similar to sputter deposition, instead of an ion beam bombarding a target, a laser beam ablates a target with the desired ions embedded in it. This technique also requires a vacuum, but can produce very accurate film thickness of hydroxyapatite on Titanium implant materials (0.02-0.05 nm/pulse) [48], albeit at a slow rate.

2.1.4 Densification of Calcium Phosphates

Immediate tooth replacement and augment construction are the main applications of dentistry for which calcium phosphates may be of use. These

parts are traditionally manufactured through the sintering, or densifying, of calcium phosphate powders or scaffolds[49]. In a similar fashion, scaffolds are also made for orthopaedic applications which require structurally stable forms of calcium phosphates[50]. It has been shown that the mechanical properties of the calcium phosphates are relative to the grain size [51] and porosity of the material [52], [53]. Therefore, for the highest efficacy in structural integrity and means of coating both enamel and titanium, crystal growth and low porosity are of the upmost importance. This is conventionally achieved by high temperature sintering, as can be seen in Figure 2.3, as the material reaches its melting point of ~1100°C there is clear amalgamation of smaller particles where prior, at 900°C, the material is a consistent particulate system.

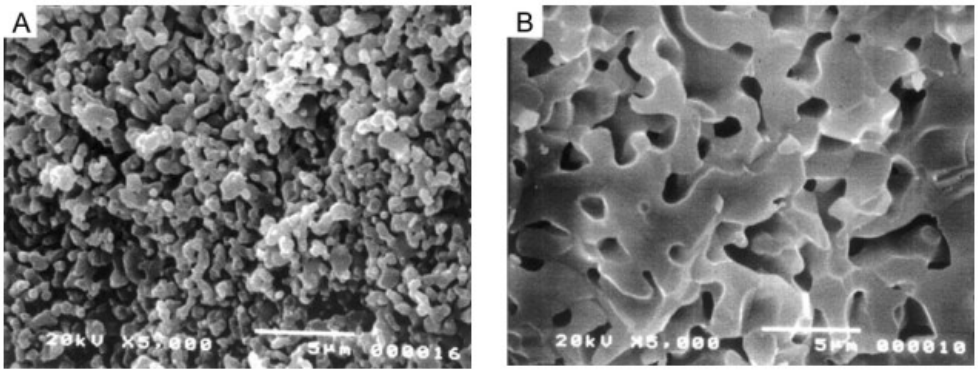

Figure 2.3: The effect of high temperature sintering on HAp at (A) 900°C and (B) 1100°C [54].

Sintering at 1300°C for 3h produces a uniform, relatively non-porous structure [52]. But sintering at this range, ~1350°C, causes a complete structural change of hydroxyapatite to tri-calcium phosphate, which can be detrimental to the structural properties [55], [56].

Microwave sintering of calcium phosphates is also another common method which tends to be more successful than conventional sintering; uniform bulk heating allows for less cracking and uniform shrinkage at a much faster rate, in

addition to maintaining the original material phase, despite high temperature [57], [58].

2.1.5 Laser Irradiation of Calcium Phosphates

Sintering and densification may also be accomplished with laser irradiation; in the literature this is mainly accomplished through absorption of continuous wave laser energy and induction of thermal effects. Hydroxyapatite may be sintered with a continuous wave laser in the near infrared at powers of ~3kW/cm^2 [59], [60]. Depending on the scan rate and power used, sound structures could be made, although similarly to thermal sintering, if the temperature of the material is allowed to reach ~1400°C, there is an imminent phase change to β-TCP, and subsequent weakening of the material. Other studies tended to avoid this problem by using a biphasic system with a sinterable biocompatible precursor materials such as PMMA derivatives [61], polyvinyl alcohol [62], poly(L-lactide-co-glycolide) [63] , Polyetheretherketone, Polycaprolactone and Poly(L-lactic acid) [64]. Creating stronger and more flexible scaffold type materials, much more synonymous with the structure of cortical bone.

On osseous tissues, UV excimer lasers have shown precise cutting but left thermal damaged areas of ~50μm [65]. Mid infrared CO_2 lasers are not so efficient at cutting and show severe charring of the osseous tissues due to excessive heat accumulation [66], [67]. Near infrared lasers, around 3μm, have shown interest in orthopaedics and dental work because of the high water absorption [66], [68], [69], however charring is still prominent [70], and intrinsic water absorption limits their use in surgery.

In the case of ultrafast sources, much of the literature then expands into femtosecond cutting of bone and dental materials [71]–[76], which due to its solid-vapour phase transition ablation mechanism, which is considered a non-thermal process due to the speed of the pulse and consequent interactions, preventing charring or thermal effects into the rest of the material.

Light etching of osseous surfaces with ultrafast sources has also shown increased wettability and adherence [77], [78] allowing for better osseointegration and augment bonding.

Non-destructive processing of tooth enamel with lasers has reported increased acid resistance [79]–[81] when subjected to laser irradiation toward carie prevention. Oho et al. suggested that this was due to the formation of micro-spaces formed within the enamel, by the dissociation of –OH and $–CO_3$ from interstitial parts of the crystal, as the lased enamel showed high positive birefringence [82].

Symeitz et al. have reported using femtosecond laser pulses to bond calcium phosphates to titanium alloy substrates [83]. Although this is technically not an interaction between the laser and the calcium phosphate, but rather stimulating the metal substrate surface to react with a surface layer of powder by taking advantage of the two differing ablation thresholds of the materials. Thermal accumulations of the metal surface then adheres the powder to the surface. Paital et al. has also reported similar results using continuous wave and ms pulsed Nd:YAG lasers [84], [85].

Inside the University of Leeds and this research group Elmadani et al. [86], studied 1.5μm, 2.5GHz, femtosecond irradiation of erbium doped brushite

minerals on the surface of dentin, and appeared to successfully occlude the dentin tubules. Anastasiou et al. has also reported utilising GHz, 1μm sources for processing ß-pyrophosphate and Fe_2O_3 nanoparticle/calcium phosphate biphasic mixtures to trigger sintering with these sources [87], [88].

Therefore, non-destructive processing of calcium phosphates by near infrared femtosecond laser sources for the means of sintering and densification appears to be a novel technique and solution to the problem, and can therefore represent an active area of research.

2.2 Laser-Matter interactions

It seems pertinent then to describe laser-matter interactions in order to devolve any limitations that might be encountered with the use of such ultrafast sources, and discover any effects that might be exploited.

The theory of light propagation through matter is well defined by Maxwell's equations; if the medium is linear and homogenous then the equations may reduce to:

$$\nabla \times \boldsymbol{E} = -\frac{\partial \boldsymbol{B}}{\partial t};\ \nabla . \boldsymbol{E} = 0$$

$$\nabla \times \boldsymbol{B} = \ \mu\varepsilon\frac{\partial \boldsymbol{E}}{\partial t};\ \nabla . \boldsymbol{B} = 0$$

Where **E** and **B** are the electric and magnetic field vectors, respectively; ε is the permittivity of and μ is the permeability of the material. In order for the macroscopic electrodynamics of these equations to be valid, it is therefore

assumed that depth of the penetration of the electric field into the medium is considerably larger than the interatomic distance of the material. Field penetration into the surface of an absorbing medium traditionally is always of the order of 100nm and so the conditions set for these equations are satisfied. These equations are then able to be coupled with the material equations as per Landau and Lifshitz [89]:

$$\nabla \times \nabla \mathbf{E} = -\frac{1}{c^2}\frac{\partial^2 \boldsymbol{D}}{\partial t^2}$$

$$\nabla . \mathbf{E} = -4\pi(\mathrm{e}n_e - eZn_i)$$

$$\boldsymbol{j} = \sigma . \boldsymbol{E}; \boldsymbol{D} = \varepsilon_0 . \boldsymbol{E}$$

Where c is the speed of light in a vacuum, **D** is the electric induction and with the electric field is a function of all three space coordinates as well as time, n_e and n_i are the number of electrons and ions respectively, e and Z, respectively, are the electron and nuclear charge, j is the current density and σ is the conductivity. The material equations for this expression, with respect to the electric field, are linear and in the local form. For dielectric materials it is much more convenient to describe the equations in the form where current and polarisation are separated [89]:

$$-c^2 . \nabla \times \nabla \times \boldsymbol{E} = 4\pi \frac{\partial j}{\partial t} + \frac{\partial^2 \boldsymbol{D}}{\partial t^2}$$

A current can now be derived from this equation due to the free carrier excitation and the electric induction can be related to part of the dielectric function that describes the polarisation, $\varepsilon_0(\omega)$. By applying the external field $\boldsymbol{E} = \boldsymbol{E_0} . e^{-i\omega t}$, this equation can then be reduced to the conventional form:

$$\nabla \times \nabla \times \boldsymbol{E} = \frac{\omega^2}{c^2}\varepsilon \boldsymbol{E} \equiv -\frac{\delta^2 \boldsymbol{D}'}{\delta t^2}; \boldsymbol{D}' = \varepsilon \boldsymbol{E}$$

Where the transient dielectric function is:

$$\varepsilon = \varepsilon_0(\omega) + i\frac{4\pi\sigma}{\omega}$$

For materials with a small number of conduction band electrons, at $\omega \gg 4\pi\sigma/\varepsilon_0(\omega)$ a solid should be approached as a material with dielectric function; $\varepsilon_0(\omega)$. In the case of conductors, electrons are free to move to the conduction band and therefore dominate the dielectric function, where the term $\varepsilon_0(\omega) = 1$ may be used in the above function.

These descriptions are then a representation of transmission, if light traverses through a medium and its electric field does not perturb a material response, such as absorption or scattering, then it is considered to have been transmitted.

2.2.1 Linear Absorption

Laser-matter interactions are primarily electronic; the modulating electric field vector of the beam interacts with atoms and their electrons. Continuous wave infrared laser radiation can induce lattice vibrations by oscillating atomic nuclei and directly generate phonons, which then can lead to local heat generation. But if the photon energy is adequate, a laser pulse may also interact with electrons by exciting them through their discrete energy barriers and promote the electron to a higher energy state.

The absorption of a photon is a complicated quantum process that may be described most effectively with quantum electrodynamics. However, the absorbed energy density rate may be specified without specifying the

mechanics of absorption. Landau and Lifshitz show the relation the absorbed energy density to the gradient of the Poynting vector [89]:

$$Q_{abs} = -\nabla \cdot S = -\nabla \cdot \left(\frac{c}{4\pi} \boldsymbol{E} \times \boldsymbol{H}\right)$$

This phrase may be time averaged to then give an expression for transient absorption, along with the material equations to derive an averaged expression for absorption and completed with a value for the incident laser intensity [90]:

$$Q_{abs} = \frac{2A\omega\kappa}{c} \cdot I(r, z, t)$$

Where A is the absorption coefficient, κ is the imaginary part of the refractive index and I is the intensity of the incident beam. It can be seen that absorbed energy density will be dependent on three factors; absorption coefficient (and thus the imaginary part of the refractive index), frequency and intensity. The latter of which can be greatly enhanced through the use of ultrafast laser sources, as even relatively small pulse energies can have immense peak intensities due to the miniscule durations for which the pulse duration lasts.

2.2.2 Non-linear absorption

The peak power of a laser pulse can be simply defined (Gaussian beams require a constant factor due to the shape of the pulse) as:

$$P_{peak} = \frac{E_{pulse}}{\Delta t}$$

As Δt decreases, it is evident that even moderate pulse energies can generate massive peak powers. Femtosecond pulse durations (~10^{-15} seconds) can generate peak powers that easily scale into the GW.

With the massive amounts of peak powers that are available with femtosecond pulsed lasers it is possible for the intensity of the beam to generate massive photon densities, this in turn can cause multiple photons to combine to generate higher harmonic single photon energies. Simultaneous absorption of two or more photons, to breach an energy potential greater than that of each photon and promote a material from one state to a higher energy electronic state, is called multiphoton absorption.

For irradiation of wide band gap materials, a single photon, unless in the low UV, will not have enough energy to promote an electron from the valence to the conduction band, and so multiphoton processes are required. The resulting photo-ionisation rate depends strongly on the intensity of the beam: σI^m is a second order non-linear process, where I is the intensity of the laser, σ is the absorption of m-photons, and the amount of photons required to breach the band gap of a material; $m\bar{h}\omega > E_g$, where E_g is the material band gap.

Once an electron has absorbed several photons to move to the conduction band of a wide band gap material, it is then in a position to further absorb incident photons at a linear rate until the electron has scaled m-photons above the conduction band, at which point, another electron is promoted to the conduction band and the absorbing electron returns to the conduction band edge. This is referred to as impact ionisation, as this occurs other electrons in the valence band are being created through non-linear absorption and further conduction band electrons are generated. What occurs concurrently is avalanche ionisation. Where this process repeats itself until the laser pulse is no longer present or intense enough.

Subsequently the conduction band of a material will become populated, drawing electrons from their bonds within the material. This can cause structural changes in the laser affected region, or if too intense, dielectric breakdown in the case of wide band gap materials.

2.2.2.1 Ultrafast electron and lattice dynamics

Electrons populated in the conduction band will then undergo several mechanisms until thermal equilibrium may be reached. Firstly, redistribution of the electrons in the conduction band will occur through electron-electron scattering, this is an elastic process as it is merely an electrostatic interaction between carriers. Distribution of this kind can cause de-phasing shortly after the pulse, but it takes hundreds of femtoseconds for the system to approach Fermi-Dirac distribution. Within the order of femtoseconds electron-phonon scattering will start to occur, this is an inelastic process as phonons are either generated or absorbed by the electrons; in this case, carriers will remain within the bounds of the band they fill. Because the energy transferred to phonons is quite small, many of these events must occur before the carriers and lattice may reach equilibrium.

Once equilibrium has been reached between the carriers and the lattice, the material is now at a definable temperature. However, the carrier distribution has remained the same, and so these carriers now must be removed before thermal equilibrium of the system may be reached.

Radiative recombination, or luminescence, may occur as electrons jump from the conduction band to the valence band and emit a photon. Electrons moving down to recombine in the valence band may also occur without radiation, but in

the reverse manner of impact ionisation, an electron in the conduction band will jump to a higher state. This is called Auger recombination; however, although free carrier density decreases during the combination the total energy remains constant. Carriers may also be redistributed out of the irradiation site and distributed in the surrounding material. Free carrier density remains constant for this process though and the previous two methods of recombination will then occur for the material to equalise.

Once an equilibrium temperature has been reached and excess free carriers have been removed, the material behaves effectively like it has been heated conventionally. With ultra-short pulses, however, this equilibrium temperature may be reached within a few picoseconds, despite the removal of excess carriers taking longer. Then, if the temperature of the lattice exceeds the melting or boiling point, melting or vaporisation will occur. The material will remain solid but superheated until nucleation of liquid or gas start on the material surface. This phase change will then spread throughout the material, as the energy that is deposited by the laser then is transformed to kinetic energy in the atoms, ions or molecules, these particles then have enough energy to leave the material surface, leading to ablation. If no phase transition is able to occur, then the system will just revert to its ambient condition through normal thermal processes, on the timescale of microseconds. However, if melting or vaporisation has occurred, then the material will re-solidify or condense onto the surface, in this case it is possible that the condensate will not be the same structure to the material that was irradiated, leading to surface modification of materials.

2.2.3 Ultrafast laser processing of materials

Femtosecond laser pulses feature their most prominent area of research in ablation and thus laser cutting of materials, as little damage may be sustained in to the nearby un-irradiated material area, making them relatively unique in terms of laser processing.

The machining of sub-micron features into metallic substrates with ultrafast lasers is a useful and successful area of research [91]–[94]. Where there are reports of highly precise defined drilling and cutting of metal films as deep as 1mm [95]. The amount of pulses required in achieving this kind of deep drilling and precise machining is still relatively high, as reported by Chichkov et al. Figure 2.4, on copper targets [94]:

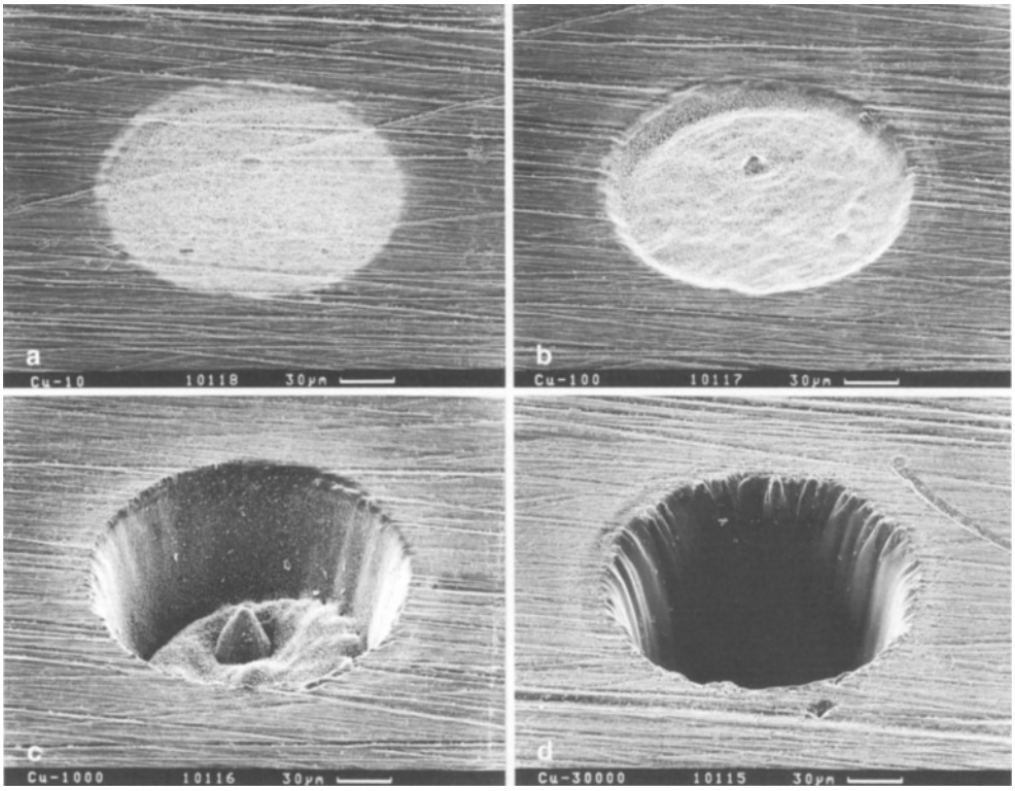

Figure 2.4: Femtosecond-pulse laser ablation of Cu a) 10, B) 100, C) 1000 and D) 30,000 pulses [94].

Kim et al. have reported significant machining with single 800nm 220fs pulses on a metallic chromium surface; Figure 2.5 [96]. And although single shot experiments are being carried out with increasing effects as higher pulse energies become available, multi-shot experiments show alternate melting effects, as can be seen as per Figure 2.4(c).

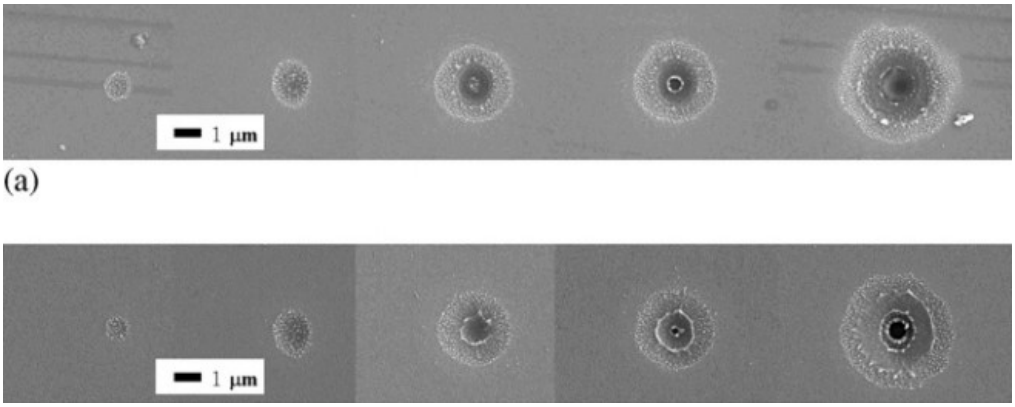

Figure 2.5: Results from Kim et al. single pulses of energy levels of 3, 11, 47, 64, and 250 nJ from left to right, where film thicknesses are (a) 200 nm and (b) 500 nm [96].

Similar studies have occurred in semiconductors, where the band gap of the materials sometimes exceeds the photon energy, and has generated similar results to that of metals [92], [97]–[99]. As is demonstrated again by Chichkov et al. and can be drawn in comparison to Figure 2.4, surface structural features are much more prominent, Figure 2.6 [94]:

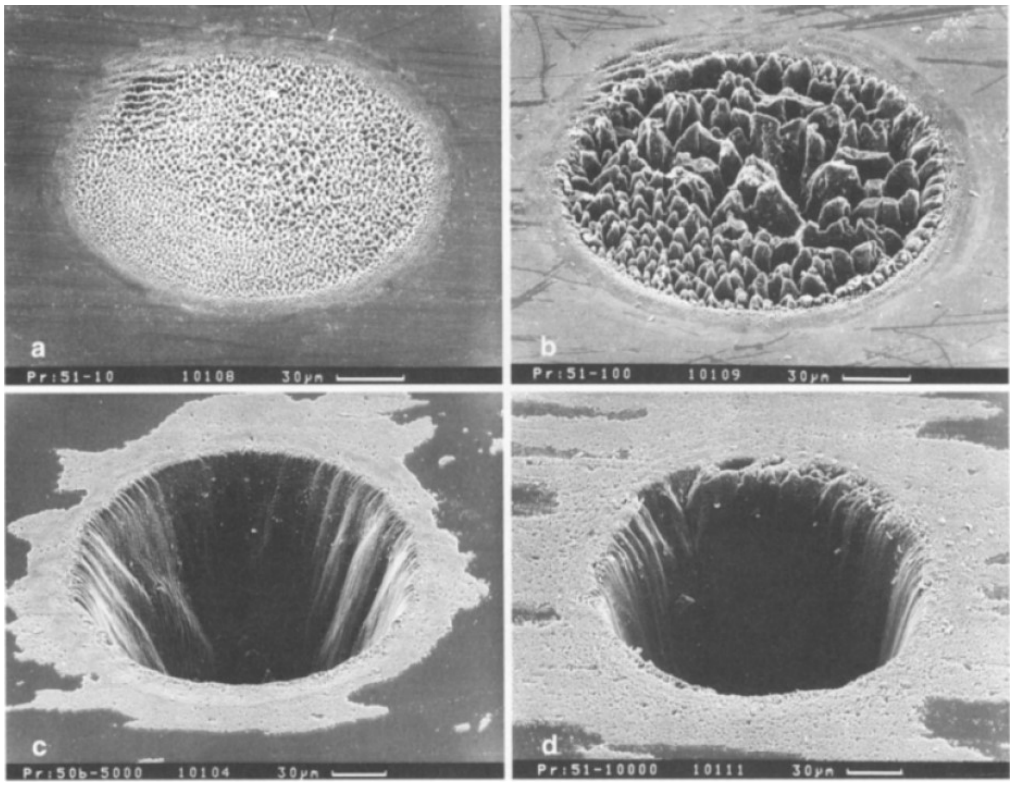

Figure 2.6: Laser ablation of a 0.3 mm thick silicon target with: (a) I0, (b) 100, (e) 5000, and (d) 10000 pulses. [94]

The same can be said for dielectrics and insulators [100]–[104]. This of course accounts for the machining of osseous tissue and tooth enamel as outlined in §2.1.5. Even transparent materials may be machined similarly [105]–[107], by utilising the lack of linear absorption of near infrared lasers in the main beam path in glasses, but utilising non-linear absorption solely at the laser focus. The general direction of transparent material machining appears to be in the formation of defects inside of bulk materials for waveguiding and optical modification [108]–[110] As can be seen in Figure 2.7, by Schaffer et al. [109]:

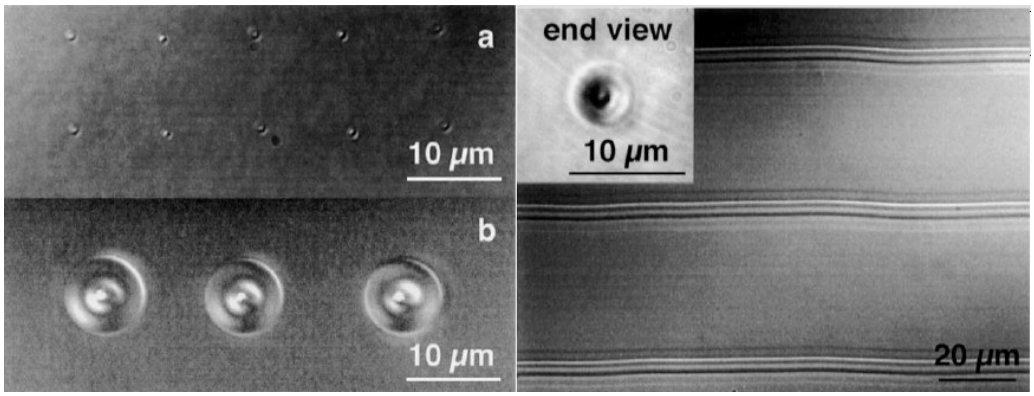

Figure 2.7: Optical images of structures made in glass with A) single and B) 25,000 femtosecond pulses. The right image shows tracks written with a 25MHz train at 20mm/s. [109]

Other processing mechanisms include patterning of structures or texturing of the material surface with ultrafast laser pulses, with ripples, conical structures and roughness, which has shown interest for adhesion and wetting of the surfaces in metals [111]–[115] and semiconductors [116]–[118]. Sundaram et al. describes this surface restructuring type process as lattice disordering, as electrons are driven far out of equilibrium, interatomic forces are modified as even a modest fraction of valence electrons are promoted to the conduction band [119], early stages of this are apparent in Figure 2.4 & Figure 2.6.

Laser welding of materials tends to be more efficient with nanosecond pulses, as heat generation and transmission are of importance in this application [120], although ultrafast pulses have been used to weld two different metals together [121] and metallic nanoparticles in suspension [122]. Ultrafast laser welding is observed in some glasses where a melt area is observed after a single pulse, Figure 2.8 [123]. This effect may be used to weld glasses together [124]–[126] with repetition rates of 1kHz to 10MHz and even bonding of glasses to metals [127] or glass to silicon [128].

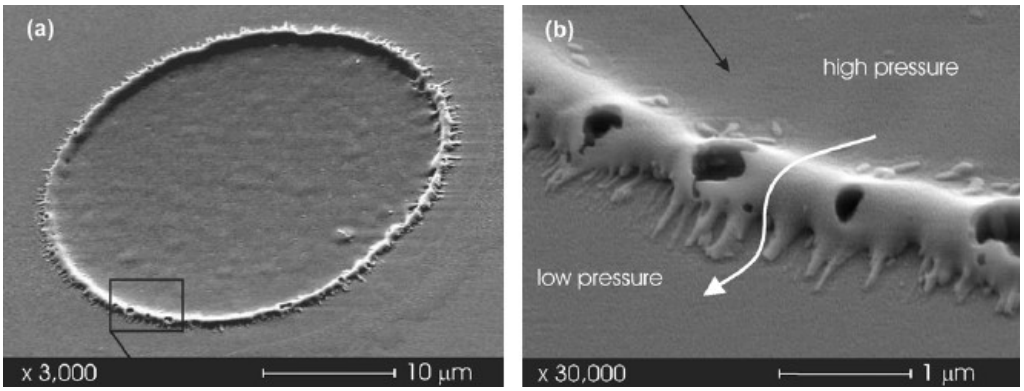

Figure 2.8: Image from Ben-Yakar et al. [123] Showing the surface melting of borosilicate glass with 100fs 780nm pulses

Synonymously with laser welding, femtosecond laser sintering has been observed in metals [129]–[132] and some semiconductors, most notably titanium dioxide, [133], but still remains a relatively understudied subject, thus permitting added motivation towards the aims of this work.

2.3 Previous work

Elmadani et al. [86] reported sintering of calcium phosphates doped with erbium and irradiated with a 2.5GHz, 1530nm, 120fs laser source. The paper shows some detailed characterisation of the materials but lacks in a description of the processes and mechanisms behind their observations.

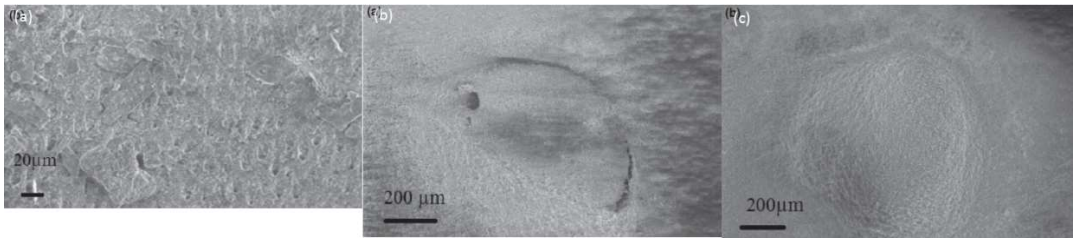

Figure 2.9: (a) a coated surface, (b) Area irradiated for 2 min and (c) area irradiated for 30s. [86]

Figure 2.9(a) shows a coated dentine surface with erbium doped brushite. Here the dentine tubules are visible, as are the platelet like particulates, however,

there are only a few particles visible and the coating is sparse over the dentine surface. If sintering was to occur on this surface it would not be adequately covered to determine that the coated mineral was the main constituent of the sintered surface. Figure 2.9(b) shows a sintered surface of erbium doped brushite for 2 minutes, with this magnification it is difficult to determine a difference between the pre and post irradiation surface. This surface appears to be coated more thoroughly, as the dentine surface is not visible. Figure 2.9(c) then shows an irradiated are for 30 seconds, which appears to be more uniform. But again, it is hard to determine the level of sintering here because of the magnification.

The paper then talks about the high peak powers achieved with the laser, which in reality are quite small. If the spot size was at 500μm then the peak power with the laser parameters given is 10^5 W/cm^2. This intensity is not high enough to induce any non-linear effects in the material (typically > 10^{14} W/cm^2) and linear attributions to the absorption would then be assumed. However, even with the similar average power values, average power density is only ~70 W/cm^2.

Elmadani then goes on to discuss the fact that Er^{3+} ions are the primary radiation absorber but then discusses the mechanisms behind material change, which is explained: The bonds within the material are excited and then relax between the pulses forming the sintered region. This mechanism does not require erbium as an absorber, and as electron attenuation is only expected through conduction band current density, bonds would not break/change

unless electrons may escape them, which would require exceeding the band-gap of the material.

Erbium ions have also been reported to have a high and broadband absorption and stimulated emission cross sections at ~1.5μm with a radiative quantum efficiency of over 80% [134]. Which suggests that erbium isn't the best absorbing medium if you intend to generate material change.

With the data from Elmadani et al. it is difficult to conclude on the potential methods of the proposed sintering. It seems apparent from the images that there has been a change from non-irradiated to irradiated samples. However, given the quantum efficiency of erbium at the source wavelength, it's likely that the differences seen in the samples are due to dehydration from water absorption near to the source wavelength [135].

Furthermore, as discussed in §2.1.1, brushite is not a structurally sound material due to the weak bonding of its 'sheets' because of the zig-zag formation of its phosphate ion tetrahedra. It also has a Ca/P ratio of 1, which does not serve the bioactive purposes or osseointegration.

2.4 Summary

Given that the main inorganic constituent of osseous and dental tissues are calcium phosphates, particularly hydroxyapatite, this material presents itself as a potentially useful medium for a bioactive coating. The utility of calcium phosphates in dentistry at present is limited to scaffolds and cements, mainly as a bioactive mineral component. This is likely due to the poor bulk mechanical

properties of calcium phosphates and therefore requires some kind of structural material, in order to be functional. Coating of a more structurally integral part, in this case the tooth itself, appears to be a unique method to solving the outlined problem.

It is clear that many of the current technologies in coating or working with calcium phosphates cannot be done in vivo or anywhere in situ to a patient. Most of the outlined processes require a vacuum or high temperature to get the desired coating. Surface and coating quality is also of importance, many of these techniques seem to fall short except for slow and extremely precise methods. The high cost and time per unit of these slow methods therefore also indicates some issues as to why these methods are not commercially utilised at present. It is clear that there is a need for more commercially viable methods of coating metallic parts, which could potentially be achieved through the methods outlined in the aims and objectives of this thesis.

Laser irradiation of calcium phosphates has been accomplished with the use of a variety of sources. Mostly with the use of mid infrared sources, most likely due to the poor absorption of calcium phosphates in the near infrared. Near infrared sources for these purposes then tend to be utilised with a green for scaffold forming. The utilisation of sources >1.5μm cause problems due to the increased water absorption in materials, creating charring of osseous tissues and therefore limits their use in surgery. A similar case can be made for UV excimer sources, where there was considerable thermally damaged areas post processing.

Ultrafast sources have been employed mainly for their efficiency in cutting without charring osseous tissues and have been used for enamel removal. Reports of increased acid resistance due to low intensity laser therapy, show there can be some moderate changes in the materials due to ion species migration in the material. As well as, utilising the difference in ablation thresholds between calcium phosphate minerals and metals, allowing for some adhesion of particulates onto metallic surfaces.

It is clear that there is a need to create a new type of rugged coating onto these titanium alloys that may be done affordably and quickly. Laser processing of titanium substrates shows a practical solution to this problem. Studies of continuous wave lasers employing calcium phosphates onto the substrate demonstrate some advantage but still lack in adhering the mineral layer to the substrate effectively.

The literature does not offer many examples of femtosecond laser pulses to process calcium phosphate materials by a mechanism of sintering or densification. The nearest examples of glass welding where melting and vaporisation can be seen to occur. The success of these studies, and the studies modifying bulk glass, is due in part to the aspect of the glass having no latent heat of melting and thus rapid phase change may occur of the order of the timescales involved in excitation and relaxation. The lack of studies, otherwise, in this area is most likely in part due to the difficulties that arise in photon absorption of materials with such large band gaps. In effect, this would only allow for non-linear absorption processes, and subsequent high energies and intensities.

The use of near infrared femtosecond laser sources to process wide band-gap materials, specifically calcium phosphates, outside the realm of ablation appears to be a relatively understudied area of research. Modifying these materials toward these purposes will therefore potentially generate an active solution to the problems outlined in the aims and objectives of this thesis.

3 Materials and characterisation

This chapter provides the rationale behind the choice of materials and methods used throughout this study, and it is intended to be a reference for the experiments that follow in the proceeding chapters.

The first sections, 3.1 & 3.2, considers hydroxyapatite, its synthesis and doping of hydroxyapatites. The third section, 3.3, analyses the precipitated materials in a variety of characterisation methods. And the final section, 3.4, outlines the methods utilised to generate the samples for later experimentation.

3.1 Hydroxyapatite

As described in §2.1., Out of all the calcium phosphates, Hydroxyapatite is by far the most ubiquitous. It has the formula $Ca_{10}(PO_4)_6(OH)_2$, and is an important ceramic that nature utilises readily. It is the major constituent of teeth and osseous tissues in the human body, making it an ideal candidate for a material choice in terms of solving the problems outlined for this study.

The properties of apatites can depend strongly on their preparation and processing conditions, and a variety of precipitation methods have been studied including sol-gel methods [136], [137], emulsion techniques [138], [139], hydrothermal routes [140], [141], solid state reaction [142] and precipitation

[143]. But the most widely used routes were wet chemical precipitation in an aqueous solution [144], [145], generally due to the large yields possible and at relatively equitable cost [146].

The effect of pH on aqueous precipitation of calcium phosphates is an extremely important factor in the formation of consistent and homogeneous materials [146]. pH neutral or mildly acidic formation of even stoichiometric hydroxyapatite Ca/P ratio synthesis leads to the formation of monetite, due to the lack of hydroxyl ions to compliment the hydroxyapatite stoichiometry and proton donation to the phosphate group [147]. Raynaud et al. found that in order to obtain reproducible stoichiometric hydroxyapatite precipitates, pH>8 and temperatures of 70+°C were the most favourable conditions [148].

3.1.1 Doping of hydroxyapatites

Doping of hydroxyapatites has proved relatively uncomplicated as substitution of the Ca^{2+} ligand cation of the apatite structure can be completed easily. The methods with the most efficacy for this modified synthesis are through co-precipitation techniques, as the substitution cations can easily form into the apatite structure during synthesis, avoiding deficient or excessive cation sites or surface structures as a result of ion adsorption [149].

Yasukawa et al. has reported the doping of both light [150] and heavy [151] rare-earth ions into calcium phosphate structures. Their results showed with increasing dopant levels, the rod like morphology of the hydroxyapatite was reduced to form rhombohedra type shapes. They used wet chemical synthesis to produce the precipitate and substituted the relevant ions into the mixture

during the reaction with dissolvable rare earth ion nitrate salts. This is also the case for the previous work by Elmadani et al. [86] in brushite.

Transition metal ions have also been substituted into the structure of hydroxyapatites for their antibacterial effects including copper, zinc [152], and silver [153]. As well as other metal ion complexes to increase osteoblast adhesion and bioactivity, such as Platinum, Ruthenium, [154], manganese [155] and strontium [156], [157].

3.1.1.1 Iron doping of calcium phosphates

Iron doping (Fe^{2+} and Fe^{3+}) of hydroxyapatites has also been reported relatively thoroughly throughout the literature [158]–[160]. However, most applications of doping with iron ions into the HAp structure have been toward sensing applications [161], [162] and iron adsorption for biological purposes, and so rarely involves utilising the iron for absorption of laser light. Rau et al. reported Fe-doping of a hydroxyapatites for a similar application, they report utilised pulsed laser deposition of the Fe-doped HAp onto titanium substrates [163]. However, the optical properties of Fe^{3+} doped HAp still remains fairly understudied.

Iron is interesting in the case of this study due to its visible and near-infrared (vis-NIR) properties. The optical absorption spectra of Fe^{3+} displays broad peaks in the vis-NIR due to intense charge-transfer bands with visible region low-energy limbs. High energy bands tend to obscure the weak spin forbidden d-d band transitions that would normally define the electronic transitions in the Fe^{3+} atom providing some luminescent properties towards the UV [164]. However, low energy photon excited electrons in 3d transitions are dipole

forbidden by Lapporte's rule and are assumed to dissipate non-radiatively. Podlowksi et al. have shown that the $^5T_{2g} \rightarrow {}^5E_g$ transition has high non-radiative quantum efficiency as multiphonon emission processes are the dominant relaxation route in Fe^{2+} [165]. The analogue of which for Fe^{3+} would be the ν_1 allowed transition $^4T_{1g} \rightarrow {}^6A_{1g}$, centred at 10525$cm^{-1}$ or 950nm [166]. We can therefore expect any absorption in this region to follow multiphonon emission relaxation processes, similarly.

This behaviour of the Fe^{3+} atom in substitution to a non-absorbing medium could mean that the base material could be modified to interact with a large bandwidth of vis-NIR wavelengths, with few losses due to photoemission, and create highly localised heating.

3.2 Material preparation

3.2.1 Hydroxyapatite

Hydroxyapatite (HAp) was synthesised using the wet chemistry method outlined by [145]:

$$10Ca(NO_3)_2 + 6(NH_4)_2HPO_4 + 8NH_4OH \rightarrow Ca_{10}(PO_4)_6(OH)_2 + 20NH_4NO_3 + 6H_2O$$

This was favoured over other methods such as the dissolution of Ca(OH) method [144], as it was possible to buffer the reaction with ammonium hydroxide to keep high pH and the resultant unwanted components are in a highly soluble nitrate form.

The synthesis was accomplished by heating 100ml calcium nitrate 0.1M solution (SIGMA-ALDRICH; C1396) and stirring with a magnetic stirrer, to maintain a

consistent temperature of 70°C, and mixture throughout the reaction. Dropwise addition of 100ml of 0.06M ammonium phosphate solution (SIGMA-ALDRICH; 379980) into the calcium nitrate solution to establish a molar ratio of calcium to phosphate; Ca/P of 1.667. The pH was kept at 9 with a dropwise addition of an ammonium hydroxide buffer throughout the reaction and the temperature was maintained. After all the solutions had been mixed and a precipitate was seen to be formed in the beaker, it was covered and left to stir at temperature and pH, to equalise for 2 hours. The resultant precipitate was then filtered through grade 44 filter paper (Whatman; 1μm pore size) and washed by rinsing the precipitate with distilled water several times to eliminate soluble reactant by-products. The drained filter paper was then air dried at 80°C for 12 hours to dry the product and then ground by a mortar and pestle until a fine powder was produced. The resultant ground powder was then collected and stored in a dry, cool place out of sunlight.

3.2.2 Fe^{3+} doped hydroxyapatite

For iron doped hydroxyapatite (FeHAp), calcium molar concentration was reduced and iron nitrate (216828 SIGMA-ALDRICH) was added to maintain a (Ca + Fe)/P ratio of 1.667, for Fe molar doping profiles of 5at.%, 10at.%, 20at.% and 30at.%.

pH stability of Fe^{3+} in solution is of practical importance as it is possible for Fe^{2+} ions to form if the solution will allow for reduction. Luckily the stability of Fe^{3+} ions is more prominent in highly alkali solutions, as can be seen in Figure 3.1 [167], where above pH 8, $Fe(OH)_3$ species are the most stable species of Fe ion.

During the addition of Iron nitrate into the calcium nitrate solution, it was noted that the solution turned a clear reddish amber, and the pH dropped to extremely acidic state. The fluid turned a darker rusty colour with the addition of ammonium hydroxide buffer, presumably as the solution moved through the pH, redox reactions of the Fe-$(OH)_x$ species stabilised toward Fe^{3+} creating the darker consistency.

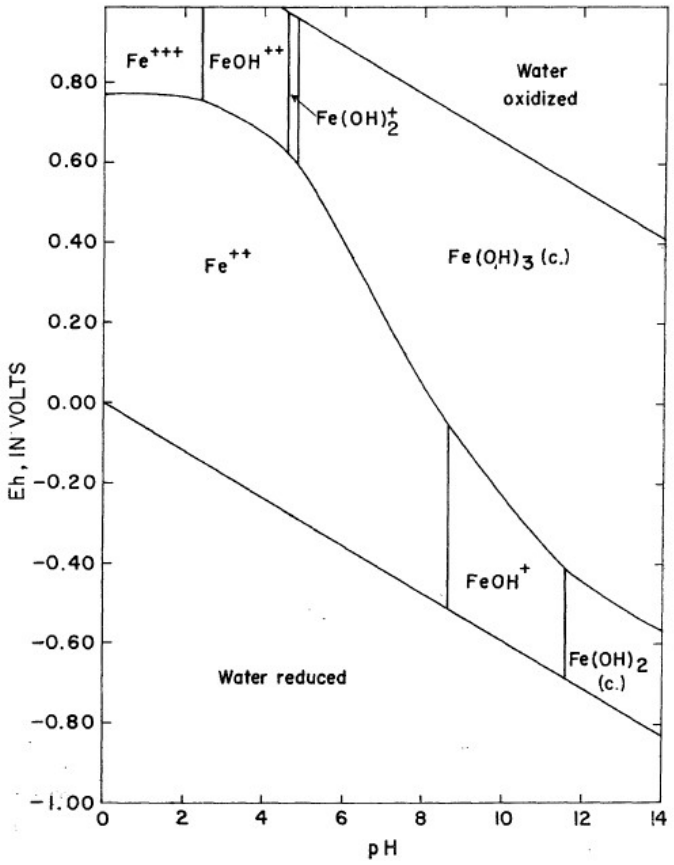

Figure 3.1: Stability field diagram for aqueous ferric solutions [167].

Figure 3.2 shows the precipitates after the described precipitation processes, it is quite clear that the effect of iron doping on the materials turns them a reddish-rusty colour with increasing Fe^{3+} doping.

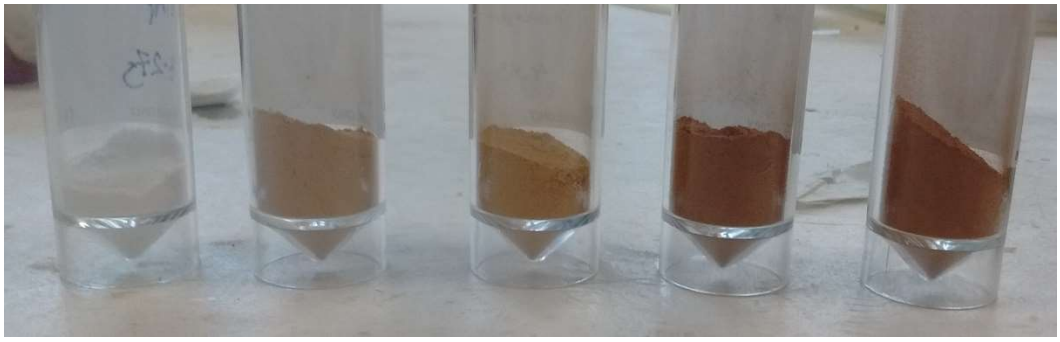

Figure 3.2: Image of the precipitates from left to right; 0%, 5%, 10%, 20% and 30% FeHAp

3.3 Material characterisation

3.3.1 X-Ray Diffraction

X-ray diffraction (XRD) was used for crystal structure and phase analysis with the instrument (Brucker D8, CuKα; 0.1540598nm wavelength) at 40 kV and 40mA, between 10-70° of 2θ and at 2°/min. XRD patterns for all samples are shown in Figure 3.3, and exhibit only hydroxyapatite phase peaks (Table 3.1) despite increasing iron content. Many minor peaks of the hydroxyapatite structure also diminish to negligible intensities, leaving only the major peaks at 2θ = 25.983 and 31.821.

Table 3.1: Hydroxyapatite peak list (JCDPS# 16-1185)

Hydroxyapatite ($Ca_{10}(PO_4)_6(OH)_2$)						
No.	h	k	l	d [A]	2Theta[deg]	I [%]
1	1	0	0	8.151	10.846	11.2
5	1	1	1	3.8794	22.906	13.5
7	0	0	2	3.4265	25.983	38.9
9	2	1	0	3.0808	28.959	20.8
10	2	1	1	2.8099	31.821	100
11	1	1	2	2.77	32.292	50.9
12	3	0	0	2.717	32.94	71.3
13	2	0	2	2.6227	34.16	22.9
17	1	3	0	2.2607	39.843	16.7
25	2	2	2	1.9397	46.797	21.5
26	1	3	2	1.887	48.185	11.7
28	2	1	3	1.835	49.642	33.6
29	3	2	1	1.804	50.554	11
30	1	4	0	1.7787	51.325	9.8
31	4	0	2	1.7514	52.185	9.9
33	0	0	4	1.7132	53.439	11.5

Peak broadening and decreasing peak intensity occurs as the iron content is increased, but no extra phases are present, which suggests that iron has been successfully incorporated into the hydroxyapatite structure, albeit with limited crystallinity. The lack of any large scale broad peaks discredits a purely amorphous component to the powder. We might expect the concentration gradient of the trivalent Fe^{3+} cations replacement of bivalent Ca^{2+} cations in the structure to distort the crystal due to increased valence, thereby affecting crystallinity.

The average crystallite size, D (nm) of the powders was determined through application of the Scherrer equation [168]:

$$D = \frac{k.\lambda}{B_{1/2}.\cos\theta} \qquad 3.1$$

Where λ is the wavelength of the Cu Kα radiation (λ = 0.15418nm), k is the shape factor, in this case 0.9, $B_{1/2}$ is the FWHM for the peak in consideration (rads) and θ is the angle of the corresponding diffraction. The peak value at 2θ = 25.9° was used to evaluate the crystallite size of the powders.

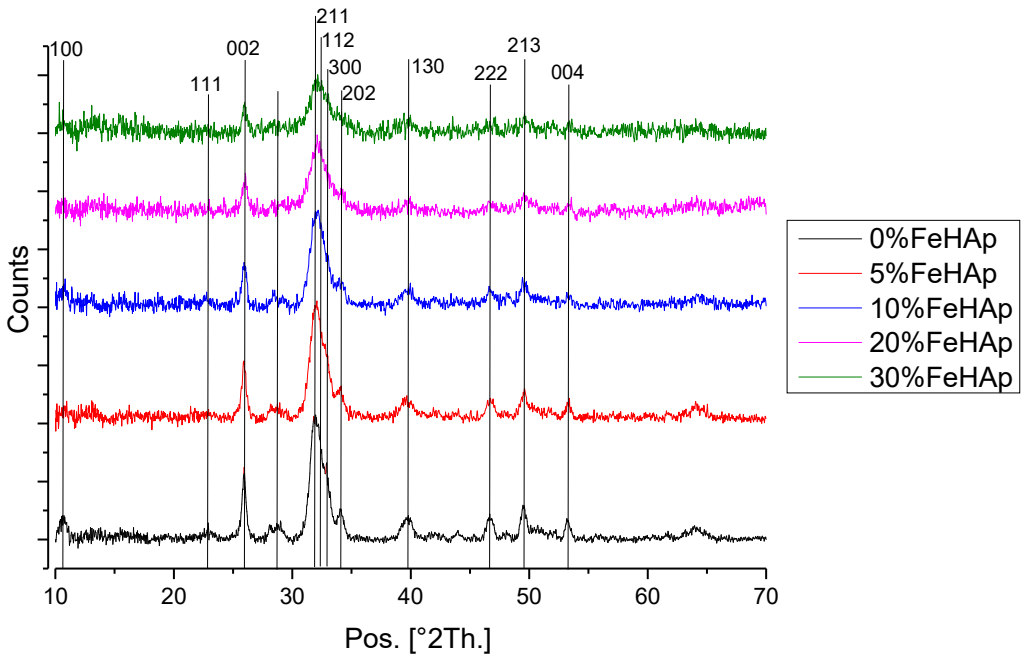

Figure 3.3: XRD spectra of the synthesised hydroxyapatite minerals throughout the doping profiles.

The crystallinity can be calculated by [169]:

$$X_c = \frac{\sum A_C}{\sum A_C + \sum A_A} \qquad 3.2$$

Where $\sum A_C$ is the total area under the crystal peaks, and $\sum A_A$ is the area under the non-crystal, or amorphous regions. Lattice coherence and strain broadening within the XRD spectra can be analysed through the Williamson-Hall method, where the intercept and slope gradient represent the coherence length broadening and strain broadening, respectively [169]:

$$B\cos\theta = 4\varepsilon\sin\theta + \frac{0.9\lambda}{D} \qquad 3.3$$

The Scherrer average crystallite size, D, of the of the particles, Table 3.2, reveals relatively uniform values for each powder and can therefore only be attributed to mild broadening across all samples due to crystallite size, and cannot account for the observed trend of decreasing peak intensities in Figure 3.3. Broadening via strain and coherence length values, also shows little legitimacy in the observed trend, as strain and length coherence scale with doping concentration until a point. This scaling is reversed by a sudden decrease in strain and coherence length for 20 and 30at.%.

Increasing Fe^{3+} content results in a decreasing crystallinity which can explain the decreasing intensities observed in Figure 3.3. This coupled with strain and coherence broadening in the 20at.% Fe^{3+} region can account for the depreciation of intensity with doping concentration. The introduction of Fe^{3+} appears to distort the lattice, creating the observed peak strain broadening, this is likely due to the charge difference between Ca^{2+} and Fe^{3+} ions as well as atomic radii, approximately 100pm and 60pm respectively [170].

Lattice parameters were calculated from relations of the hexagonal structure from peak position and hkl miller indices of the respective plane [171]:

$$\frac{1}{d^2} = \frac{4}{3}\left(\frac{h^2 + hk + k^2}{a^2}\right) + \frac{l^2}{c^2} \qquad 3.4$$

Table 3.2: Scherrer crystallite size, crystallinity, peak broadening due to lattice strain and coherence length and lattice parameters.

			Broadening		Lattice Parameters (nm)	
	D(nm)	Crystallinity (%)	Strain	Length	a	c
0%Fe;HAp	22.11	54.34	-0.00062	20.3871	0.9457	0.6834
5%Fe;HAp	19.38	29.65	0.001697	24.7131	0.9431	0.6872
10%Fe;HAp	19.99	26.00	0.002437	29.3335	0.9446	0.6818
20%Fe;HAp	18.09	26.47	0.00017	18.5374	0.9446	0.6852
30%Fe;HAp	21.54	22.03	0.000137	22.0527	0.9429	0.6795

The lattice parameter values appear to vary with crystallinity and doping concentration, where the parameter values have been calculated on the (121) and (222) planes. However, we might expect the crystal strain in a particular dimensions to not be constant as the position of the Fe^{3+} ions in the structure is undeterminable, and therefore would strain the lattice depending on its position in the apatite structure. The calculations will be based on an average of the selected planes, and so the net result of this expectation would alter the crystallinity, which appears to the only variable that can be correlated with the observed trends in the XRD spectra.

3.3.2 Scanning electron microscopy

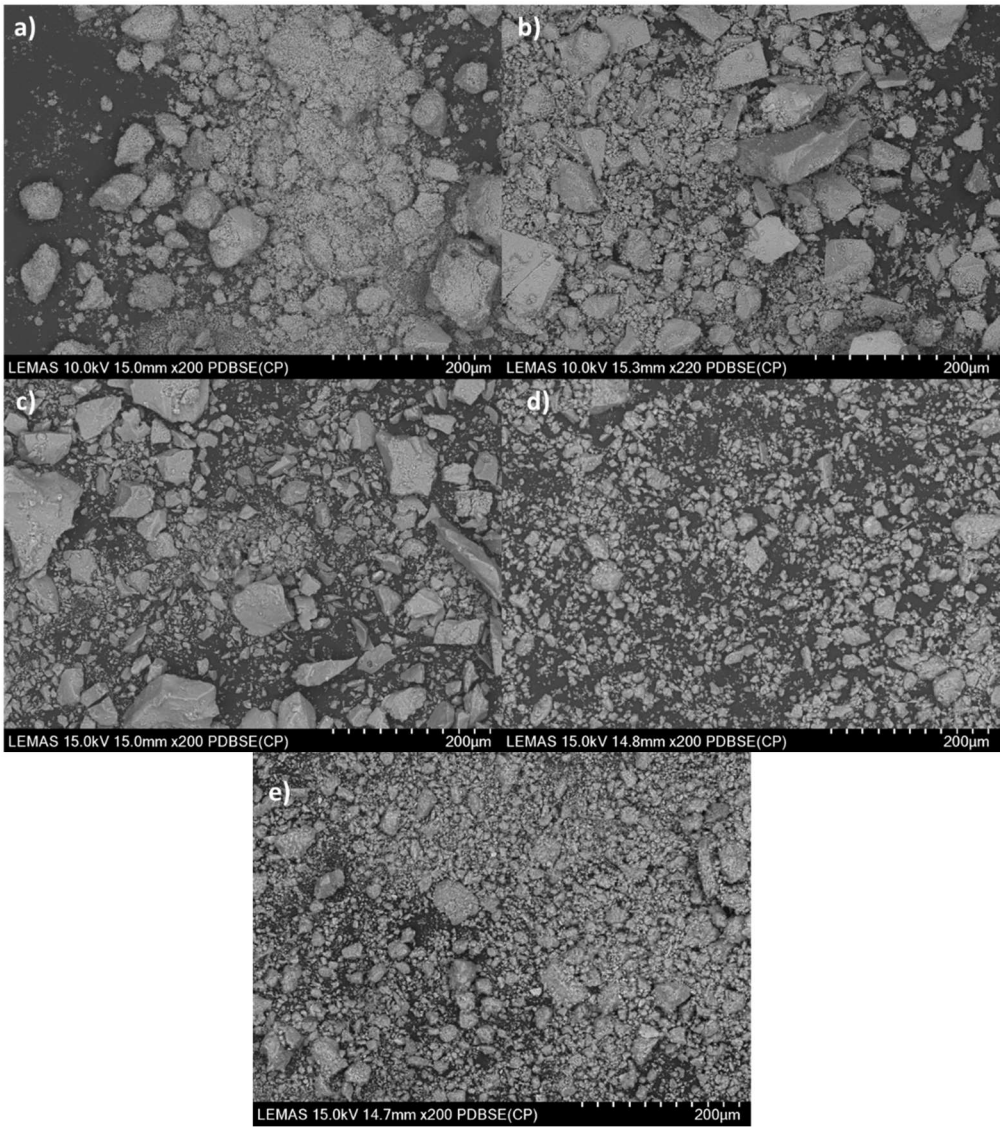

Figure 3.4: Scanning electron microscopy images of a) 0% FeHAp b) 5% FeHAp c) 10% FeHAp d) 20% FeHAp and e) 30% FeHAp powders.

Scanning electron microscope (SEM) images were obtained using a Hitachi SU8230 high performance cold field emission (CFE) SEM with Oxford Instruments Aztec Energy EDX system. Figure 3.4, demonstrates that post precipitation and milling agglomeration is present in the powders, with a mixture of sizes of agglomerated particulates, ranging from microns to a few hundreds of microns. However, high magnification images of these agglomerates, Figure 3.5, show that these objects consist of much smaller sub-

micron crystallites. These crystallites appear become less rod like with increasing iron content up to 10at.%, where they form a more aggregating rhombohedra. This is similar to the reported morphologies from Yasukawa et al. [150], however, these studies were limited up to 10at.% doping concentrations. As can be seen in Figure 3.5(d & e), at 20at.% the rod like formations are again more prominent and homogeneous, with 30at.% showing crystal like flakes.

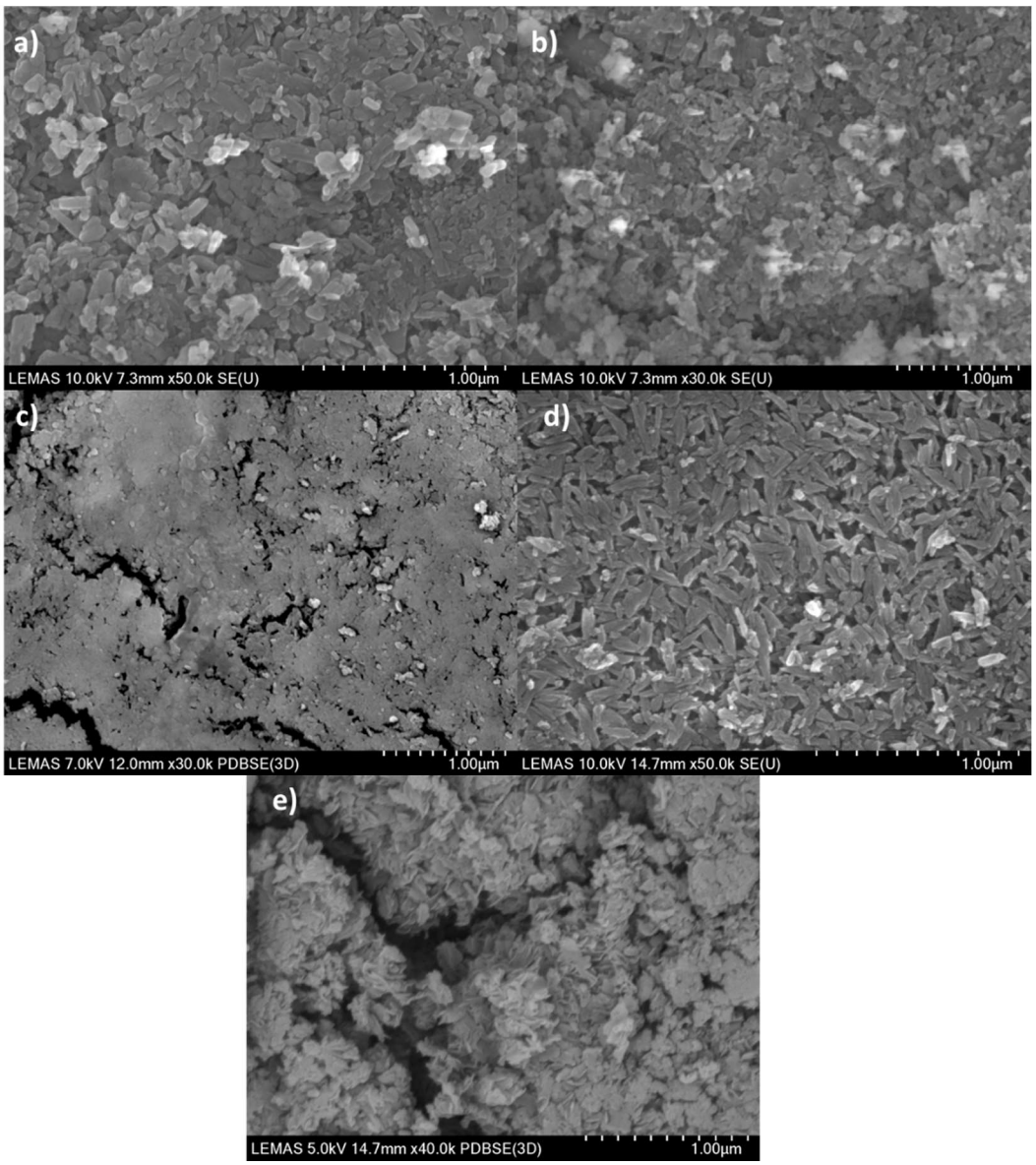

Figure 3.5: High magnification SEM images of a) 0% FeHAp b) 5% FeHAp c) 10% FeHAp d) 20% FeHAp and e) 30% FeHAp powders.

This is somewhat in contrast to what we might expect given the XRD results in Figure 3.3 and Table 3.2. Which appears to demonstrate increasing disorder and lack of crystallinity with increasing Fe^{3+} content. The strain and coherence length in these samples appear to be playing a major role in the distortion of the XRD spectra, perhaps due to a higher probability of the Fe^{3+} being contained in the planes used for the calculation.

3.3.2.1 Electron Dispersive X-Ray spectroscopy

Electron dispersive X-Ray (EDX) spectroscopy was completed using the AztecEnergy software, a map of a 10% FeHAp crystal can be seen in Figure 3.6, showing no biphasic type material, and homogeneous distribution of Fe around the crystals imaged. Confirming that Fe^{3+} has been substituted into the HAp structure. The map sum spectrum, Figure 3.7, showed the observed peaks in this map. Table 3.3 shows the normalised quantitative amounts of each element with respect to doping concentration and seem relatively close to unity.

The accuracy of the calculated weight % amounts for each element is questionable when considering EDX, as the backscattered X-Ray intensity into the detector depends on a variety of variables, and so the quantitative correction procedure within the software may have been chosen favourably. We might not expect the final precipitates to have exact amounts of each component as intended, however, these results confirm with some margin error, the relative composition of each powder has a correlation to the precipitated amounts and Fe^{3+} content in the crystals has not saturated.

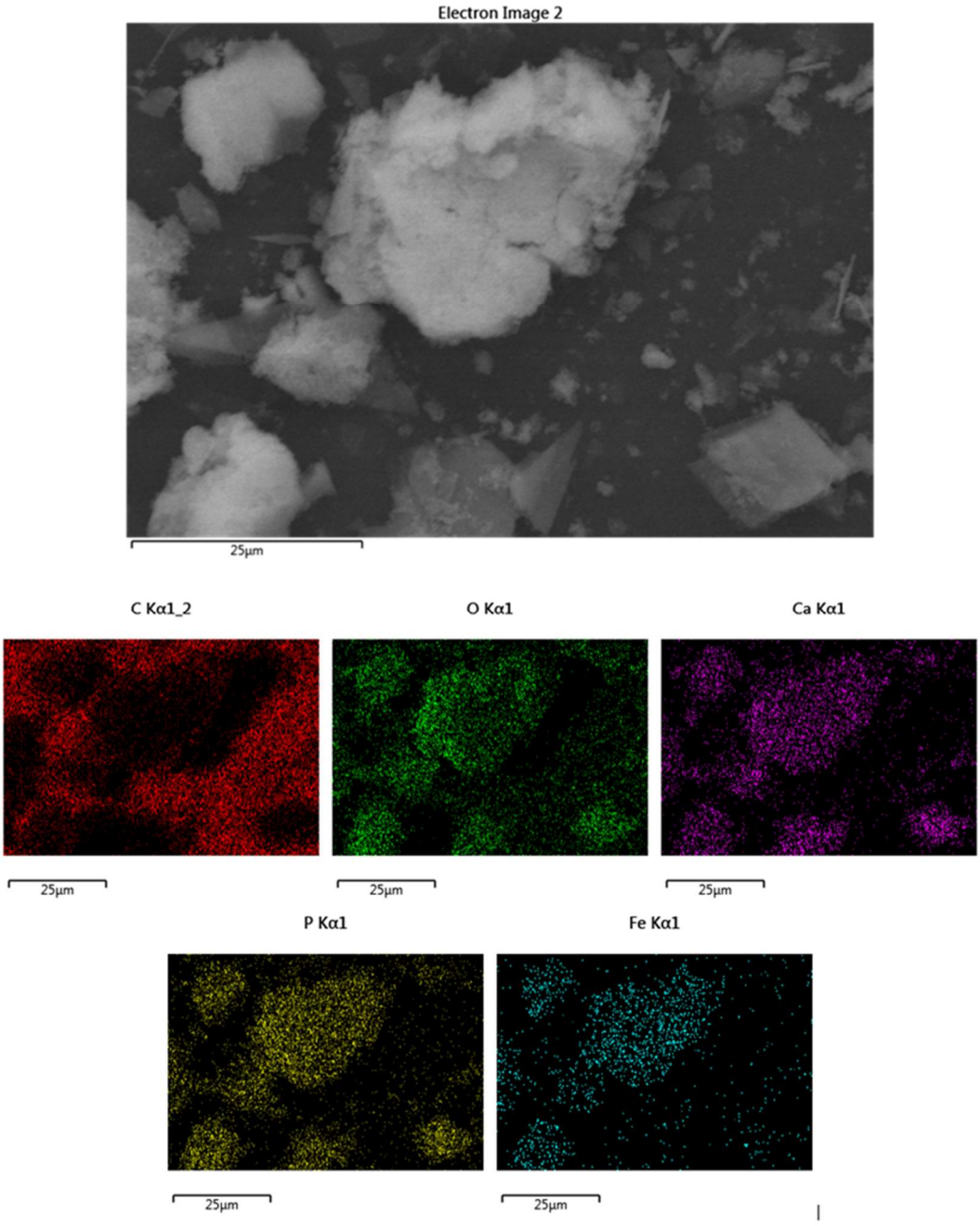

Figure 3.6: EDX of 10% FeHAp, clear Fe Kα1 signal in the region of the crystals.

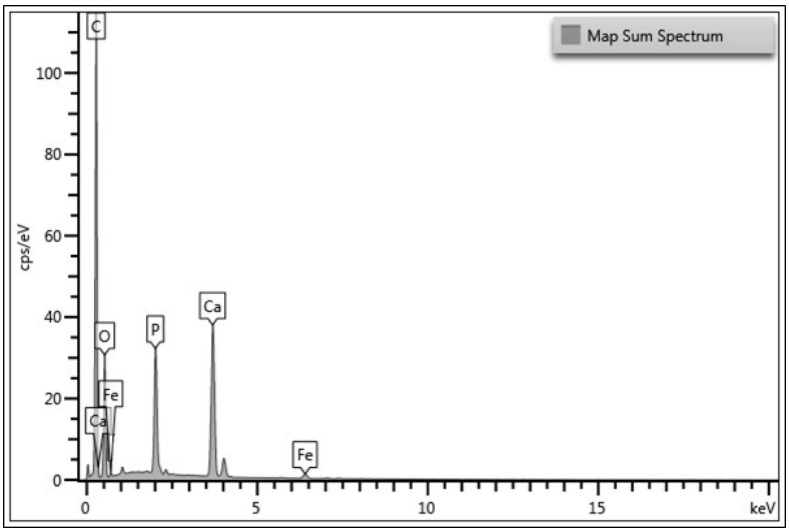

Figure 3.7: EDX Map sum spectrum for Figure 3.6

Table 3.3: Normalised quantitative EDS elemental analysis for FeHAp powders

	Weight %				
Fe dopant concentration	0%	5%	10%	20%	30%
O	41.48	41.04	41.24	41.81	40.99
P	18.36	18.74	19.13	18.94	18.23
Ca	40.16	37.43	33.73	29.02	24.83
Fe	0	2.79	5.90	10.23	15.95
	Relative %				
Fe	0.00%	5.40%	11.27%	19.16%	28.74%

3.3.3 Particle size analysis

Particle size analysis of the powders was acquired with the Malvern Mastersizer 2000E, the powders were mixed into the water stream and passed between a light source and detector. A calculation is then completed, assuming the powders to be exact spheres. Therefore, the results obtained are calculated from an average of the 2D image a particle might form during its transit through the fluid, in front of the detector, and so is not an exact method of particle measurement, should the powder not be exact spheres.

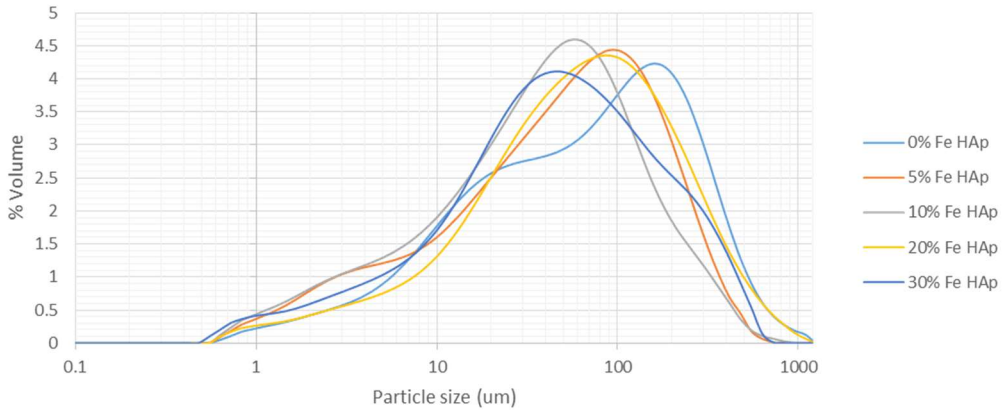

Figure 3.8: Particle size distribution of FeHAp powders

Figure 3.8 shows the distribution of the particles by size and confirms the size estimation of the agglomerates made from the SEM images in Figure 3.4.

Table 3.4: Particle size distribution of FeHAp powders

	Particulate size distribution (µm)				
	0% FeHAp	5% FeHAp	10% FeHAp	20% FeHAp	30% FeHAp
d (0.1)	7.42	4.36	4.07	8.21	5.26
d (0.5)	66.49	49.07	37.85	59.58	42.58
d (0.9)	282.93	190.97	157.52	252.93	218.97

The relative size distribution of the agglomerates and the percentiles are in Table 3.4. The average (d(0.5)), appears to be around 50µm, with quite a large spread of particle sizes up to ~200µm. The highest volume of particles being around 100µm.

The large spread of agglomerate size might be concerning should we need homogeneous particles for this application. Conversely, this range of sizes will likely be beneficial, as packing density may be increased as smaller particles may fill the interstitial voids between larger packed agglomerates. A high packing density will benefit densification and coarsening during sintering as thermal transport and interfacial surface area will be increased.

3.3.4 Fourier Transform Infrared (FTIR) spectroscopy

Functional group analysis was conducted by Fourier Transform Infrared spectroscopy (FTIR, Brucker Vertex 70 spectrometer) in the mid-infrared range (400-4000cm-1) using an attenuated total reflectance accessory. The FTIR spectrum shown in Figure 3.9 , confirms the presence of phosphate groups with the peaks at 561, 574 and 602 cm^{-1}, representing the triply degenerated bending modes of ν_{4c}, ν_{4b} and ν_{4a} of the O-P-O bonds of the phosphate group respectively.

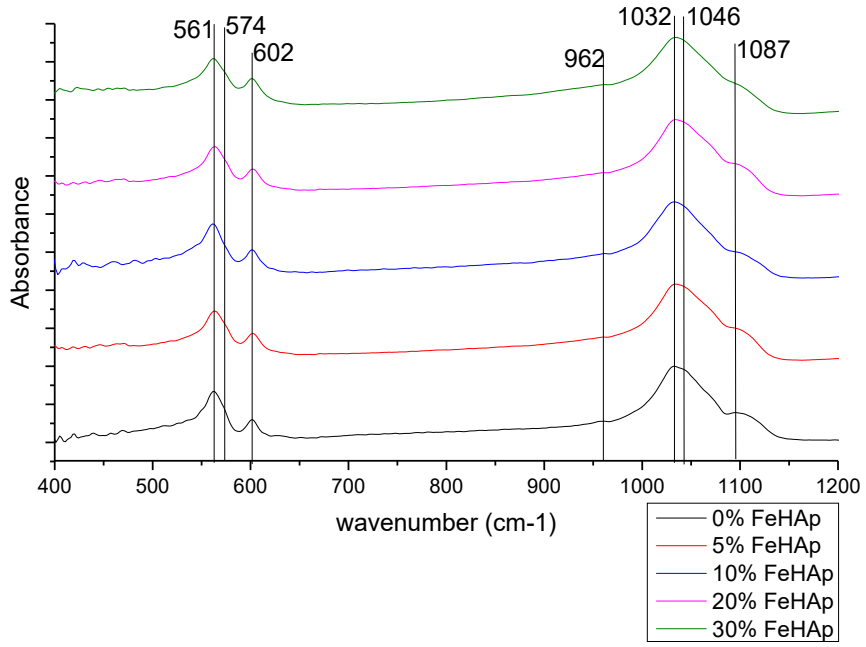

Figure 3.9: FTIR-ATR spectra of FeHAp powders for 1200-400cm^{-1}

A weak but present nondegenerate symmetric stretching mode, ν_1, at 962 cm^{-1} and the triply degenerated asymmetric stretching modes ν_{3c}, ν_{3b} and ν_{3a} at 1032, 1046 and 1087 cm^{-1}, respectively for the P-O phosphate group bond.

The hydroxyl group libration mode, ν_L, at the 631 cm^{-1} is not apparent in these spectra. The shallow broad band centred at 3572 cm^{-1}, Figure 3.10, of hydroxyl

group stretching, ν_s, is weak, however does seem to be increasing in intensity with increasing Fe^{3+} concentration, signifying increased hydroxyl retention. A similar trend is observable at the H_2O bending ν_2 at 1683 cm^{-1}.

C-O asymmetric stretching, ν_3, is present at ~2360cm^{-1}, which is consistent with atmospheric carbon dioxide. The two weak remaining peaks at 1432 and 1521cm^{-1} appear to be consistent with N-O asymmetric and symmetric stretching, signifying that the washing process after powder precipitation was not quite thorough enough at removing all the nitrates in the post solution out of the powders. However, these peaks are extremely weak, and therefore account for a very small amount of residual N-O, and can be considered negligible.

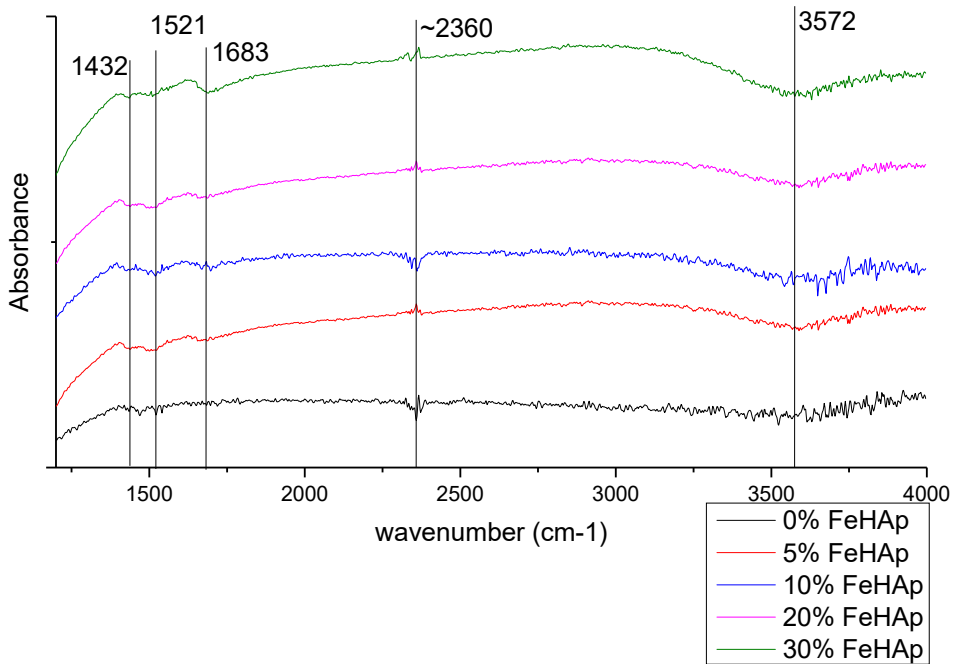

Figure 3.10: FTIR-ATR spectra of FeHAp powders for 4000-1200 cm^{-1}

Table 3.5: Infrared absorption peaks and their assignments

Peak (cm-1)	Assignment	Reference
1087	Triply degenerated asymmetric stretching mode, ν_{3a}, of the P–O bond	[142]
1046	Triply degenerated asymmetric stretching mode, ν_{3b}, of the P–O bond	[142]
1032	Triply degenerated asymmetric stretching mode, ν_{3c}, of the P–O bond	[142]
962	Nondegenerated symmetric stretching mode, ν_1, of the P–O bonds	[142]
631	Librational mode, ν_L, of the hydroxyl group	[172]
602	Triply degenerated bending mode, ν_{4a}, of the O–P–O bonds	[142]
574	Triply degenerated bending mode, ν_{4b}, of the O–P–O bonds	[142]
561	Triply degenerated bending mode, ν_{4c}, of the O–P–O bonds	[142]
3572	Stretching mode, ν_s, of the hydroxyl group	[172]
1630	Bending mode, ν_2 , of water	[172]
2360	Asymmetric stretching, ν_3, C-O bond	[172]
1410-1550	Asymmetric, ν_3, and symmetric, ν_1, bending of N-O bonds.	[173]

Table 3.5 shows the peak position and assignment for infrared spectra, and their references.

There is no observable shift in the peaks with increasing Fe^{3+} content of the FTIR spectra, which implies that there is little effect on the phosphate vibrational modes in the structure. This might be expected as there would be little change to the mass and therefore dipole rovibrational state of the phosphate ion. The increase of hydroxyl ion intensity at ~3600cm^{-1} and lack of, or extremely weak, libration mode at 631cm^{-1} does suggest that despite increasing water content, the hydroxyl ion is bound in its degrees of freedom.

3.3.5 Raman spectroscopy

Raman spectroscopy was obtained with a Renishaw InVia Raman microscope with a 514nm diode pump source. No fluorescence peaks or abnormalities in the Raman spectra are observed, Figure 3.11, and so it can be concluded that

there is little or no radiative emissions from the samples whilst being pumped at 514nm. Heating of the sample due to absorption of the pump source, may shift the vibrational Raman mode, as we might expect more linear absorption with increasing doping concentration.

There are relatively strong peaks around 1046, 961, 594 and 447cm^{-1} across all samples, which are consistent with phosphate group P-O bond ν_3, ν_1 and O-P-O bond ν_4 and ν_2 modes respectively [174].

There is a shift in the peaks tending towards longer wavenumbers in all the doped samples, signifying either heating of the sample, or an effect on the phosphate group inherited from higher doping concentrations.

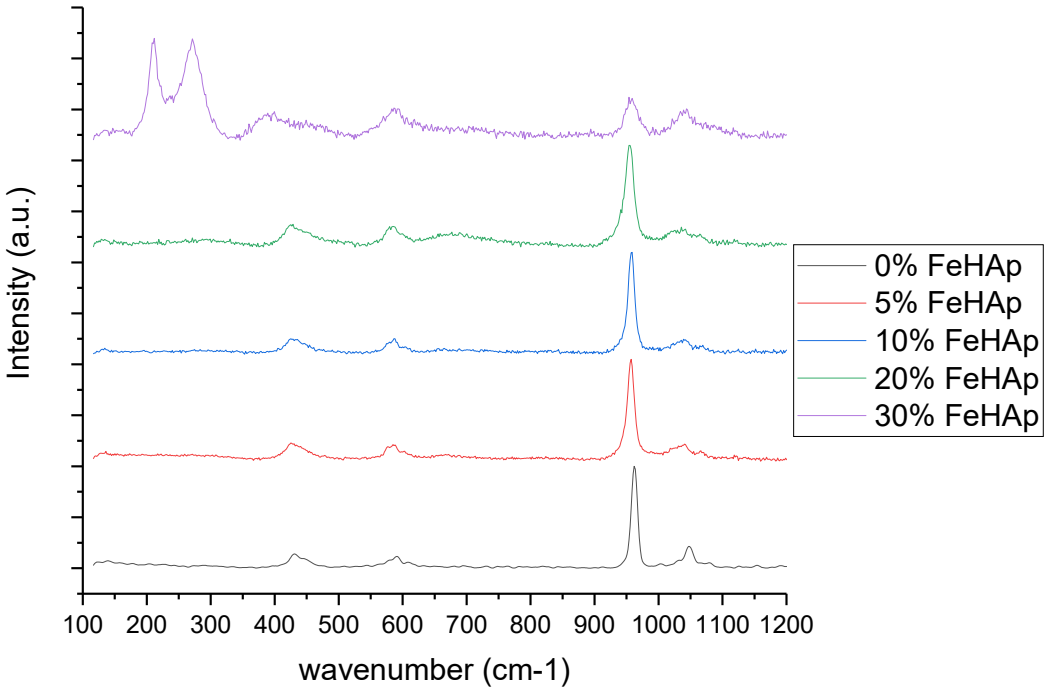

Figure 3.11: Raman spectra of the FeHAp powders

Since Raman depends on the change of the polarizability of the vibrating molecule, in comparison the case of FTIR which depends on the change in the dipole moment, Raman is clearly the more effective method to determine the effect of Fe^{3+} has within the structure of the hydroxyapatite.

The increased water content as apparent from the FTIR and shift in peaks of the Raman spectra, could also mean that the trivalent Fe^{3+} cation is harbouring extra hydroxyl ions around the crystal structure, which inhibit the polarisation and movement of the phosphate groups, creating the trend seen in these spectra. This is certainly prominent in the 30% FeHAp sample, where the lower ionic lattice vibrations of 210cm-1 and 270cm-1 represent α-FeO(OH) bond frequencies and therefore dominate the reciprocating polarizability of the medium [175], as the phosphate group peak is greatly dampened. Why this occurs suddenly only at 30at% Fe^{3+} and not at lower concentrations is inconclusive.

Saturation of hydroxyl ions into the structure would explain the loss in XRD crystallinity and coherence, it might also be expected to net an effect of the phosphate ion. Since the peak shifts are not correlated with Fe^{3+} doping concentration, the shifts can be explained through heating. However, the lack of hydroxyl vibrational modes in the Raman spectra confirm the FTIR, little to no libration of the molecule is observed, indicating weak polarizability of the polar molecule, and that it must only be in the species, ^{-}OH. If water is expected in the structure, strong Raman peaks at ~3400cm^{-1} should be observed.

3.3.6 UV-vis-NIR

Diffuse reflectance was measured by a UV-vis spectrometer (Perkin-Elmer Lambda 950 UV/Vis/NIR) from 250-2500nm in an integrating sphere with the sample held at 8° from incidence for spectral and diffuse reflection collection. UV-vis-NIR reflection spectroscopy is shown in Figure 3.12, where it can be observed that there are several absorption peaks. The broad peaks centred around 1900 and 1430nm represent combinations of hydroxyl overtone modes, $av_1 + v_2 + bv_3$; a+b=1 and $v_1 + bv_3$; a+b=2 respectively [135]. At 1433nm, there is a sharp peak in the 0% doped HAp, this peak is apparent but not distinct in the remaining samples, indicating that the more valent Fe^{3+} ions in the structure constrict the hydroxyl resonance at this particular overtone combination. Which confirms somewhat the observations in the FTIR and Raman.

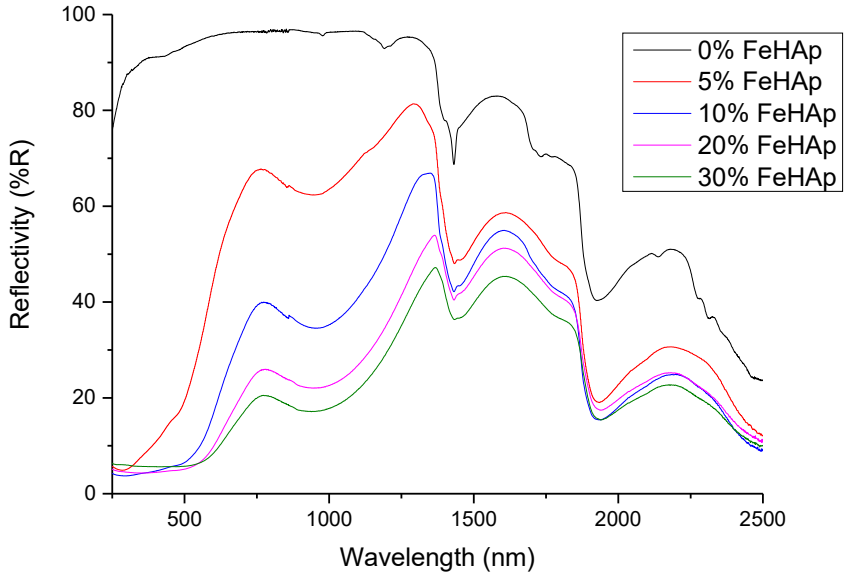

Figure 3.12: UV-vis-NIR spectroscopy of the powders

The broad trough centred on 950nm appears only in the doped samples, meaning that this absorption peak is due to Fe^{3+} in the structure. This is in

agreement with the non-radiative $^4T_{1g} \rightarrow {}^6A_{1g}$ state of Fe^{3+} [164], [166], where a high number of transitions are available, accounting for the broad nature of the peak. This peak also appears to reduce in reflectivity with increasing doping levels. Which demonstrates that increased doping levels increases absorption properties. All samples also demonstrate decreasing reflectivity from 1350-2500nm, with doped samples extending further decreases. This suggests that either broadband absorption is occurring, or that there is increased losses into the sample. As the measurement is taken by an integrating sphere it can be assumed that all of the signal would be reciprocated as reflectance as the sample is not opaque throughout bandwidth. The decreasing slope in reflectivity would not then represent scattering or any other means of losses in the sample and can be attributed to the increased water or hydroxyl vibrations in the NIR where the absorption coefficient in this region increases by three orders of magnitude [135]. Doped samples thereby displaying further hydroxyl broadband overtone modes than in the un-doped sample, suggesting increased hydroxyl content.

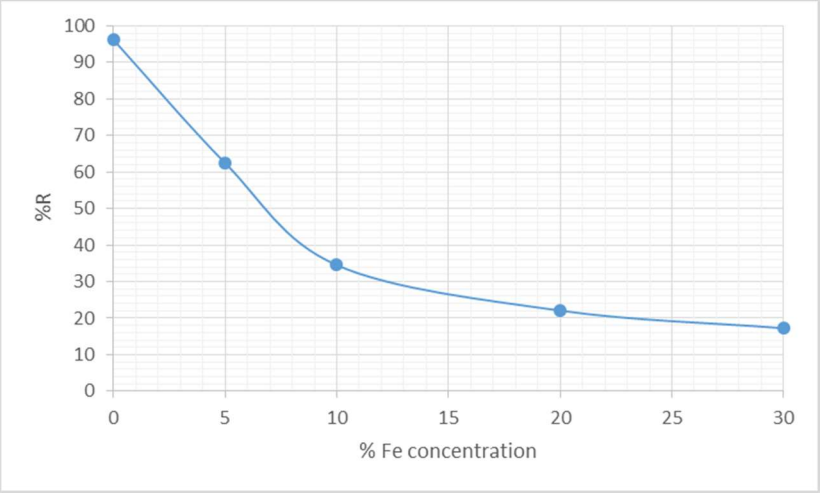

Figure 3.13: % Reflectivity for % Fe^{3+} concentration at 950nm.

Total energy absorbed is therefore representative of the un-reflected part of the beam; 1-R. Absorption of the light appears to saturate as we tend towards >30at% Fe^{3+}, further doping regimes would therefore likely do little to increase the absorption properties; Figure 3.13.

3.3.6.1 Kubelka-Munk

Conversely, it is somewhat unjustified to measure the absorbance solely through %R spectra, as there are many ways in which photons might end up at the detector. A photon may reflect between many layers of the opaque medium without and absorption event, and therefore cannot be attributed to the absorbance value through 1-R. Figure 3.14 illustrates this, showing that the net reflectance will clearly be a sum of reflections and transmission of reflections between the subsequent layers of the material.

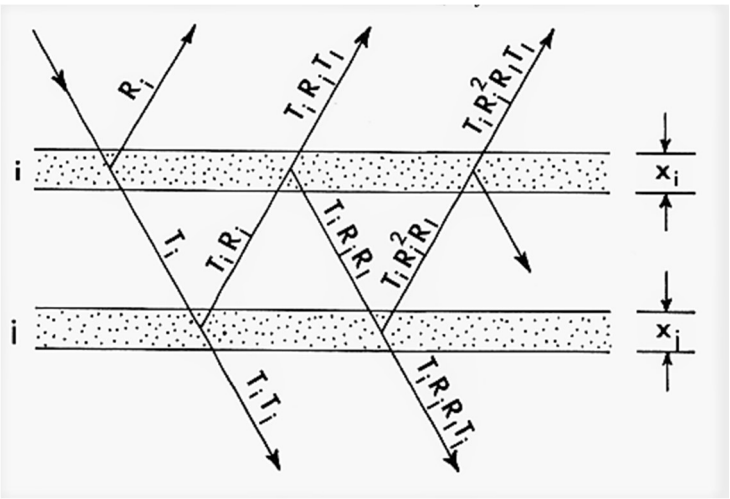

Figure 3.14: Methods of reflected attenuation and transmission[176]

It is therefore necessary to implement Kubelka-Munk diffuse reflectance theory to be able to analyse the UV-vis-NIR data more thoroughly. The theory is based upon modelling two radiant fluxes, one which travels from an illuminated sample surface, and another travelling toward it. As the radiant flux travels from

the surface, it is clear that it will decrease by any scattering or absorption events that occur, which will be proportional to the depth into which the radiation can penetrate the medium.

The absorption of a single layer, a, will then be represented:

$$a = \frac{S + K}{S} \tag{3.5}$$

Where S and K are phenomenological constants that describe scattering and absorption, respectively. The rate of change of radiant fluxes with respect to scattering of the medium will be dependent on the rate of change of reflection:

$$\frac{dR}{Sdx} = R^2 - 2aR + 1 \tag{3.6}$$

As R is essentially the ratio between the radiant fluxes. If we integrate this equation to then find the reflectance of a layer which is thick enough so any increase in thickness results in no further increase of reflectivity, we can see:

$$R_\infty = a - (a^2 - 1)^{1/2} \tag{3.7}$$

We can then substitute equation 3.5 to rearrange for the Kubelka-Munk function $F(R_\infty)$ [177]:

$$F(R_\infty) = \frac{(1 - R_\infty)^2}{2R_\infty} = \frac{K}{S} \tag{3.8}$$

We can use this function on the reflectivity data, in order to ascertain the relative absorbance, Figure 3.15. In several studies, it has been found that the scattering coefficient in this term is inversely proportional to the particle diameter [178], [179], and maybe approximated in this manner to obtain the attenuation coefficient of the material.

In Figure 3.15 it is more apparent the description of the high energy limbs centered on ~300nm, $^6A_1 \rightarrow {}^4A_1\,{}^4E(G)$ transition, that almost obscure the much weaker d-d spin forbidden transitions centered at 950nm, representing the $^4T_{1g} \rightarrow {}^6A_{1g}$ transition. The change in relative absorbance at this band appears much more evenly spread, with dopant level, in comparison to the raw reflectivity measurements.

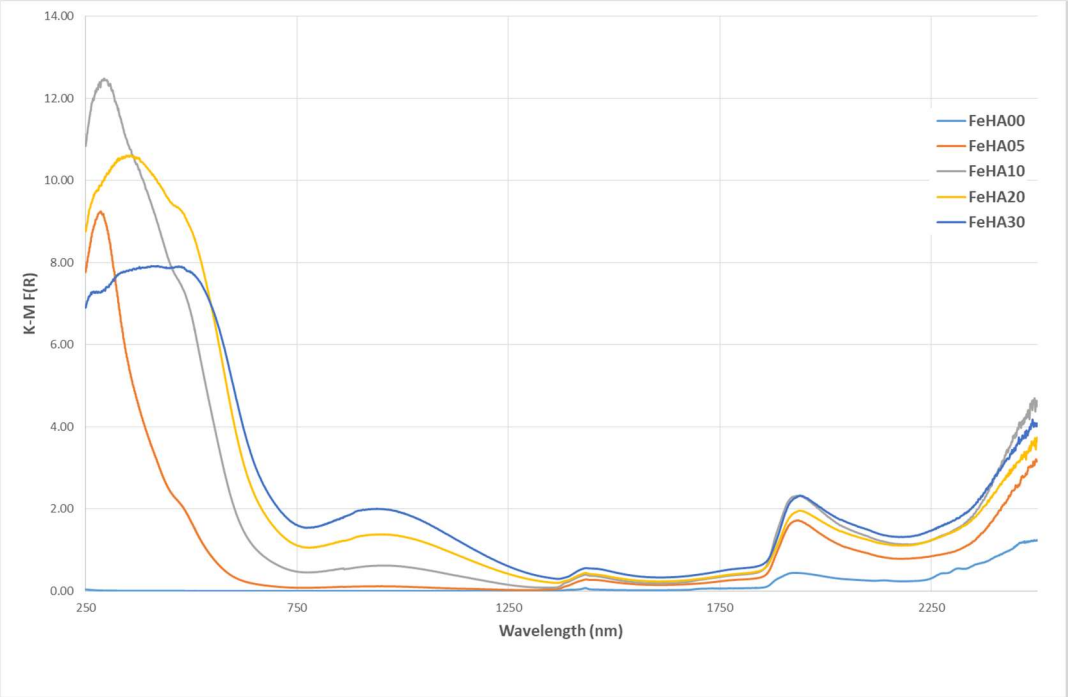

Figure 3.15: Kubelka-Munk function for the reflectivity data of the powders

3.3.6.2 Tauc analysis

Tauc analysis was completed utilising the Kubelka-Munk function as this is directly proportional to the absorption coefficient values, in an attempt to determine the optical bandgaps of the different materials. The direct allowed transitions and indirect allowed transitions are shown in Figure 3.16 and Figure 3.17, respectively.

The accuracy of this data is questionable due to the fact that it can be observed in Figure 3.15 that in the UV the curves tail back toward abscissa, signifying that this is not quite the UV band edge. 250nm is the lowest wavelength that the detector in the integrating sphere can achieve, and so it was not possible with this set up to scan any lower wavelengths.

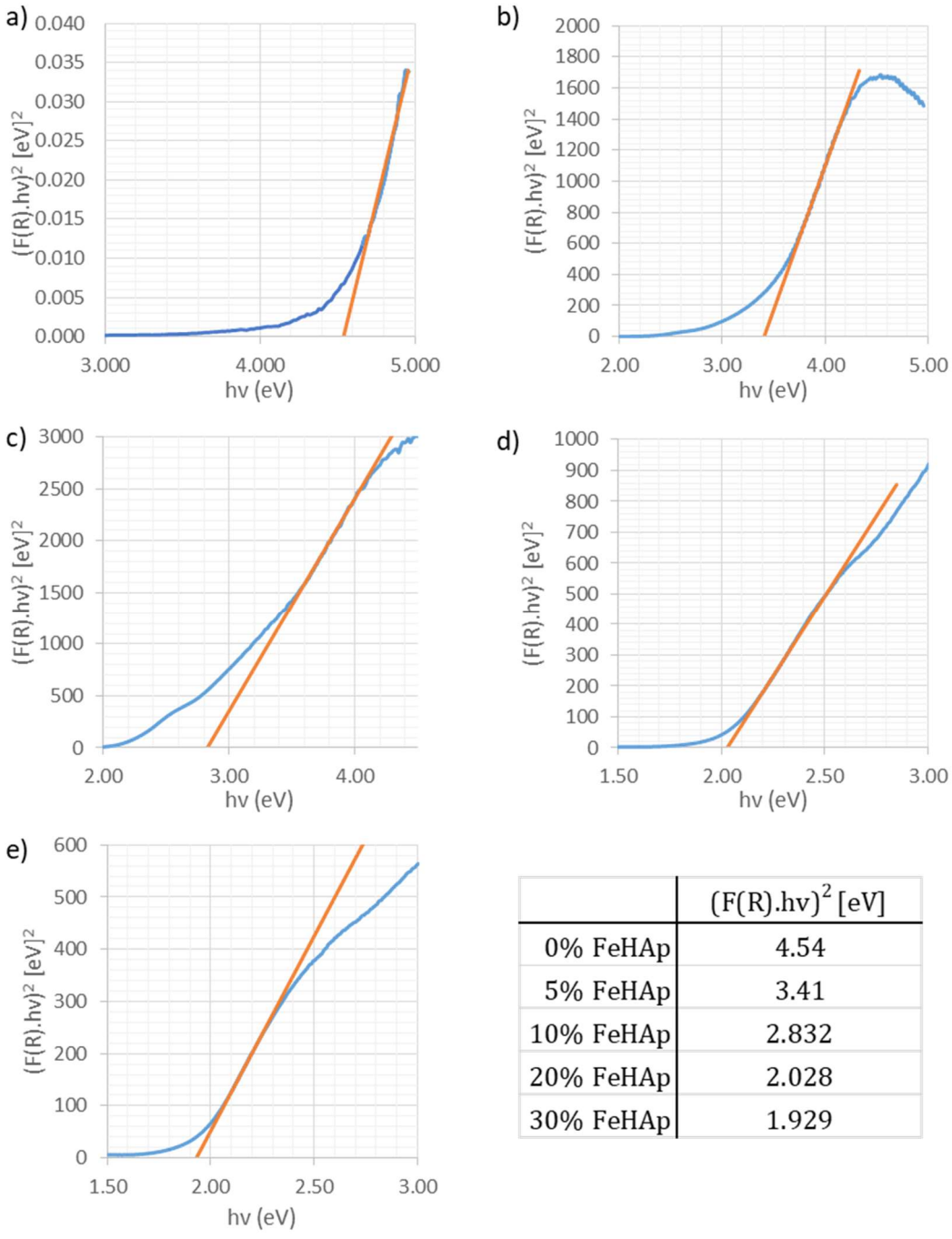

	$(F(R).hv)^2$ [eV]
0% FeHAp	4.54
5% FeHAp	3.41
10% FeHAp	2.832
20% FeHAp	2.028
30% FeHAp	1.929

Figure 3.16: Direct allowed transitions measurements

Nonetheless, the 0% FeHAp sample will likely represent the nearest result to the UV band edge as it does begin to tail at 250nm, giving a transition energy of 4.54 eV, not far from reported ~5eV band gap from Bystrov et al. [180]. Leading the belief that deeper in the UV the remaining absorption plots would join this band edge, effectively giving the remaining doped samples the same band gap.

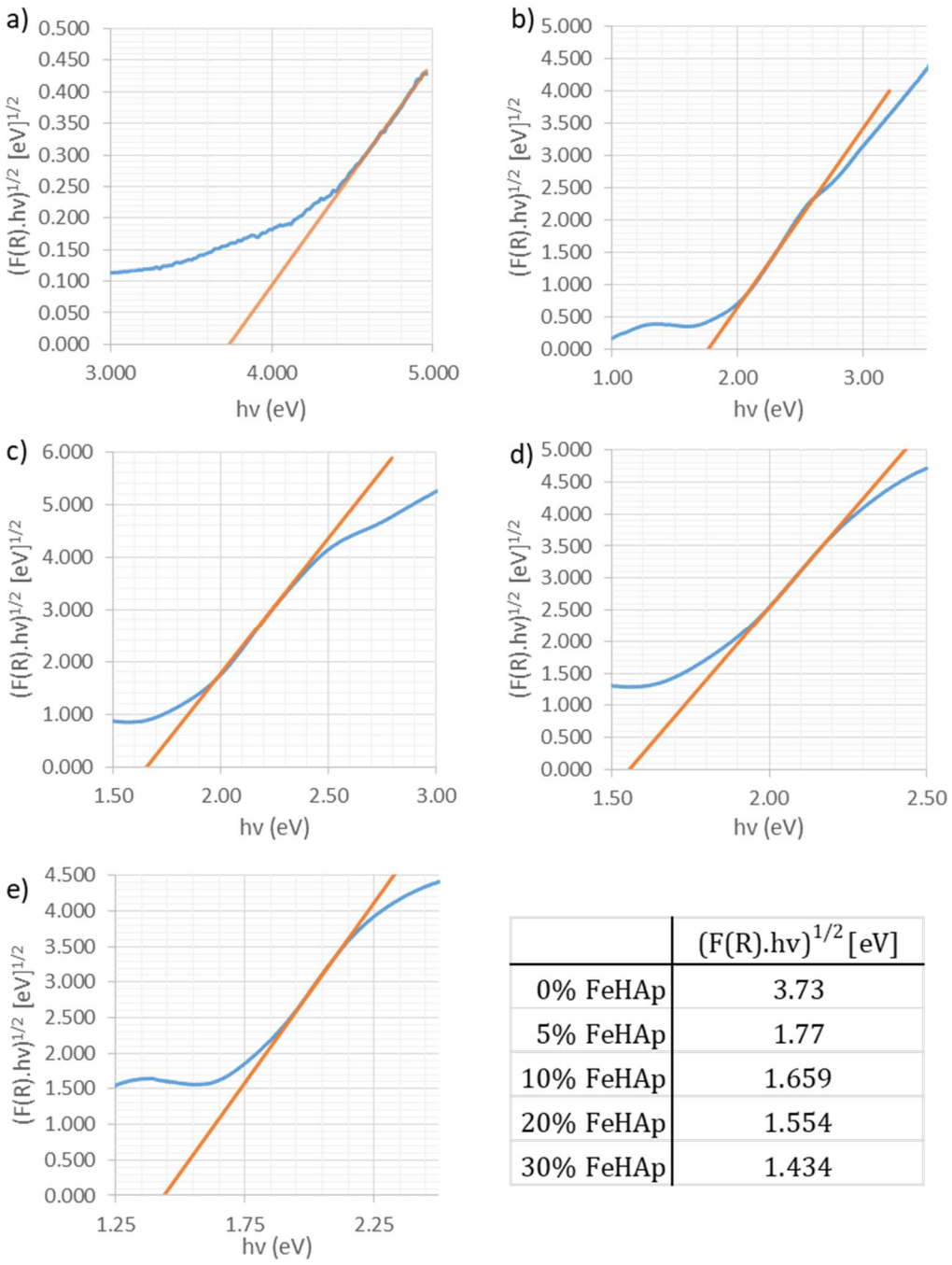

	$(F(R).hv)^{1/2}$ [eV]
0% FeHAp	3.73
5% FeHAp	1.77
10% FeHAp	1.659
20% FeHAp	1.554
30% FeHAp	1.434

Figure 3.17: Indirect allowed transition measurements

The trend across doped samples show decreasing values of direct and indirect transition energy is therefore modelling the $^6A_1 \rightarrow {}^4A_1\,{}^4E(G)$ transition, and shows that increasing doping concentrations allows for increased population of this transition. Thereby spreading the edge of the transition through the Stark effect [181], which is what should be expected with increased Fe^{3+} concentration in the crystal field.

3.3.7 Fluorescence spectroscopy

Steady state fluorescence measurements were taken with an Edinburgh instruments FLS920 fluorescence spectrometer with near infrared photomultiplier tube and pumped using a commercial 980nm diode excitation source. This was taken to confirm if any radiative decays were present after the addition of iron into the hydroxyapatite complex. Figure 3.18 shows the fluorescence spectra for 30% FeHAp, showing a peak only at the pump wavelength of 980nm, which is a reflection from the sample, and no other degenerate peaks of emission, confirming that any absorbed energy at this wavelength, and in the $^4T_{1g} \rightarrow {}^6A_{1g}$ transition will decay non-radiatively.

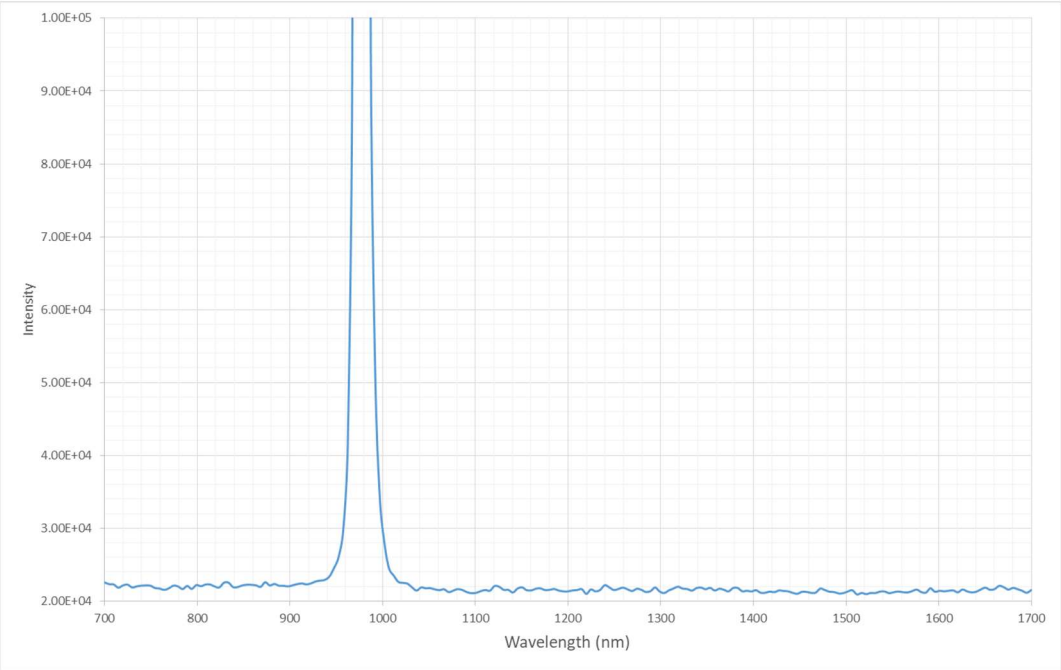

Figure 3.18: Fluorescence spectra for 30% FeHAp

3.3.8 Thermal analysis

Thermal analysis of the powders was carried out with a Perkin Elmer Simultaneous thermal analyser (STA) 8000, at a rate of 50 °C/min heating rate up to 1450°C in air. Thermo-gravimetric analysis (TGA) can be seen in Figure 3.19 and shows that the mass loss up to 500°C scales with doping concentration, where in all cases it then tails off to a drop in mass until at about 750°C. This then continues to slope modestly until 1375°C where there is then an apparent increase in mass in all but 20-30% FeHAp samples.

Less than 200°C, absorbed water is removed from the surface of hydroxyapatite, and then from temperatures up to 500°C interstitial water is removed from any pores in the material, which describes the immediate mass loss as seen in Figure 3.19. Structural water is then slowly released upon further heating up to >900°C. Where slow conversion of the hydroxyapatite to α-TCP until ~1350°C

where there is complete conversion to TCP [182]–[185]. This confirms the conclusions made earlier that increasing doping concentration lead to increased absorption of water into the structure, as the mass loss of higher doping concentration is far larger than in less doped samples.

Differential thermogravimetric (DTG) analysis, Figure 3.20, shows further the mass losses peaking around 100°C, which should expect if it were water held within the structure. This is followed by a secondary peak centred at 500°C up to 600°C, this demonstrates the loss of interstitial water within the crystal structure. A major peak at 775°C is then apparent, this further mass loss is due to further dehydration and rearrangement to HPO_4- groups [186], followed by complete decomposition into α-TCP at 1350°C.

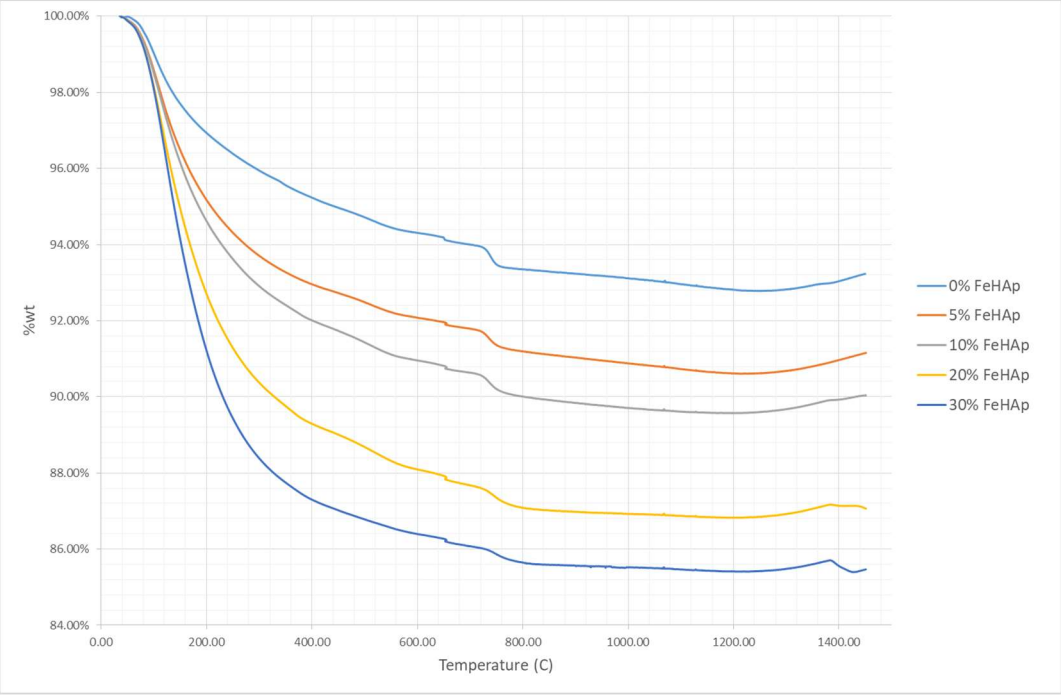

Figure 3.19: TGA of the doped hydroxyapatite powders

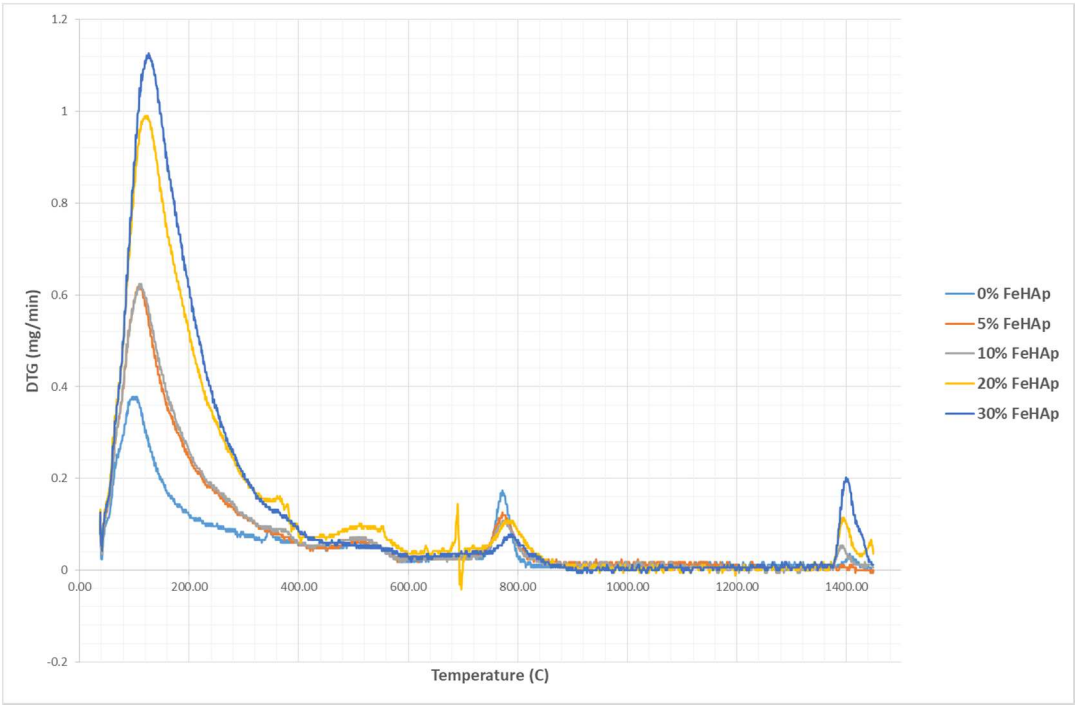

Figure 3.20: DTG of the doped hydroxyapatite powders

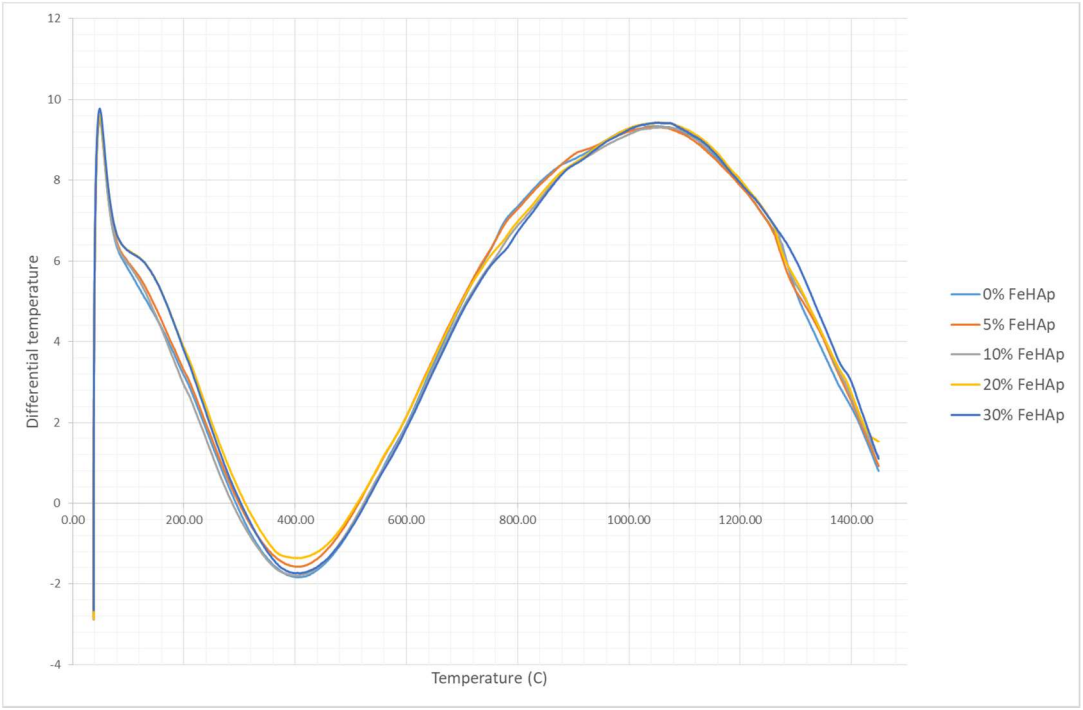

Figure 3.21: DTA of the doped hydroxyapatite powders

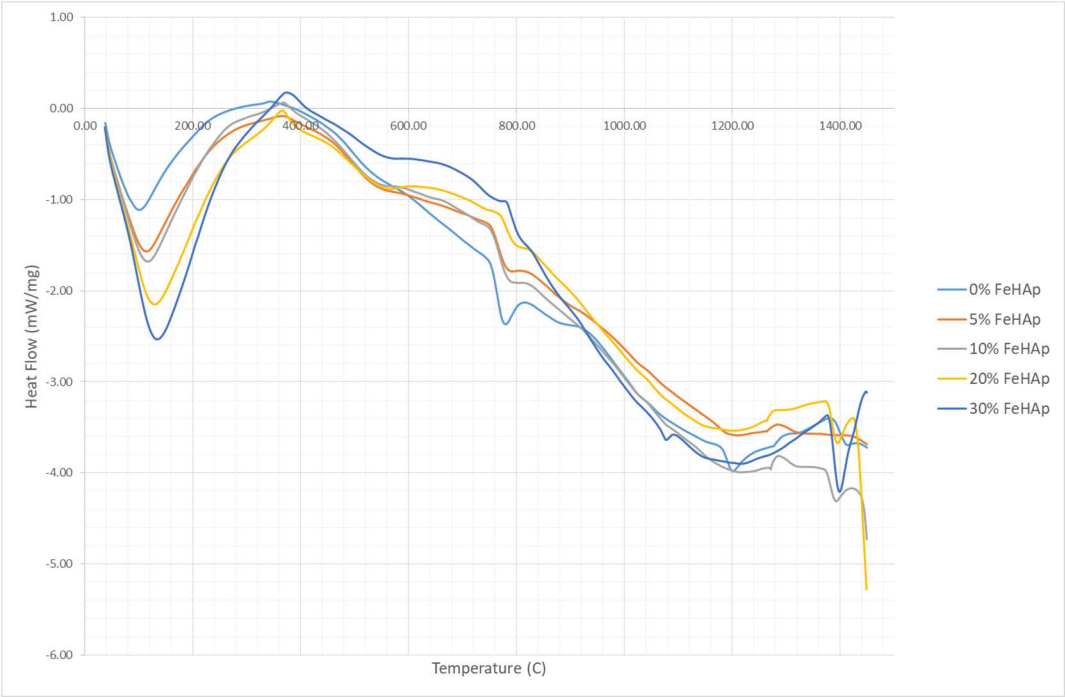

Figure 3.22: DSC of the doped hydroxyapatite powders

Differential thermal analysis (DTA) and Differential scanning calorimetry (DSC) of the powders are displayed in Figure 3.21 and Figure 3.22, respectively, the DSC showing two broad endothermic peaks. The initial parts of the peaks, under 600°C, will be attributed to evaporation of water within the samples, as can be confirmed with the mass loss. Post 600°C, this long peak that centres at ~1200°C will be due to the decomposition of the structure into β-TCP.

The DTA curve is fairly homogenous across all samples, with a slight accentuation of knee present <200°C. Variance within this data is likely due to the sensitivities of the instrument.

The DSC curve shows increasing endothermic peaks, <400°C, with increasing doping concentration. Since the measurement has been converted to relative mW/mg, this demonstrates that there is more enthalpy required in evaporating 1mg of water from higher than lower doping concentration. The difference in

valence and electrostatic equilibrium of crystallites due to the Fe^{3+} substitution into the hydroxyapatite structure evidently aids in hydroxyl retention.

The further peak up until <600°C can be attributed to further interstitial water loss, however, there is a slight difference in the 30% FeHAp sample only, where less enthalpy is apparently required for this section. The samples then seem to diverge slightly, creating the characteristic peak at 775°C toward rearrangement to HPO_4- groups. The divergence is due the reaction kinetics and the relative stoichiometry of the materials, decomposition of iron doped hydroxyapatite to calcium iron phosphate is most stoichiometric at 10% FeHAp doping concentrations ($Ca_9Fe(PO_4)_6(OH)_2 \rightarrow Ca_9Fe(PO_4)_7$) and only requires adsorption of another phosphate group. Outside of this stoichiometry, more or even less energy is likely to be absorbed to instigate the decomposition, depending on the remnant components of the solid state reaction. Clearly this is more favourable for higher doping concentrations, where the increased valence, has beneficial reaction entropy. However, this does not necessarily have a net effect over the whole decomposition.

Table 3.6 shows the required enthalpy from the DSC curve for the different parts of the major peaks. Dehydration of the material shows a positive correlation with increasing doping concentration. However, there appears to be little correlation for the overall enthalpy of decomposition across the samples.

Table 3.6: Enthalpies of Fe doped HAp's from DSC

	0% FeHAp	5% FeHAp	10% FeHAp	20% FeHAp	30% FeHAp
Enthalpy of dehydration (J/g)	-267.74	-305.35	-375.27	-456.15	-529.92
Enthalpy of decomposition (J/g)	-2440.95	-2125.74	-2477.45	-2094.51	-2378.89
Total Enthalpy (J/g)	-2708.69	-2431.09	-2852.72	-2550.66	-2908.81

The DSC curve also shows mild peaks centred at 1076°C and 1200°C for only the 30% FeHAp and 0% FeHAp, respectively. It was considered that this was due to the formation of an iron phase, however, since this also occurs to a relative scale, only at a higher temperature for the undoped sample, it can be attributed to a further phase change to a tetracalcium phosphate (TTCP: $Ca_4O(PO_4)_2$) which occurs in the region 1100-1200°C [187]. No change in the remaining samples here, demonstrates a doping concentration range of thermal stability.

At 1300°C there is then a mild exothermic peak, which suggests some form of crystallisation is occurring prior to the final decomposition to α-TCP at temperatures above 1360°C.

3.3.9 Heated XRD

Heated X-Ray diffraction spectra were collated with the Philips X'Pert diffractometer with CuKα emission source (0.1541nm) at 40 keV and 40 mA, with a water cooled hot stage that could heat target powder at 600, 700, 800, 900 and 1000°C at a rate of 50 °C/min.

Figure 3.23 shows such a spectra for 0% FeHAp sample, it can be seen that there is little change between the room temperature spectra and the 600°C, as we might expect given that this heating regime only results in dehydration of the

material. Heating further, at 700°C, it can be seen that there are now very clear peaks associated with tricalcium phosphate (peak list Table 3.7).

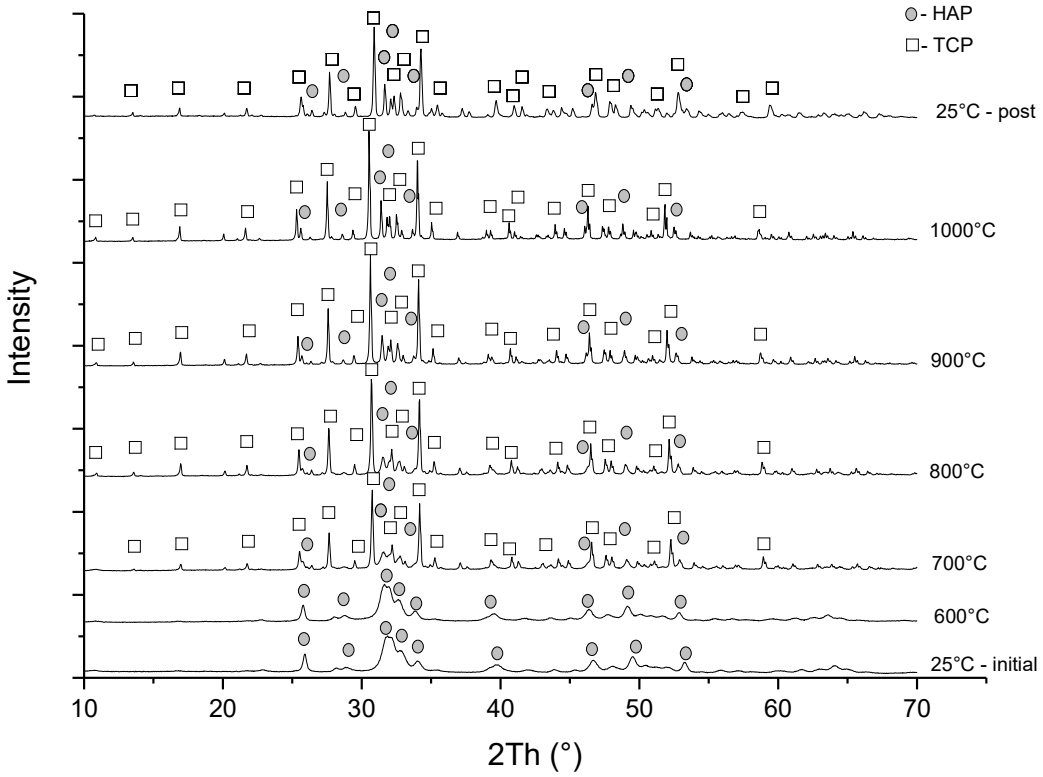

Figure 3.23: XRD spectra for 0% FeHAp over different temperatures.

Table 3.7: Major peak list for Tricalcium phosphate (JCDPS #01-7220)

Tricalcium Phosphate ($Ca_3(PO_4)_2$)

No.	h	k	l	d [A]	2Theta[deg]	I [%]
1	0	1	2	8.1247	10.881	11.7
2	1	0	4	6.4881	13.637	17.8
4	1	1	0	5.21	17.005	21.1
8	0	2	4	4.0624	21.861	11.5
10	1	0	10	3.4503	25.801	24.6
15	2	1	4	3.2036	27.826	59.7
18	3	0	0	3.008	29.676	12.6
19	0	2	10	2.8767	31.063	100
20	2	1	7	2.8767	31.063	100
21	1	2	8	2.7538	32.487	20.6
24	2	2	0	2.605	34.399	69.3
27	2	1	10	2.5183	35.622	11.8
40	4	0	4	2.1929	41.13	10.2
41	3	0	12	2.1627	41.731	11.7
55	4	0	10	1.9309	47.023	24.9
56	3	2	7	1.9309	47.023	24.9
57	2	3	8	1.8924	48.039	15.3
58	1	4	6	1.8774	48.448	13.3

Table 3.8: Major peak list for Calcium Iron phosphate (JCDPS #05-6336)

Calcium Iron Phosphate ($Ca_9Fe(PO_4)_7$)

No.	h	k	l	d [A]	2Theta[deg]	I [%]
1	0	1	2	8.0922	10.925	37.5
2	1	0	4	6.467	13.682	43.7
4	1	1	0	5.1866	17.082	27.3
8	0	2	4	4.0461	21.95	11.6
10	1	0	10	3.4424	25.861	18.9
15	2	1	4	3.1902	27.945	48.5
18	3	0	0	2.9945	29.813	9.4
19	0	2	10	2.8682	31.158	100
20	2	1	7	2.8682	31.158	100
21	1	2	8	2.744	32.607	22.1
24	2	2	0	2.5933	34.559	66.7
27	2	1	10	2.51	35.744	9.5
41	4	0	4	2.1833	41.319	9.8
42	3	0	12	2.1557	41.873	10.3
55	4	0	10	1.9236	47.212	21.9
54	2	1	16	1.9236	47.212	21.9
56	2	3	8	1.8848	48.245	10.5
57	1	4	6	1.8695	48.666	11.8
67	2	0	20	1.7212	53.171	22.7

However, the hydroxyapatite peaks are still prominent up until 900°C, which is in contention with the literature [183]. Turning mainly to β-TCP at 1000°C, and maintaining these peaks upon cooling, but still with some hydroxyapatite constituent at this temperature. Reitveld analysis of the residual patterns reveals that the post processed room temperature material still consisted of 23% hydroxyapatite.

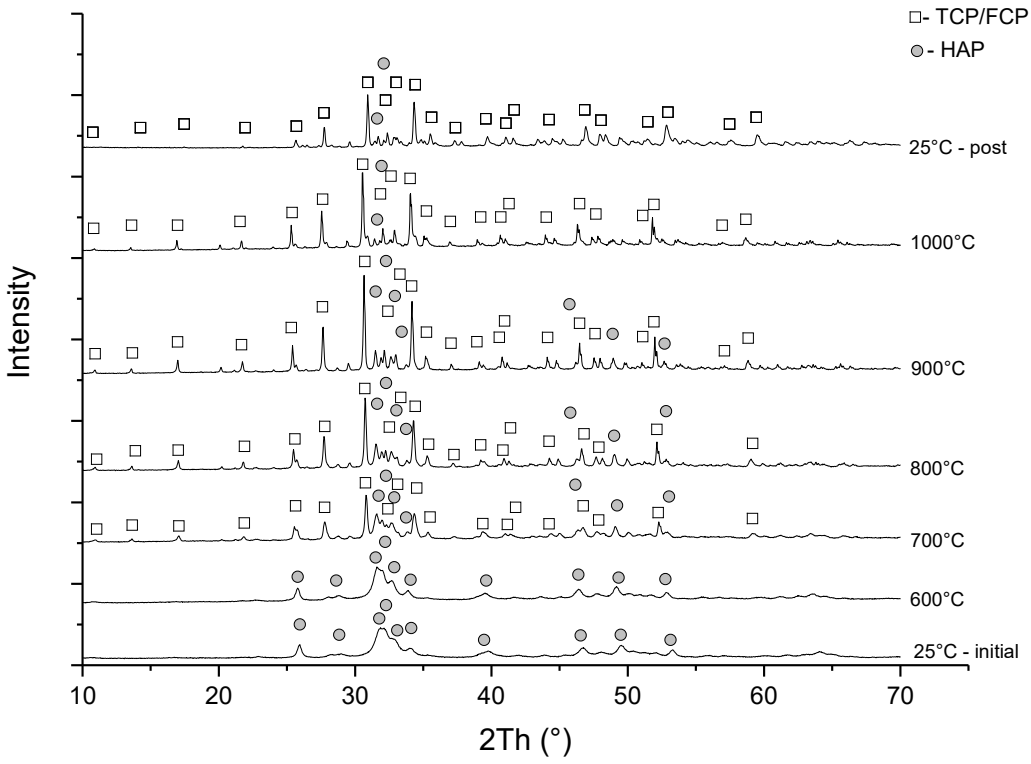

Figure 3.24: XRD spectra for 5% FeHAp over different temperatures

The 5% FeHAp XRD spectra, Figure 3.24, showed some similarities to the 0% FeHAp results, in the general trend to the pattern, however, the peak intensities for the 5% FeHAp appear somewhat reduced, signifying less crystalline product. This is evidently due to the incorporation of Iron into the structure, part of the product will form calcium iron phosphate (FCP), whereas the remainder will form the β-TCP phase, which presents a problem when trying to analyse the

final product due to the incredible similar peak values for FCP and β-TCP. As can be seen in comparing Table 3.7 and Table 3.8, the peak value centres are almost identical, with mild variance in intensity values. Ascertaining any exact value of the composition of the heated product is then not trivial, as well as the value of the remaining hydroxyapatite in the crystal structure.

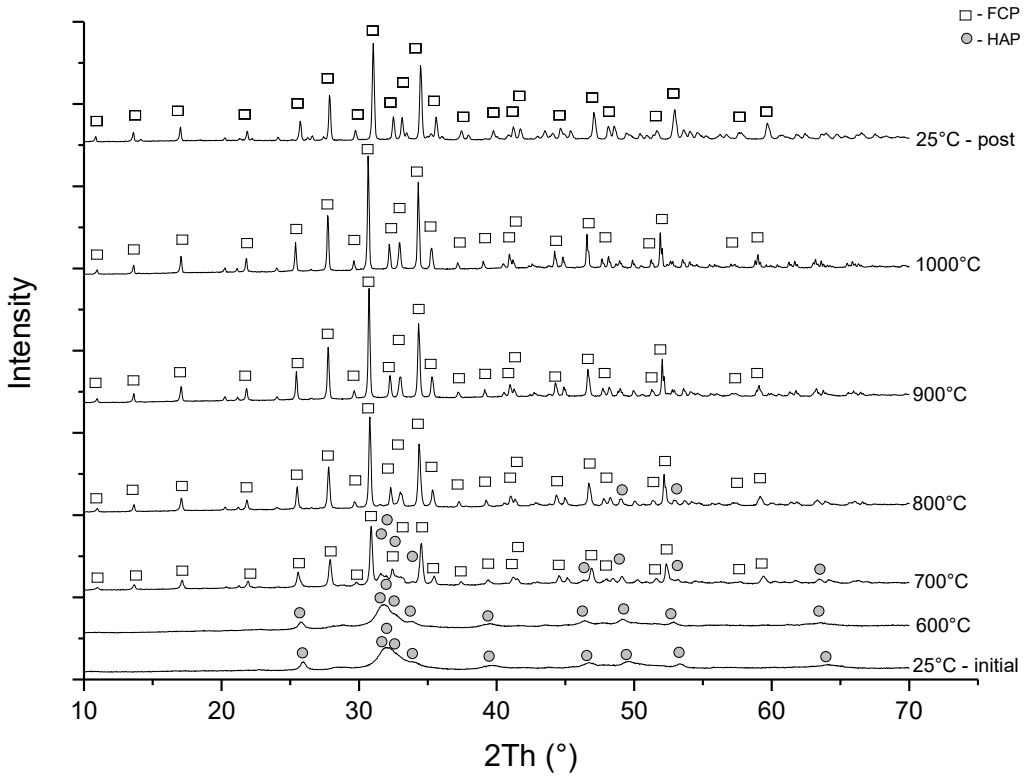

Figure 3.25: XRD spectra for 10% FeHAp over different temperatures

The spectra for the heated 10% FeHAp, Figure 3.25, has strong peaks across the scanning range and generally appears more uniform after 800°C. This is likely due to the stoichiometry present with the Fe^{3+} at 10at.% into the FCP structure causing no required secondary phases of calcium based phosphate phase, in this manner it is far more probable to stimulate crystal growth and coherence in the diffraction scan, without any disruptive valence differences or out of equilibrium phases.

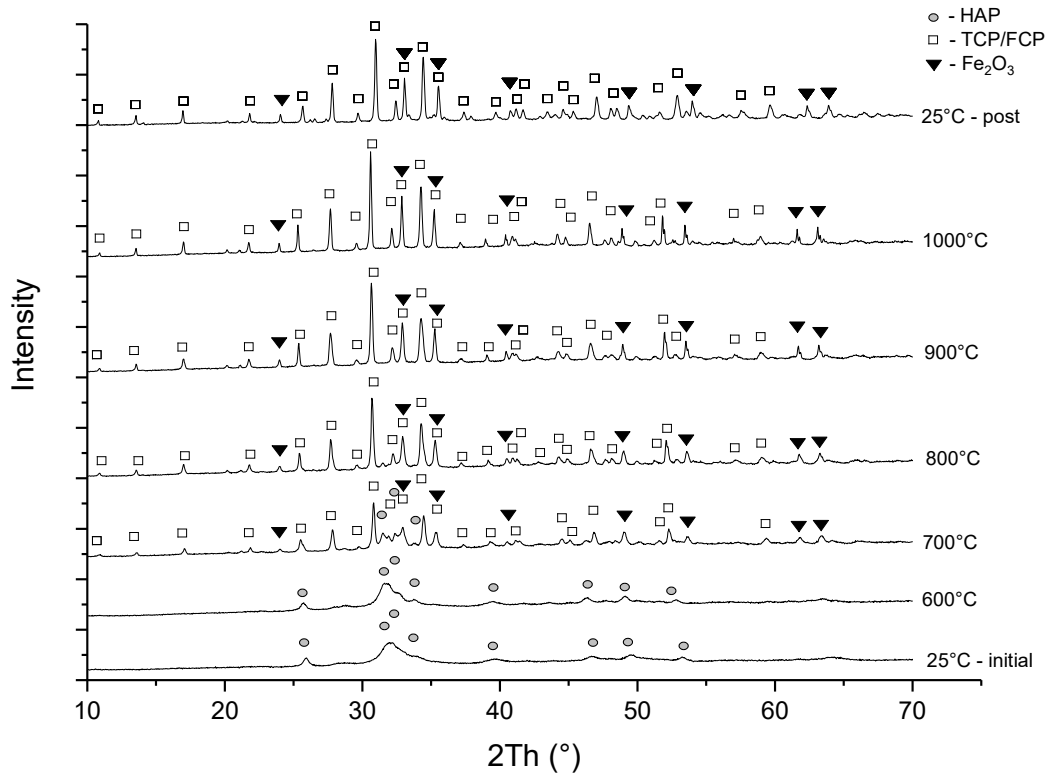

Figure 3.26: XRD spectra for 20% FeHAp over different temperatures

The spectra for the 20% FeHAp sample, Figure 3.26, shows a similar result to the 5% FeHAp, where the peak intensity seems dampened and hydroxyapatite peaks seem relative to the major FCP/β-TCP. However, there are some further peaks with enhanced intensity. This is due to a contribution from hematite, which has high intensity peak centres at 33.152 and 35.612,

Table 3.9, which complements the (2110) planes of the FCP/TCP mixture. This is also apparent for the (012) and (116) hematite planes, where a peak at 24.14 and 54.056 is now present in the spectra, which was not present in the previous doping concentrations. The remaining identifiable peaks appear to be obscured by the FCP/TCP mixture and therefore does not make determining the relative quantities of this product a favourable method of analysis.

Table 3.9: Major peak list for Iron Oxide (JCDPS #06-8177)

Iron Oxide (Fe_2O_3)

No.	h	k	l	d [A]	2Theta[deg]	I [%]
1	0	1	2	3.6838	24.14	42.8
2	1	0	4	2.7001	33.152	100
3	1	1	0	2.519	35.612	79
5	1	1	3	2.2076	40.844	21.1
7	0	2	4	1.8419	49.443	34.1
8	1	1	6	1.6951	54.056	52.3
13	3	0	0	1.4544	63.961	26.5

The spectra for 30% FeHAp, Figure 3.27, shows a very similar trend to the 20% FeHAp sample, where there is still more accentuation of the hematite peaks and mild reduction in relative intensity of crystalline FCP.

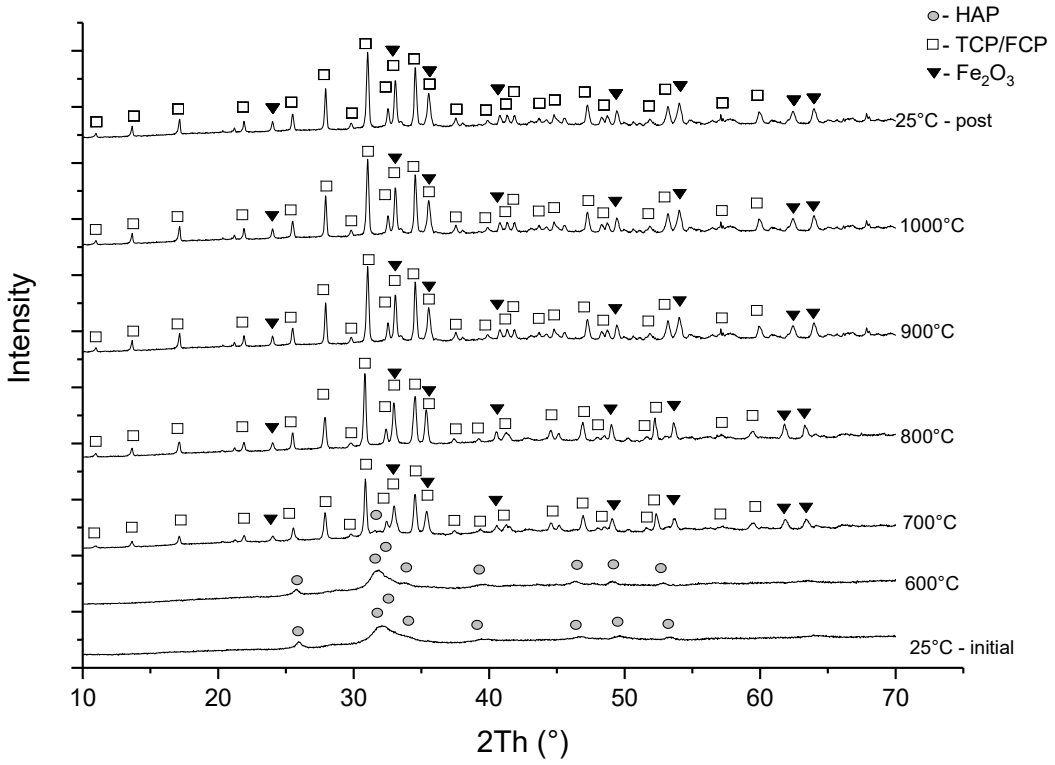

Figure 3.27: XRD spectra for 30% FeHAp over different temperatures

Figure 3.28 shows a comparison of all the resultant heated products at room temperature. The 0% FeHAp has produced a very crystalline by product, however, there is still a constituent hydroxyapatite part. Further heating of the powder to 1350°C would provide a full conversion to TCP. 5% FeHAp shows a less crystalline similar trend, however, still remnant (211), (112) and (300) hydroxyapatite peaks at 31.821, 32.292 and 32.940.

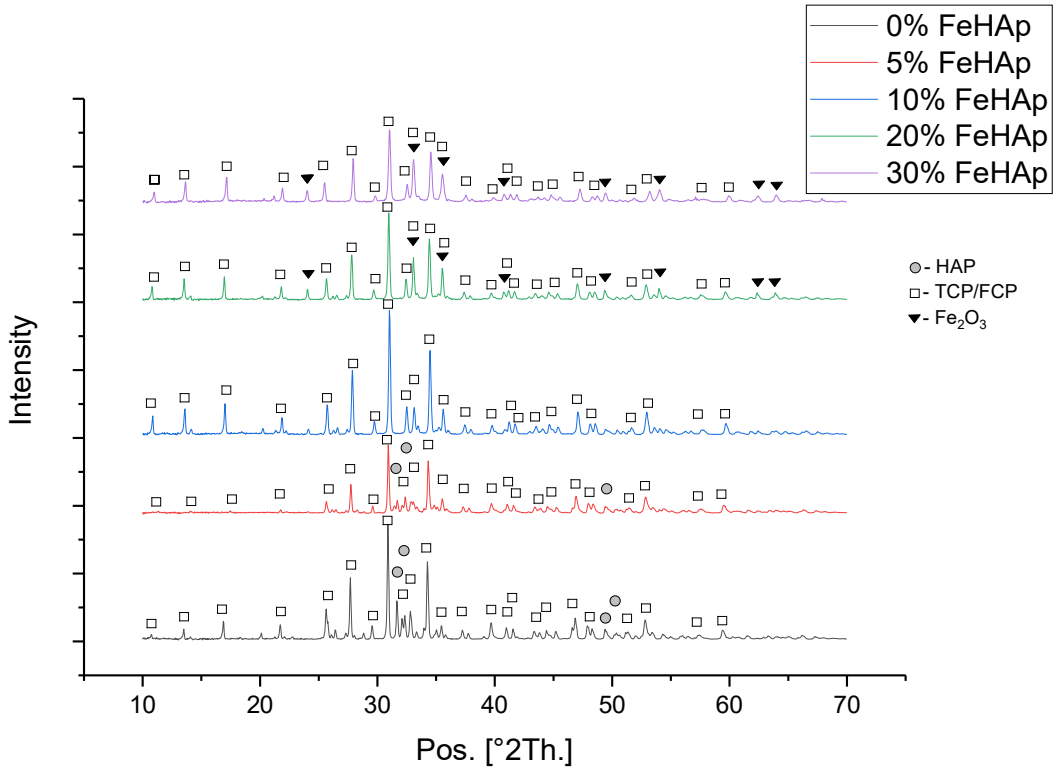

Figure 3.28: XRD Comparison of all post heated powders

At 10% FeHAp, strong, sharp crystalline peaks are apparent and the residual hydroxyapatite peaks have disappeared, making for an apparently isotropic FCP medium due to the iron concentration stoichiometry, and no hematite peaks are present. This is somewhat in contrast with the thermal analysis data, as there were no observed peaks of crystallisation or exothermic crystalline growth. The decomposition kinetics in this case creating a more uniform end product, in

shorter heating span, than the undoped material, due to a higher entropy with the stoichiometric precursor and by products.

20% and 30% FeHAp, the latter to a greater extent, demonstrate that even at moderate temperatures, saturation of the solid-solid solution has evidently caused diffusion of excess Iron and oxygen out of the heated material, phase separated and formed hematite. This has clearly disrupted some of the enthalpy for decomposition and has resulted in a reduced peak intensity with increasing doping concentration post 10at.% Fe^{3+}.

Whether the higher doping concentration and hematite formation will have any beneficial effect on the properties of the material post-laser processing is worth a subject of enquiry.

3.4 Substrate preparation

The synthesised powders and appropriate substrates were prepared in the following ways:

3.4.1 Pellets

After powder preparation, drying and milling, as outlined above; approximately 1g of each of the powders was placed into a 13mm diameter die press. A force of 1tonne, leading to an overall pressure of 75MPa was applied to the powder for 5 minutes. After which the resultant pellet was carefully ejected from the die and stored, and the die press washed and dried before the next sample, to prevent cross sample contamination.

3.4.2 Tooth substrates

Tooth samples were prepared by Dr. Simon Strafford from the University Of Leeds Dental School. Bovine incisors were cut into rectangular blocks and sterilised with γ-ray radiation. Each surface of the block was then polished using 2500 grade silicon carbide paper for 2 minutes. The tooth samples were then set in epoxy resin, and some of the blocks were also treated in order to obtain a groove in the centre of the sample. This was accomplished by applying nail varnish to the tooth surface at the limit of the intended groove, and a pH = 3.5, 1% citric acid solution was applied onto the un-varnished surface and left. After 12h, the acid had etched away approximately 1mm, and the nail varnish could then be removed with acetone.

3.4.3 Titanium substrates

Medical grade Titanium alloy, (Ti-6Al-4V; grade 5; ASTM B348-05), 30mm rod was purchased from goodfellow group. The rod was then sliced into multiple

3mm thick discs and wet polished on each surface, up to grade 1200 silicon carbide polish paper, before being cut down further into smaller 5mm wide strips. The strips were then cleaned polished again to remove any remnant material from the cutting process and dried.

3.4.4 Powder deposition onto the substrate surfaces

Evaporative deposition was one of the main techniques employed in the depositing the powders to the substrate surface: The powders were added to ethanol and mechanically agitated, often with an ultrasonic bath, if the facility was available. The mixture was then left for several seconds and a small volume was pipetted onto the substrate surface until there was adequate wetting and coating of the surface. The sample was then left to dry for a few minutes until all the ethanol had evaporated off, and a continuous layer on the substrate surface was formed.

4 Femtosecond laser ablation of Fe^{3+} doped calcium phosphates

Ultrafast laser matter interactions have garnered most of their attention due to their ability to induce non-linear effects in a medium, should high enough energy density conditions arise. Energy depositions in this regime are highly efficient, as even at relatively low pulse energies, high pulse peak powers can be generated and are capable of ionising a large number of electrons.

For the purposes of modifying or sintering of a material, then, it is apparent that an upper boundary exists in terms of energy density, in order to modify the irradiated material without subsequent removal via ablation.

This chapter is then intended to investigate the ablation threshold fluence for the described materials and substrates, and therefore determine this energy maxima for future sintering experiments.

The first section, 4.1, considers the laser systems used and how certain experimental parameters. Section 4.2, analyses the ablation of the produced materials. Section 4.3, analyses the ablation of the substrates, and finally, section 4.4 discusses the main findings.

4.1 Methods

Materials were prepared as described in subchapter 3.4

4.1.1 Laser system

The experiments were conducted using a Coherent Libra series Ti-sapphire femtosecond laser, with a pulse duration of 100fs, centre wavelength of 800nm, maximum repetition rate of 1kHz and maximum average power at 1W, yielding a maximum pulse energy of >1mJ. The laser energy was controlled with a half wave plate and beam splitting polariser, and was measured with a pyroelectric energy meter (PE50-DIF-C and energy meter, Ophir).

The laser beam was then directed through mirrors and an objective lens (Newport 5725-B-H, 0.3NA) onto an XYZ motion stage (3 stacked ABL1000 air bearing direct drive linear stages, with A3200 Npaq controller). The beam delivery was then controlled by single shot firing from the laser controller for N=1, 10 and for N>10 the laser was run at 1 kHz, with a Thorlabs SH05 optical shutter, by adjusting the open time in accordance to the repetition rate.

Differing spot sizes were then controlled by varying the sample surface in the beam prior to the focal spot, at a distance from the lens that was made easily with the accuracy of the motion stage.

4.1.2 Determination of spot size

The spot focal plane was determined by zeroing the lens edge with the motion stage platform. Starting at a fixed location from the lens edge, it is then possible to ablate lines into the surface of a material whilst changing the stage axis with respect to the lens.

This will create an ablation track that varies in thickness with respect to the distance from the focal plane of the lens and motion in the z-axis, as per Figure 4.1. With this discovered distance, traversed z-axis, and geometry, it is possible to deduce that the focal plane is exactly 7.5mm from the lens edge.

Figure 4.1: Ablation crater generated by rastering the material surface in the beam path with changing z-axis.

In a similar fashion, any other spot size may be generated by working prior to the focal plane and the lens edge. The fundamental minimum spot-size of the focal plane may be discovered using the lens parameters as outlined by the manufacturer, see Table 4.1, and the equation for a diffraction limited Gaussian beam with plane wave-front [188]:

$$d_{focus} = \frac{4}{\pi}\frac{\lambda f_{lens}}{A_{lens}} \qquad 4.1$$

Where d is the focus diameter, λ is the laser wavelength, f_{lens} is the effective focal length, and A_{lens} is the lens clear aperture. For the given parameters, the Gaussian waist size of this focus is 2.03μm.

Table 4.1: Lens parameters of the 5725-B-H

Lens Shape	Plano-Convex Aspheric
Lens Material	Corning C0550 Glass
Effective Focal Length	11.0 mm
Clear Aperture	5.5 mm
Numerical Aperture	0.3
Working Distance	8.0 mm

The beam may be represented as a flat ended cone, the major diameter being the input aperture of the lens, and the minor diameter being 2.03μm. A cross section of this cone at any stage, may simulate a variant spot size between these two values. Thus in order to obtain a spot diameter of 100μm, moving 0.25mm away from the focal plane, toward the lens, will represent a cross section of this cone with this diameter, to an accurate degree.

4.2 Ablation properties of Fe^{3+} doped calcium phosphates

Pressed pellets of the selected materials were placed onto the motion stage and the subsequent height of the lens edge was modified in order to secure a spot size of 100μm and the material surface, as per §4.1.2. The pellets were then irradiated with pulses of N = 1, 10, 100 and 1000, at energies ranging from 50-750uJ, at 50uJ increments. The ablation craters were then analysed via an optical microscope to measure the ablated regions parametric dimensions.

4.2.1 Crater morphology

Microscopy images of the ablated craters were taken utilising differential interference contrast, unless normal bright field imagery proved more visually clear. Various changes to the camera exposure, brightness or contrast, has been

applied during and in post processing, which accounts for the variations in images. All the images are for the 400uJ spot for each material and N number, which is the middle of the energy spectrum used.

It is apparent by observing Figure 4.2 to Figure 4.6 that there is little disparity between the samples. The N=1 images reveal a very shallow crater in the wake of just a single ablative shot, it appears as if just a few surface crystals have been removed in the process. As N increases, further boring of the hole is apparent, as one might expect, however this has little effect on the diameter of the holes, as all of the samples and N numbers are within 109±8μm, with this particular energy.

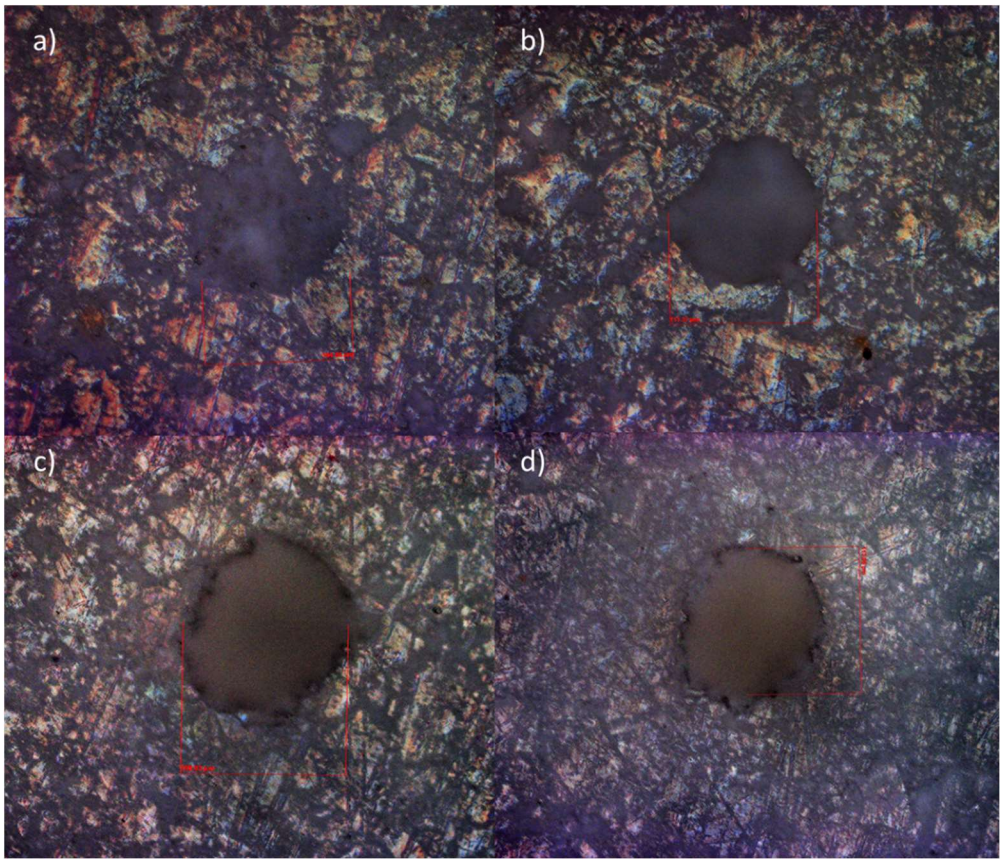

Figure 4.2: Ablation craters for 0% FeHAp for a) N=1, b) N=10, c) N=100 and d) N=1000

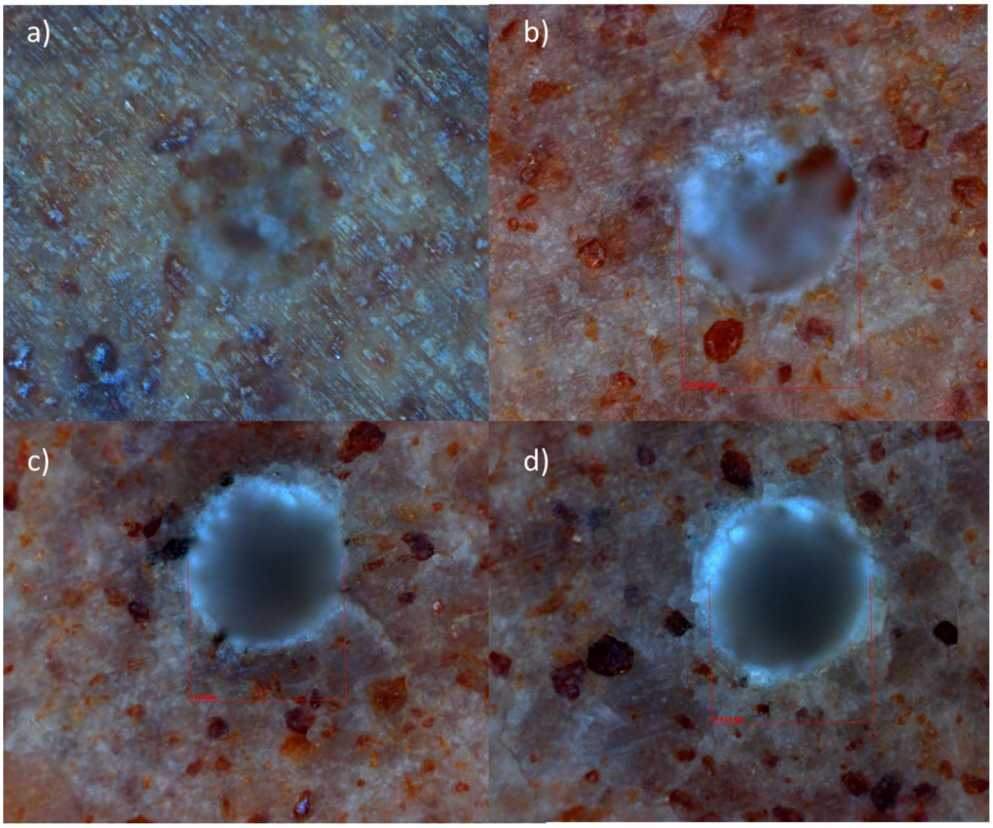

Figure 4.3: Ablation craters for 5% FeHAp for a) N=1, b) N=10, c) N=100 and d) N=1000

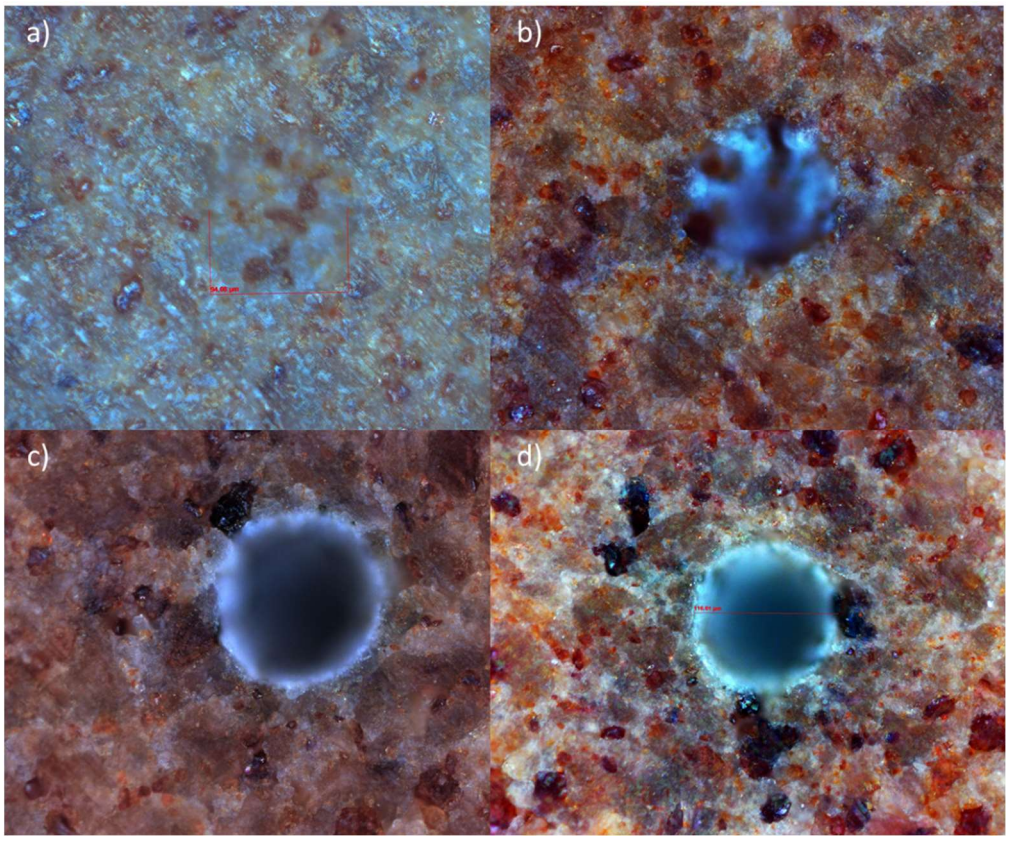

Figure 4.4: Ablation craters for 10% FeHAp for a) N=1, b) N=10, c) N=100 and d) N=1000

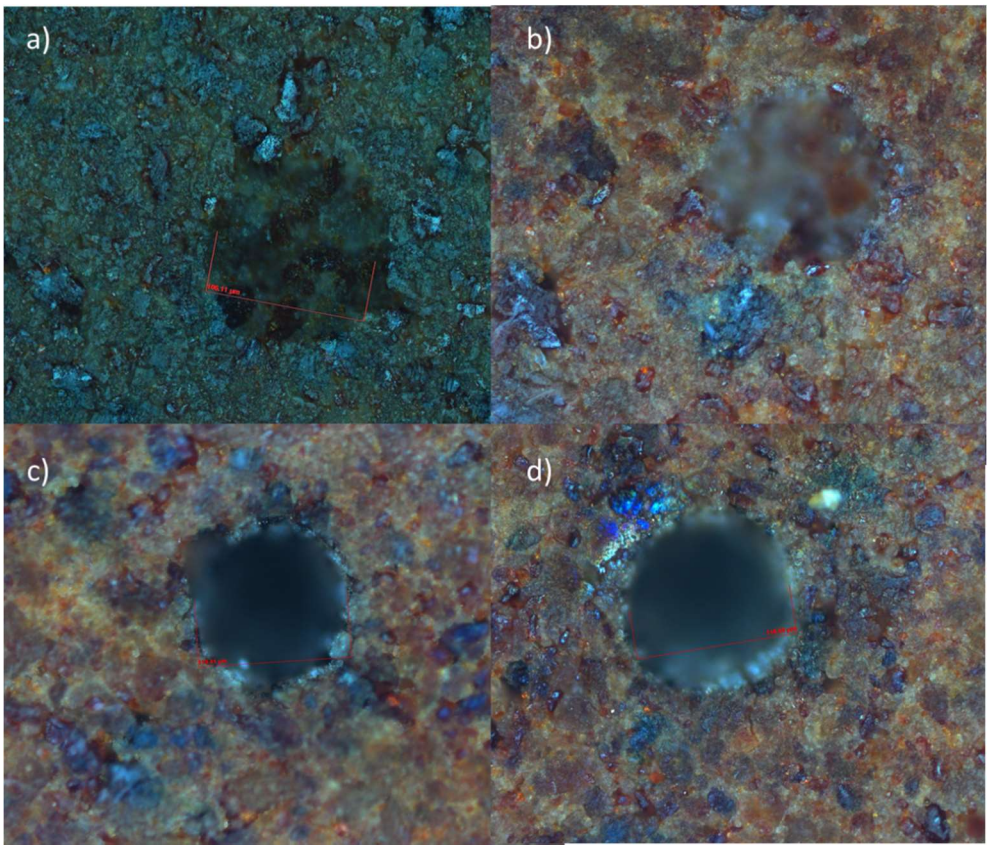

Figure 4.5: Ablation craters for 20% FeHAp for a) N=1, b) N=10, c) N=100 and d) N=1000

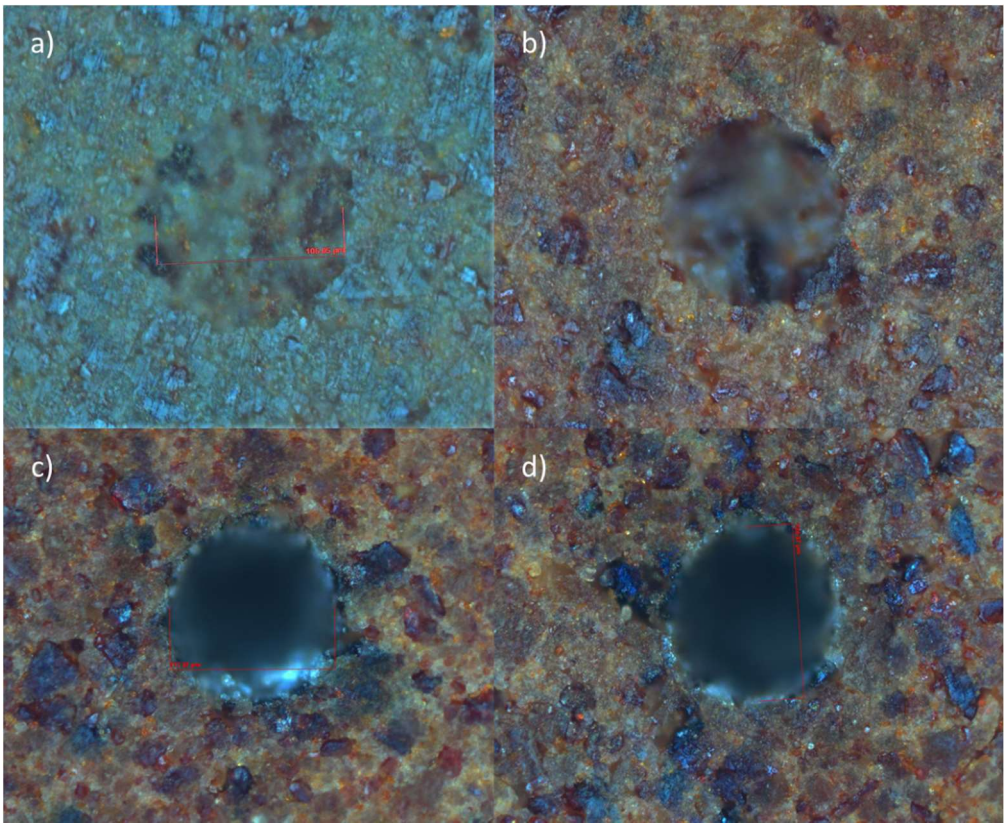

Figure 4.6: Ablation craters for 30% FeHAp for a) N=1, b) N=10, c) N=100 and d) N=1000

The features appear regularly circular across all the samples, except some edges appear relatively rough and more oval. This roughness of the crater edges is likely due to the removal of whole crystals post ablation that lie across the border of where the Gaussian energy profile tails off below the ablation threshold.

These features therefore made difficulty in accurately measuring the crater dimensions, which was done via a measuring tool in the microscope software by selecting a pixel range within the image, and done by eye. Measurement of several craters, several times over, revealed that there could be a discrepancy of up to ±5%. This should be taken into consideration during evaluation of the measurements.

4.2.2 Threshold fluence

Investigations of crater sizes generated by femtosecond pulsed laser ablation as a function of laser parameters, may be investigated with the scale law for diameter measurements. Liu et al. [189] determined that when a material interacts with a spatially Gaussian beam of radius w_0, the $1/e^2$ radial distribution of the laser fluence is:

$$F(r) = F_0 \exp\left(\frac{-2r^2}{w_0^2}\right) \qquad 4.2$$

Substituting for r = D/2 and obtaining the threshold fluence equivalence, $F_{0peak} = F_{th}$ and D = 0, we may be able to obtain the region of surface modification must follow the scaling:

$$D^2 = 2w_0^2 \ln\left(\frac{F}{F_{th}}\right) \qquad 4.3$$

Where D is the crater diameter, w_0 is the Gaussian waist radius (where energy has dropped to $1/e^2$ level) and F_{th} is the threshold fluence and F is the applied fluence. This may also be expressed in terms of energy and threshold energy, as these terms and fluence are proportional. The use of energy in this term may therefore be used to determine the surface spot size, and thus adjudicate fluence values accurately.

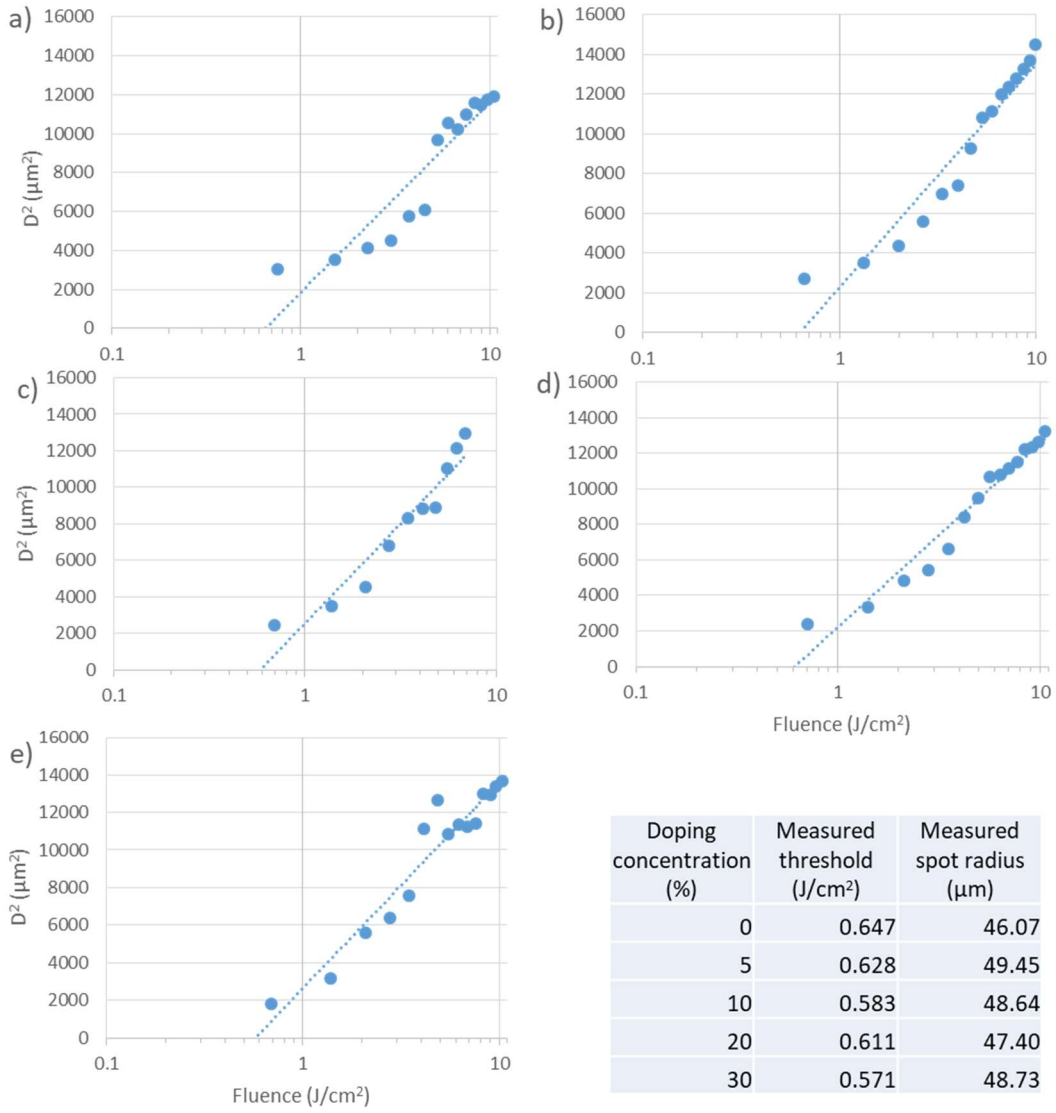

Doping concentration (%)	Measured threshold (J/cm²)	Measured spot radius (µm)
0	0.647	46.07
5	0.628	49.45
10	0.583	48.64
20	0.611	47.40
30	0.571	48.73

Figure 4.7: N= 1, D² vs fluence measurements over all energies for a) 0%, b) 5%, c) 10%, d) 20% and e) 30% Fe^{3+} doped hydroxyapatite

The single shot ablation threshold is the minimum average required fluence to initiate ablation with a single pulse. This has been determined by plotting the square of the crater diameter, D^2, for differing laser fluences and utilising the linear relationship of D^2 and ln(F) the varying parameters may be derived as per Equation 4.3, the slope of the trend line across measured values is then representative of the spot radius and the intercept at the abscissa is the threshold, $D^2 = 0$, fluence.

It can be seen in Figure 4.7 that there are some relatively anomalous results, particularly towards the lower end of the energy spectrum. This is likely due to the inherent measurement issues as previously discussed. However, the main perturbations in these data still hold an average coefficient of determination of around 0.92, and so the accuracy of these measurements should reflect this.

As such, for the given doping concentrations, as seen in the table inset in Figure 4.7, we can see that we obtain single shot ablation thresholds as 0.647±0.052, 0.628±0.050, 0.583±0.047, 0.611±0.049 and 0.571±0.046 J/cm^2 , for 0%, 5%, 10%, 20% and 30% Fe^{3+} doped hydroxyapatite respectively.

Despite this invariability, the measured spot radius, holds its value towards the intended spot diameter of 100μm, with a minima of 92.14μm and maxima of 98.9μm, across the samples, therefore regaining some confidence in the accuracy of the measurements, and the method of determining the spot dimensions at the surface.

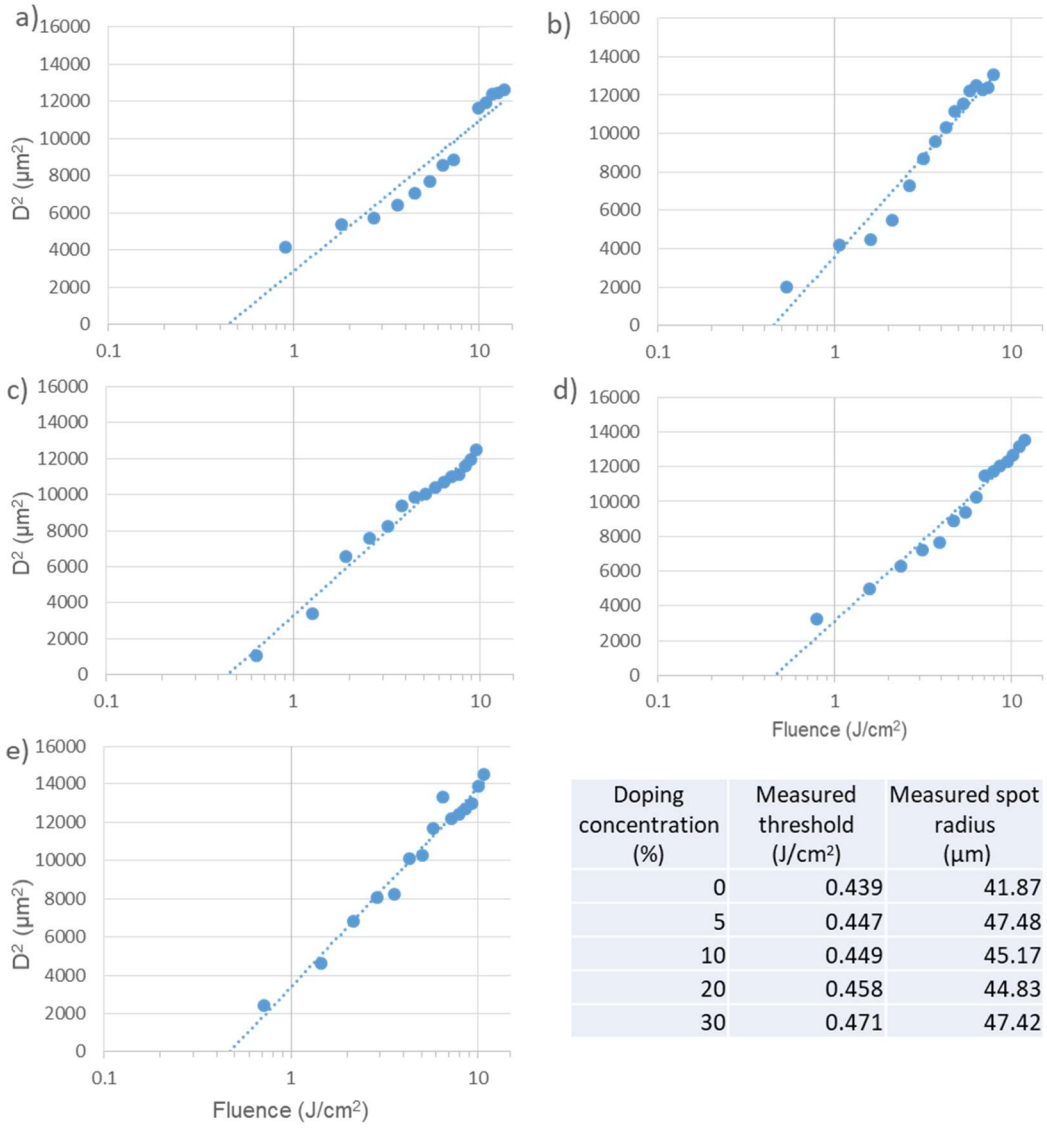

Doping concentration (%)	Measured threshold (J/cm²)	Measured spot radius (µm)
0	0.439	41.87
5	0.447	47.48
10	0.449	45.17
20	0.458	44.83
30	0.471	47.42

Figure 4.8: N= 10, D^2 vs fluence measurements over all energies for a) 0%, b) 5%, c) 10%, d) 20% and e) 30% Fe^{3+} doped hydroxyapatite

The ablation threshold of multi-shot experiments is expected to decrease, due to the train of pulses overlapping and the incubation effect [190]. This effect is attributed to the generation of surface defects, from pulses lower than the threshold of ablation, that cause absorption localities for the latter pulses, therefore lowering the required fluence. These defects may be the result of changes in the mechanical properties of the target material or chemical changes due to the sub-ablative pulse.

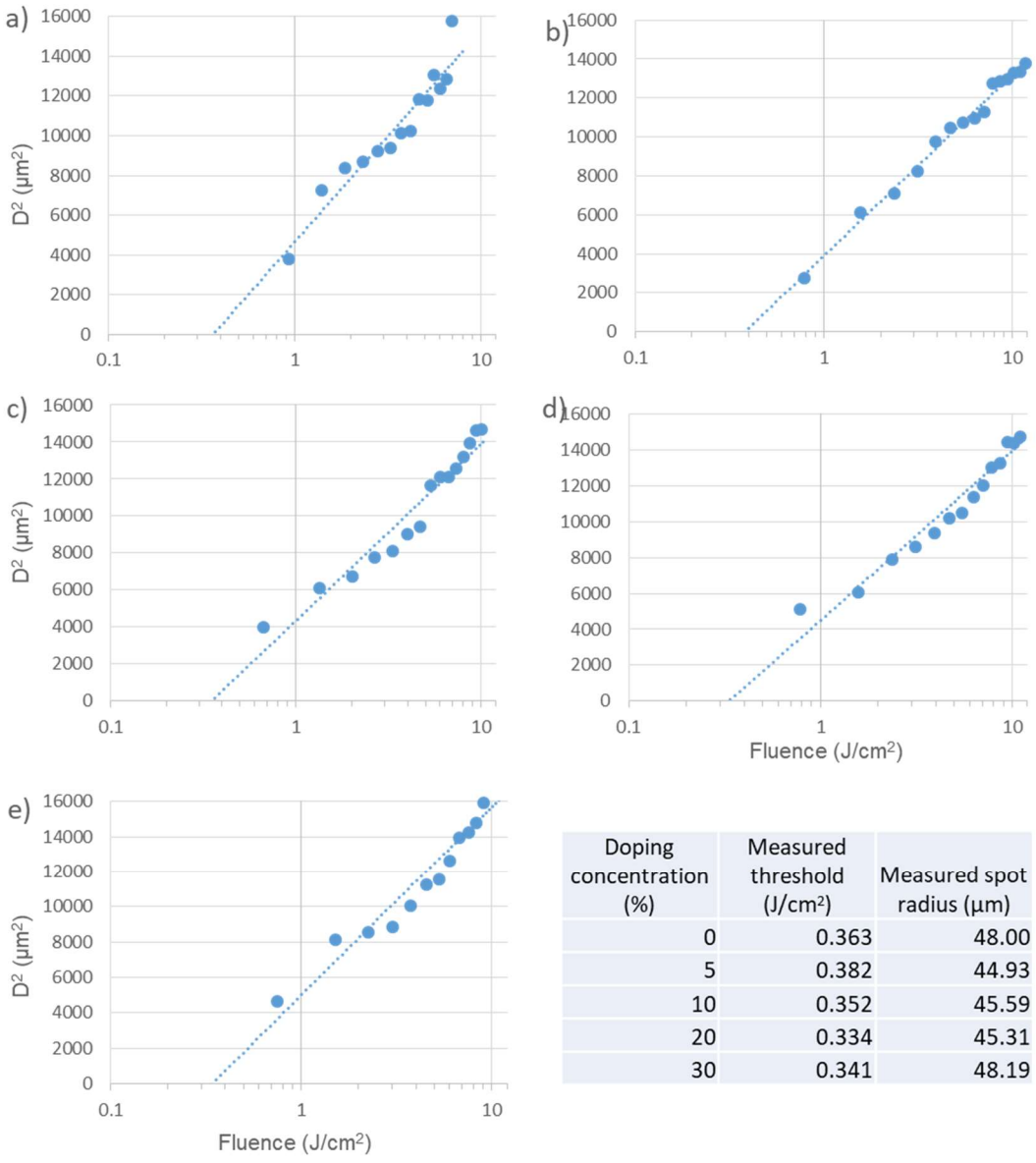

Doping concentration (%)	Measured threshold (J/cm²)	Measured spot radius (µm)
0	0.363	48.00
5	0.382	44.93
10	0.352	45.59
20	0.334	45.31
30	0.341	48.19

Figure 4.9: N= 100, D^2 vs fluence measurements over all energies for a) 0%, b) 5%, c) 10%, d) 20% and e) 30% Fe^{3+} doped hydroxyapatite

To take the multi-shot ablation threshold and incubation effect into account, crater diameters are determined in the usual way. It has been shown that equation 4.3 is also valid in the regime [191]. Although, accuracy of D^2 measurements in the multi-shot experiments has been shown to be diminished due to crack formation around craters. This is apparent in Figures 4.2-4.6, where N = 100 and 1000, where the crater edge is not particularly uniform or discrete.

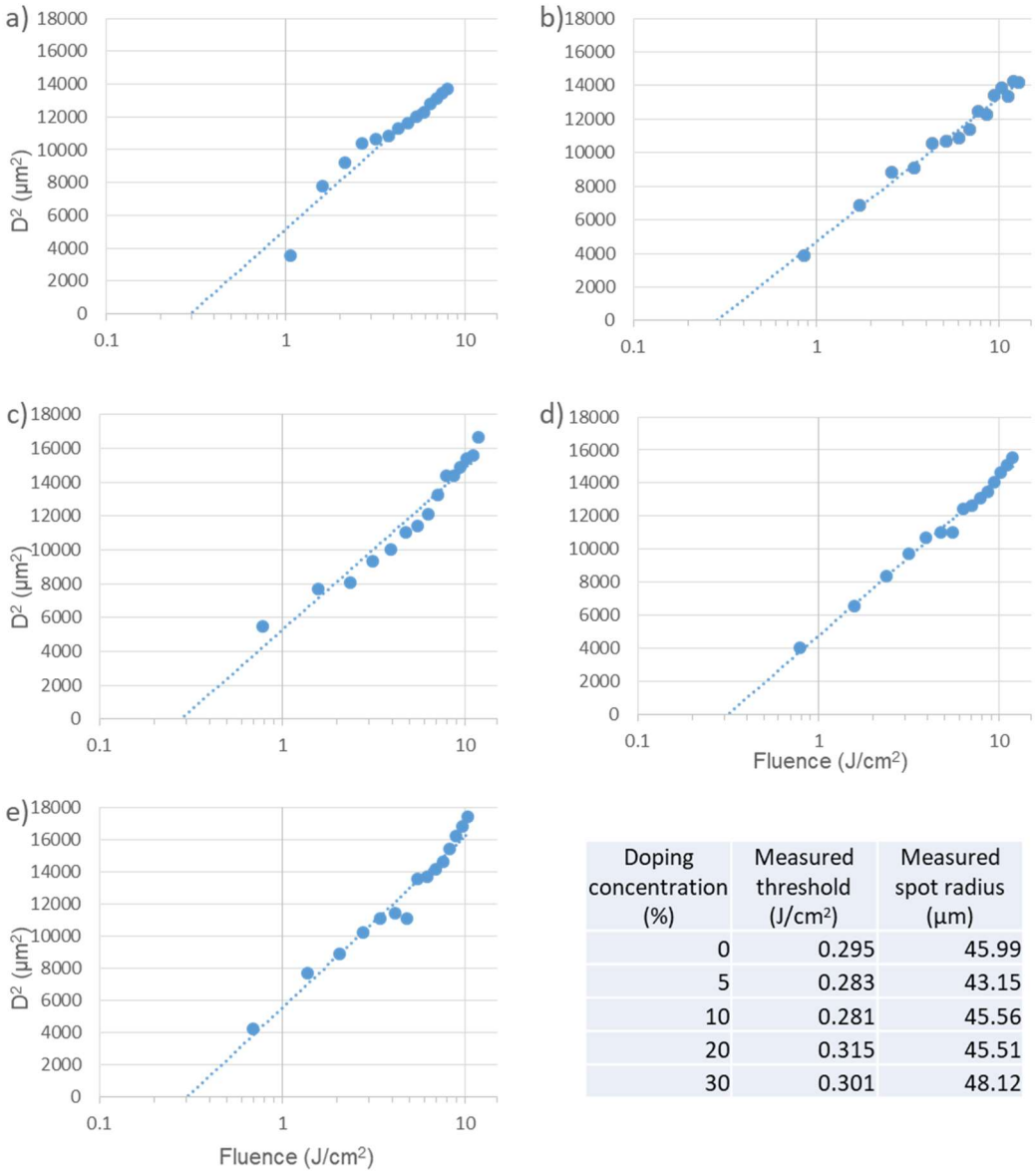

Doping concentration (%)	Measured threshold (J/cm²)	Measured spot radius (µm)
0	0.295	45.99
5	0.283	43.15
10	0.281	45.56
20	0.315	45.51
30	0.301	48.12

Figure 4.10: N= 1000, D^2 vs fluence measurements over all energies for a) 0%, b) 5%, c) 10%, d) 20% and e) 30% Fe^{3+} doped hydroxyapatite

It can be seen from Figure 4.8 to Figure 4.10, that there is a clear decrease in ablation threshold with increasing pulse number, in agreement with the literature. Although measurement of the spot radius has decreased slightly in comparison to the single shot experiments, it remains relatively consistent throughout the increasing pulse numbers, and its decrease therefore can be attributed to changes in the experimental conditions, such as lens height placement with respect to the sample surface.

4.2.3 Effect of Fe^{3+} concentration on the threshold values

Impurities are expected to generate lower ablation thresholds within a material due to the introduction of absorption sites and higher density of states surrounding the impurity in the crystal structure [192]. These impurities can also seed electrons in the laser interaction volume that can interact with the normal medium through collisions with other electrons and the lattice through dephasing [193].

To consider whether the Fe^{3+} substitution into the crystal structure of the lattice is an impurity, or whether it has full integration into the crystal system itself we can deliberate these ablation results. Since we know that the absorption centres in the crystals will be with the substituted ions, within the broad 3d; $^4T_{1g} \rightarrow {}^6A_{1g}$ transitions, we therefore might expect that there would be decreasing ablation threshold with increasing doping concentration.

Alternatively, since the Fe^{3+} is included into the crystal structure and with the given UV-vis results linear absorption across this band may be occurring, upon the onset of the pulse, we could also consider that mobilised electrons could jump through the various excitation transitions of the Fe^{3+} electronic structure to populate the UV band edge, without the need for multiphoton processes.

The results however are quite consistent and demonstrate parity across all samples and pulse numbers, Figure 4.11, Table 4.2. This suggests that the ablation threshold is dependent solely on multiphoton processes in exceeding the band gap of the material and populating the UV conduction band edge.

Table 4.2: overview of measured thresholds and spot radii for all Fe^{3+} doping concentrations and pulse numbers

Doping concentration (%)	Measured threshold (J/cm²)				Measured spot radius (µm)			
	N=1	N=10	N=100	N=1000	N=1	N=10	N=100	N=1000
0	0.647	0.439	0.363	0.295	46.065	41.869	47.998	45.989
5	0.628	0.447	0.382	0.283	49.447	47.482	44.933	43.151
10	0.583	0.449	0.352	0.281	48.636	45.172	45.585	45.558
20	0.611	0.458	0.334	0.315	47.397	44.827	45.310	45.514
30	0.571	0.471	0.341	0.301	48.734	47.424	48.192	48.120

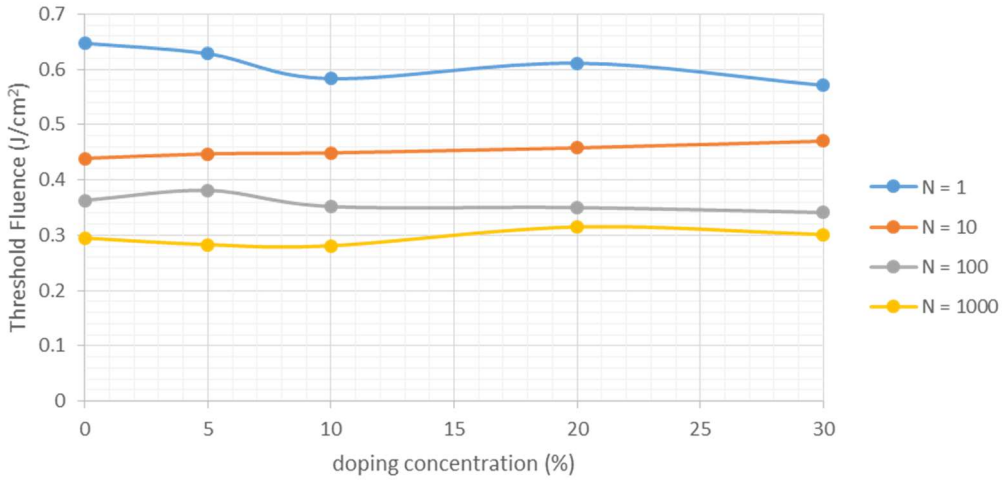

Figure 4.11: Trend in the measured ablation thresholds for all samples

4.2.3.1 Band gap of the materials

The Tauc analysis as per §3.3.6.2, is therefore confirmed to some extent, in that there must be a further absorption band in the materials lower than the measured 250nm, that is a similar band edge to the undoped hydroxyapatite ~6eV. This would therefore determine the ablation thresholds of the materials and since the multiphoton absorption in this region will be effectively the same, across all materials, in order to populate the UV band edge, we would therefore expect the ablation thresholds to maintain despite doping concentration, which has been demonstrated.

4.3 Ablation properties of the substrates

As well as the knowledge of the upper energy bounds for the materials it is also useful to know the limitations of the substrate used, for similar purposes. For this reason ablation thresholds were measured at N = 1 and 1000 pulses for the Ti-6Al-4V and enamel substrates. The substrates were prepared and used corresponding to §4.2, however, with a larger spot radius of 150µm, and in the case of the enamel substrate, the motion stage was used to raster the beam at 150µm/s to simulate irradiance of 1000 pulses as a shutter was not available during these experiments.

4.3.1 Crater morphology

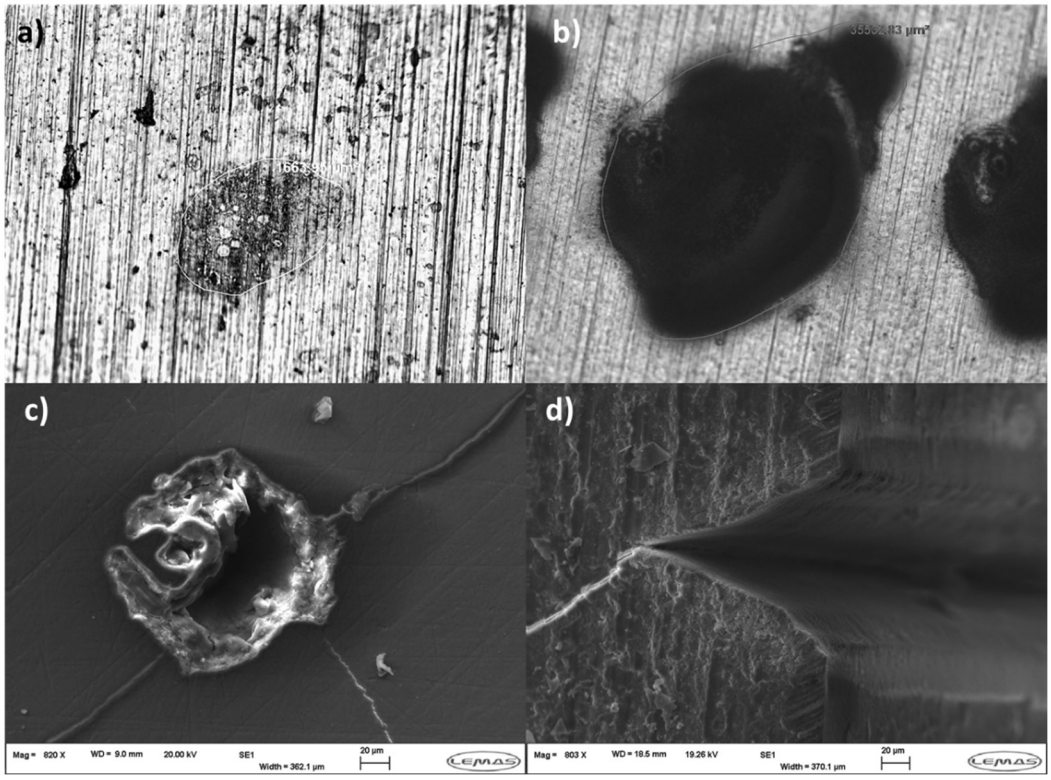

Figure 4.12: Crater morphology of the substrates for a) Ti-6Al-4V, N = 1, b) Ti-6Al-4V, N = 1000, c) Enamel, N=1 and d) enamel, N=1000

From the craters, Figure 4.12, it can be seen in a) and b) the ablation craters of the Ti-6Al-4V substrates for N = 1 and N = 1000 respectively. The initial crater for N = 1 is hardly noticeable, even with 100μJ, and resembles more a stain. This is likely due to the incredible small penetration depth into metals because of the abundance of conduction electrons. The staining that is observed is likely more akin to the defect generation, as discussed in §4.2.2. Figure 4.12(b) shows the crater from N = 1000 pulses, and shows a much darker area of interaction, where evidently the staining as seen in Figure 4.12(a) is exacerbated massively.

Figure 4.12(c & d) then show the single shot ablation and N = 1000 ablation cross section for the enamel substrate. At these relatively high energies of 250μJ, it is clear some cracking is formed in the enamel surface. This could be due to relief of internal stresses within the enamel layer prior to the ablation of the material surface, or a result of shock from the ablation due to the resultant impulse force from the escaping ablated plasma.

The removal depth in these samples appears greater than in the compressed powder pellets, probably due to the higher density, crystal size and compaction in the enamel compared to the compressed pellets. The single shot ablation Figure 4.12(c) does appear to have an island of remnant material towards the left of the crater, this was later discovered to be due to burn damage in the quarter-wave plate used to control the energy, hindering part of the beam in this region.

4.3.2 Threshold fluence

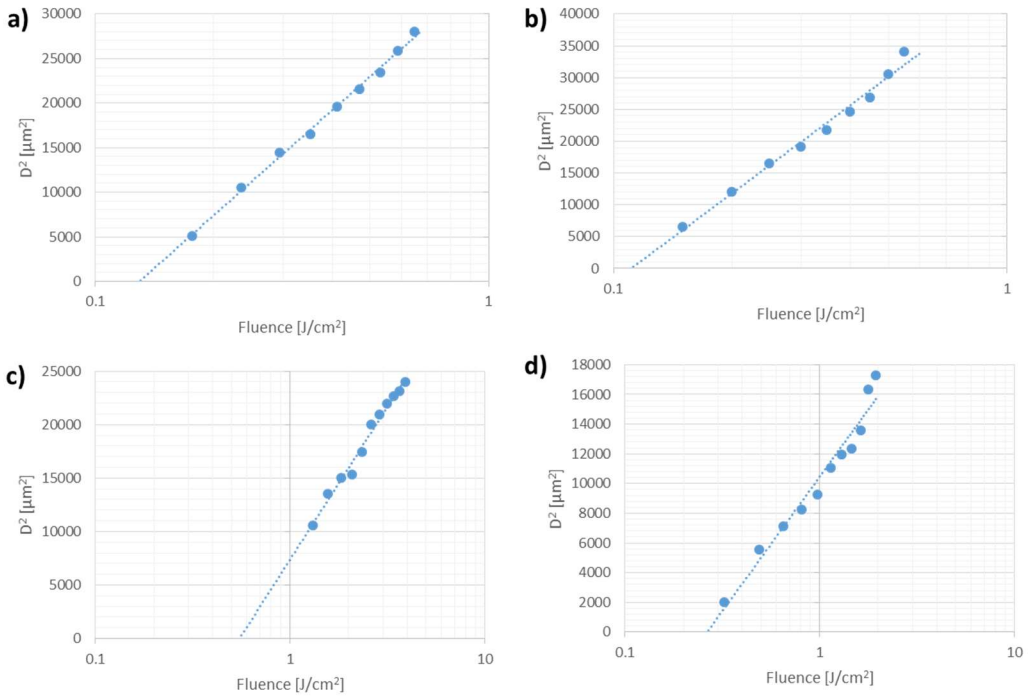

	Measured threshold (J/cm²)	Measured spot radius (µm)
Ti-4Al-6V (N = 1)	0.129	72.21
Ti-4Al-6V (N = 1000)	0.111	76.43
Enamel (N = 1)	0.551	78.64
Enamel (N = 1000)	0.265	69.67

Figure 4.13: D2 against fluence plots for a) Ti-6Al-4V, N = 1, b) Ti-6Al-4V, N = 1000, c) Enamel, N=1 and d) enamel, N=1000

The measured threshold fluences of the substrates, Figure 4.13, showed that the Ti-6Al-4V substrate had a much lower ablation threshold than the previous samples, 0.129 ± 0.01 J/cm² and 0.111 ± 0.01 J/cm² for N = 1 and N = 1000 pulses, respectively. These values are near the reported femtosecond laser ablation threshold of ~0.1 J/cm² for Ti-6Al-4V [194]. The multi-pulse, N = 1000, threshold has not deterred from the single shot ablation threshold all too radically. It is probably that the staining observed in the titanium is the formation of an oxide layer, after the pulse essentially superheats the surface. Electrons can move rapidly from the bulk to the surface of the material to populate the laser affected region almost instantaneously, allowing for reaction

kinetics to take place quickly after the pulse, and a passivation layer to form. However, each subsequent pulse will remove this layer and generate another, therefore limiting the effect of the incubation effect in these materials.

The ablation threshold of enamel, Figure 4.13, was shown to be 0.551 ± 0.044 J/cm^2 and 0.265 ± 0.021 J/cm^2 for N = 1 and N = 1000, respectively. Which is agreement with reports of 0.58 J/cm^2 for single pulse ablation of enamel by Ji et al. [195]. However, the 1000 pulse ablation threshold is slightly lower than the reported 0.3 J/cm^2 [196], however, Girard et al. [73] suggests that in cortical bone variance in the multi-pulse ablation is due to the interstitial organic materials between the hydroxyapatite crystals, and is therefore very sample dependent.

4.4 Conclusions

Laser ablation studies were conducted on the synthesised materials and substrates. It was found that the single shot ablation thresholds for the materials were 0.647±0.052 J/cm^2, 0.628±0.050 J/cm^2, 0.583±0.047 J/cm^2, 0.611±0.049 J/cm^2, and 0.571±0.046 J/cm^2, for 0%, 5%, 10%, 20% and 30% Fe^{3+} doped hydroxyapatite respectively. This demonstrated that there was no change in ablation threshold with increasing doping concentration, confirming that there is similar UV band edge across all samples.

Multiple pulse ablation thresholds decreased with increasing pulse number, showing that lower energy pulses can affect the material prior to the next pulse, allowing for lower threshold energies to ablate the material with the

consecutive pulse. This is in agreement with the literature for these types of materials, and therefore provides useful information for the upper energy bounds prior to ablation for future experimentation.

Ablation of the substrates showed similar results, the ablation threshold of Ti-6Al-4V was found to be 0.129 ± 0.01 J/cm^2, and enamel 0.551 ± 0.044 J/cm^2, which is in conjunction with reported values for these materials. The relatively low value of the Ti-6Al-4V ablation threshold may cause issues in later experimentation, due to the quite large disparity between the synthesised materials and substrate threshold values.

5 Low repetition rate regime femtosecond laser modification of Fe^{3+} doped calcium phosphates.

With the given results from the previous chapter 4, it is apparent that there are upper boundary energy limits to the use of femtosecond lasers for the means of sintering or modifying the material, without exemplifying the effects of ablation. However, Chikov et al, Symeitz et al and Ben-Yakar et al. [83], [94], [123] have also demonstrated modification of materials post ablation of the surface, which may also provide some utility in the aims of this study.

In this chapter, then, the objectives of the given experiments are to observe the efficacy of 1 kHz repetition rate femtosecond laser pulses on the materials and substrates for sintering of the materials thereof. And also attempt high pulse energy depositions in order to observe effects of the materials under moderate fluence, aside from ablation.

The first section, 5.1, considers the laser systems used and certain experimental parameters. Section 5.2, analyses the sub-ablation of the produced materials. Section 5.3, analyses the sub-ablation of the substrates, and finally, section 5.4 discusses the main findings.

5.1 Methods

Materials were prepared and described as per chapter 3.4, however, for majority of these experiments, only the 10% Fe^{3+} doped material was used, as further investigations were halted due to closure of the laboratories for renovation and maintenance.

The experiments were conducted using a Coherent Libra series Ti-sapphire femtosecond laser, with a pulse duration of 100fs, centre wavelength of 800nm, maximum repetition rate of 1kHz and maximum average power at 1W, yielding a maximum pulse energy of >1mJ. The laser energy was controlled with a half wave plate and beam splitting polariser, and was measured with a pyroelectric energy meter (PE50-DIF-C and energy meter, Ophir).

The laser beam was then directed through mirrors and an objective lens (Newport 5725-B-H, 0.3NA) onto an XYZ motion stage (3 stacked ABL1000 air bearing direct drive linear stages, with A3200 Npaq controller).

The spot size was then controlled by varying the sample surface in the beam prior to the focal spot, at a distance from the lens that was made easily with the accuracy of the motion stage, as outlined in §4.1.1. The number of pulses then delivered to the surface per unit area was controlled by adjusting the scan speed of the motion stage in relation to the given spot size, allowing for a known number of pulses per unit area of the material.

5.2 Sub-ablation threshold processing experiments

In order to modify the materials appropriately, it would be necessary to deposit a relative amount of energy to the surface to generate either structural change to the material itself, via solid state sintering and crystal growth. Or the induction of melting and liquid phase sintering. This would be achieved through long depositions of the laser onto the surface, in order to obtain the greatest energy accumulation.

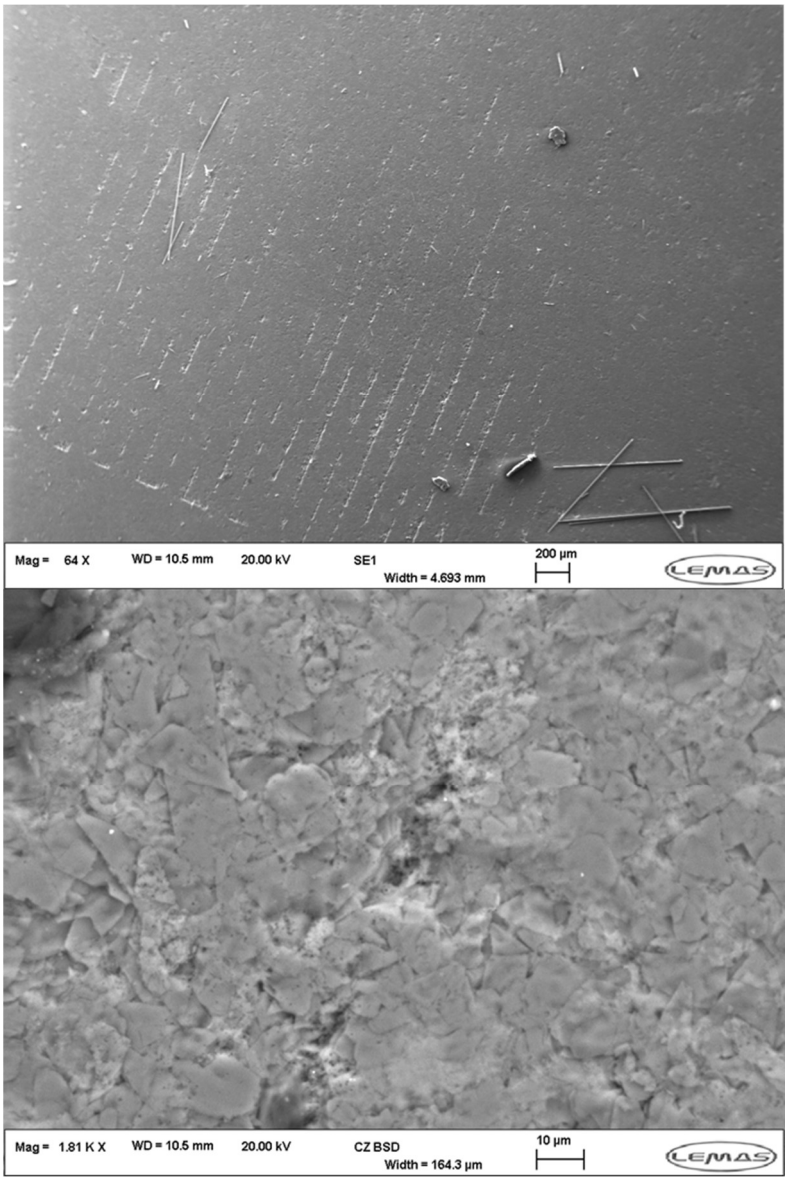

Figure 5.1: SEM Images of processed un-doped hydroxyapatite at 1 kHz, 0.3 J/cm², 5000 pulses per spot area.

Pellets were placed onto the motion stage and a spot size of 200μm, was arranged at the surface. Given the multi-shot ablation threshold of un-doped hydroxyapatite was 0.295±0.06 J/cm^2, a fluence of 0.3 J/cm^2 was applied to the surface, to utilise the maximum energy without inducing excessive ablation, which equated to 100μJ, as measured after losses, per pulse. The motion stage was then rastered at a speed of 40μm/s, as to deposit 5000 pulses per unit area.

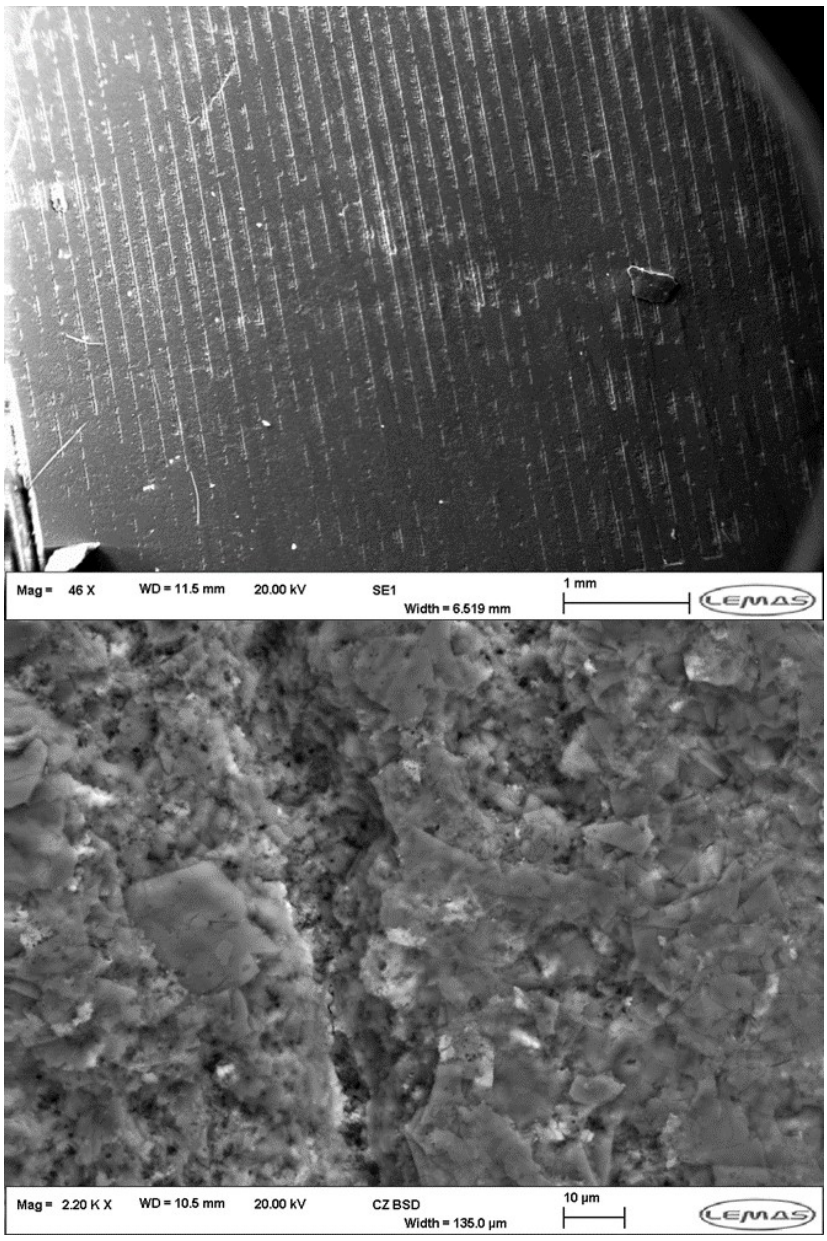

Figure 5.2: SEM Images of processed 10% Fe^{3+} doped hydroxyapatite at 1 kHz, 0.3 J/cm^2, 5000 pulses per spot area

As can be seen in Figure 5.1 and 5.2, mild ablation can be seen throughout the samples, generating lines in the raster direction over the sample. This is to be expected, working so close to the ablation threshold. However, little energy should have been lost into the ablative process at this energy regime as only a small portion of the beam energy is over threshold. This can be observed as despite using a 200μm spot, only ~10μm or so features are ablated in the laser path. The rest of the energy in the pulse will have interacted with the medium and not been lost into the ablative process.

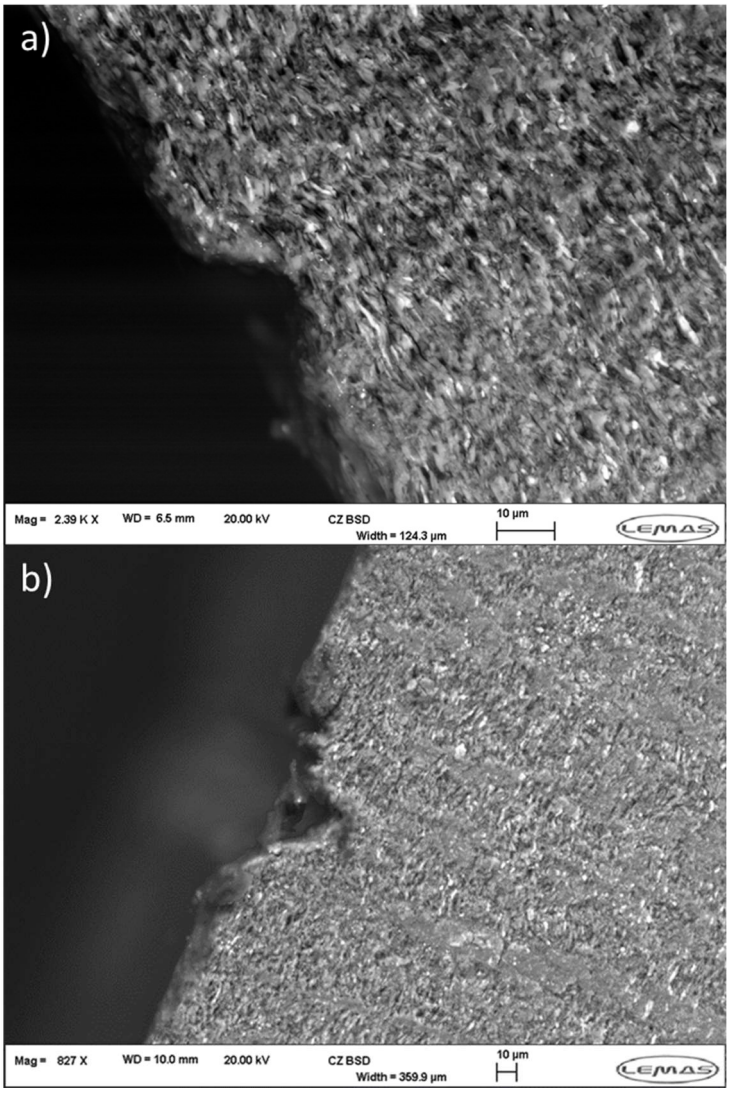

Figure 5.3: Cross-sectional SEM of a) un-doped hydroxyapatite and b) 10% Fe^{3+} doped hydroxyapatite

Cross sectional SEM of the ablated lines and surrounding material, as seen in Fig. 5.3 (a & b), shows that there is little difference in the morphology of the layered crystals from the bulk, around the ablation crater, or either side of the ablation crater, in both un-doped and doped samples. Therefore indicating that there has been little interaction with the material and the laser in these regimes apart from ablation.

X-Ray diffraction of these surfaces, as per outlined in §3.3.1, was then taken to see if any changes in the structure has taken place. And as it can be seen in Figure 5.4 and 5.5. There is very little change to the XRD spectra, with the exception of count rates being slightly higher in the unprocessed examples. Although this is relatively arbitrary, this could also be due shadowing of the incoming X-ray beams further than usual owing to the roughened surface, and less coherent material to be scanned due to the ablation craters.

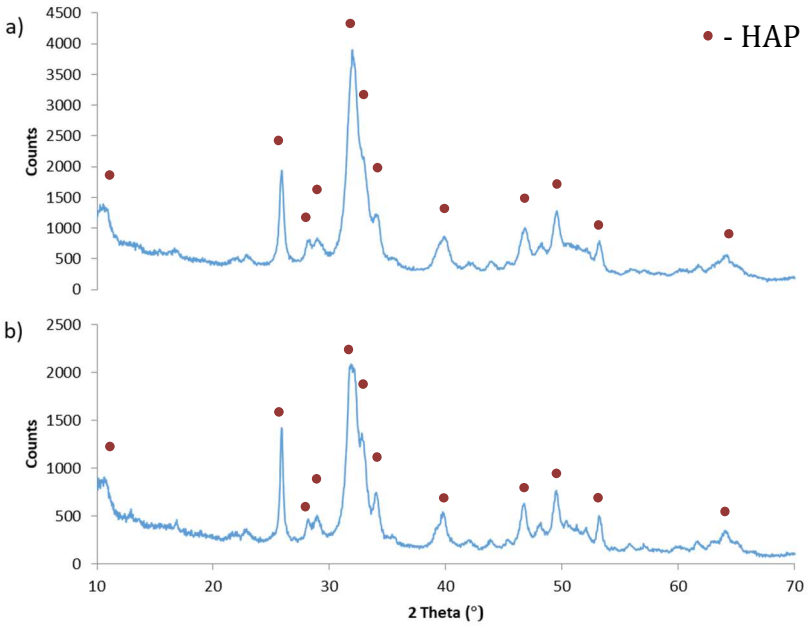

Figure 5.4: XRD spectra of a) unprocessed and b) processed un-doped hydroxyapatite

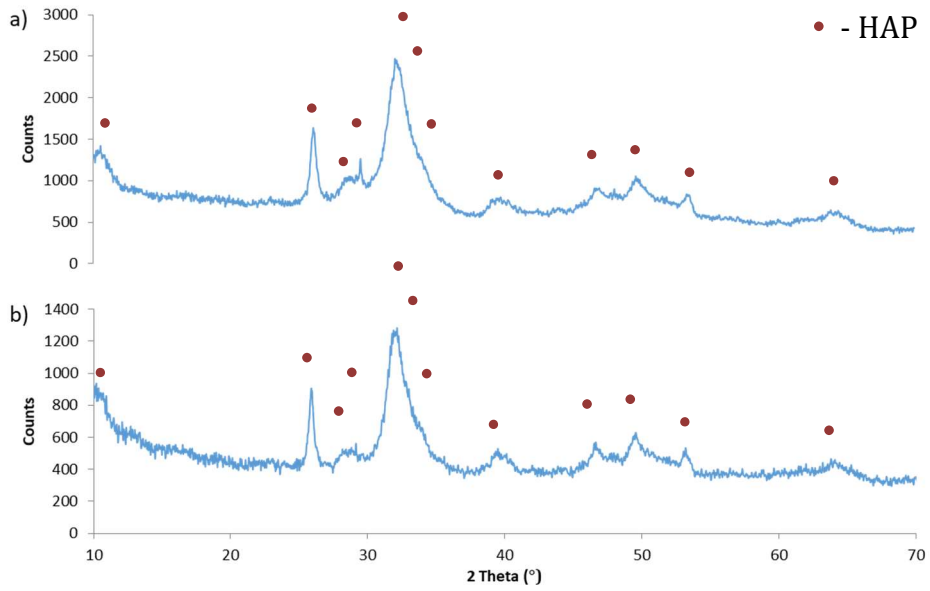

Figure 5.5: XRD spectra of a) unprocessed and b) processed 10% Fe^{3+}doped hydroxyapatite

5.2.1 Extreme energy processing interactions

Another assumption was that under high intensities, removal of the ablated material might cause enough reactionary forces onto the material surface to create a similar effect as per Ben-Yakar et al. [123].

If an ablation volume of material, roughly conical in shape had a depth of 200µm and a radius of 100µm then its volume would be 2.09 x 10^{-16} m^3, with an effective density of 3156 kg/m^3 [56], this would mean that its mass is 6.51 x 10^{-13} kg. The average ablation velocity for an ion in a etch area of this size is 500 m/s [191]. This can be then equated into a momentum change that must be effected onto the surface of the non-ablated area in the laser affected region. The momentum change occurring is then $\Delta p = mv$, with the mass and average velocity profile of above is: 3.26 x 10^{-10} kg m s^{-1}. Since ablation occurs at the order of nanoseconds, the resultant force onto the surface of the ejected cone will be 0.326N or 4.64 x 10^6 Pa. This is approximately four atmospheres, but we could expect that if the area underneath the ablation volume had been

stimulated throughout the laser pulse, due to any interactions with the laser effected material prior to coulomb explosion, and on the onset of ablation might require less energy to instil modification than the required amount as per §3.3.8, akin to restructuring type lattice disordering as per Sundaram et al. [119].

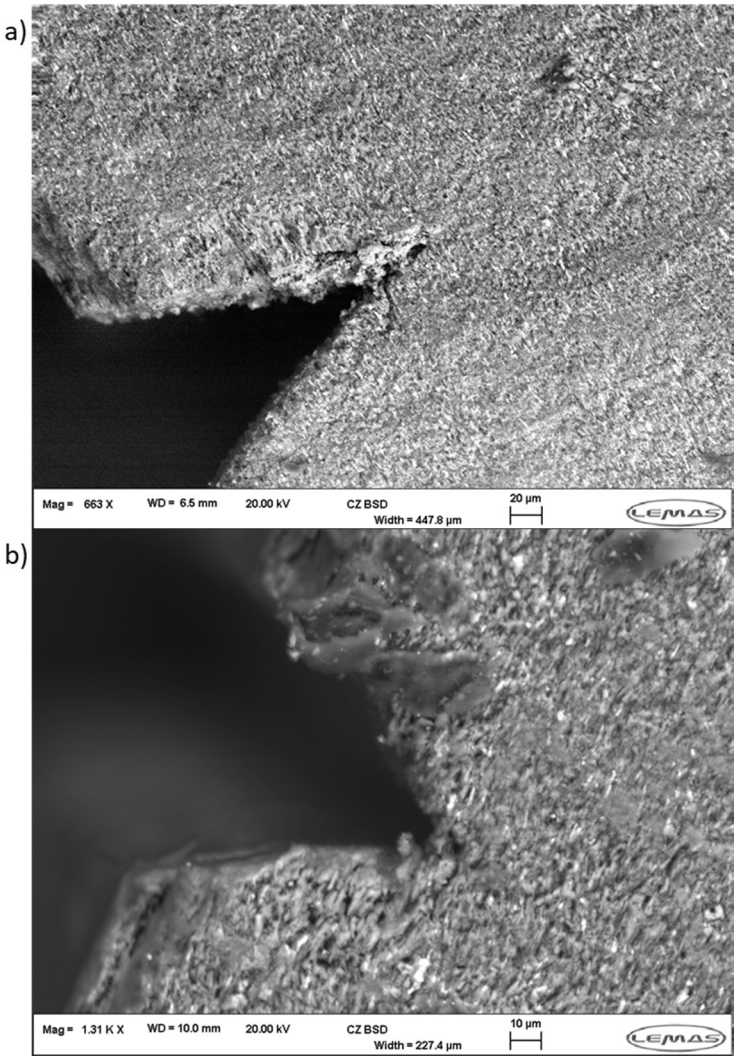

Figure 5.6: Extreme energy processing interactions of a) undoped and b) 10% Fe^{3+}doped hydroxyapatite

The cross sections of 0% FeHAp and 10% FeHAp post processing at 6.4 J/cm^2 with N = 2500 pulses per unit area can be seen in Figure 5.6 showed little interaction other than a clean ablation crater. The darker shade particulates surrounding the crater edge in Figure 5.6(b) are remnants of the cleaving

process in order to obtain the cross section. There is no apparent change in the particulate morphology in this regime, the order of multiphoton processes towards ablation are visibly too intense for any immediate structural disordering.

5.3 Coated substrate experiments

Despite the lack of observable interaction of the given materials with this particular laser regime, it seemed pertinent to attempt to learn what might occur should these materials be deposited onto a substrate, and are processed with a laser. Particularly for the case of Titanium alloy, where the ablation threshold is much lower than that of the synthesised materials and where a metallic substrate may well play a differing role in comparison to a dental substrate, which is essentially made from the same material.

5.3.1 Dental substrates

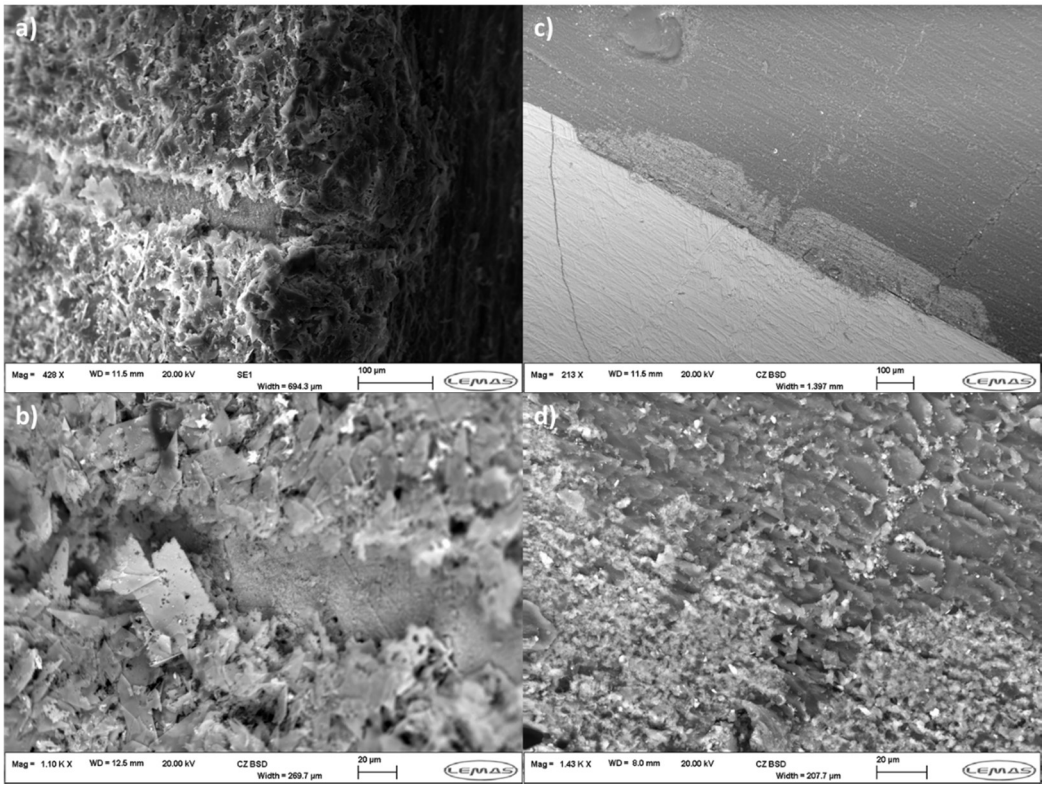

Figure 5.7: Processing of drop coated enamel substrates with 1kHz, 0.3 J/cm², N = 1000. a,b) 0% FeHAp and c, d) 10% FeHAp cross sections.

Enamel substrates were prepared as per §3.4 and processed with a 100µm beam diameter and 25µJ pulse, giving a fluence of 0.3 J/cm², the beam was then rastered at 0.1mm/s over the surface to deliver 1000 pulses to the coated substrate.

As can be seen in Figure 5.7, the laser has created an ablation path in the coating, for both materials. This is what might be expected, however, the coating has seemed to act as a passivation layer and protected the substrate from any ablation itself. Although at these lower fluences, the enamel surface may hold some resilience, if this particular substrate was devoid of any interstitial organic material between the hydroxyapatite crystals.

5.3.2 Ti-6Al-4V substrates

Symeitz et al. [83], proposed using a femtosecond laser, to stimulate the underlying metallic substrate with a calcium phosphate coating, utilising the disparity of the ablation thresholds between the two media and generate adequate bonding between the coating and the substrate. Paitel et al. [84], [85], also showed similarly with different laser sources. These experiments are therefore intended to simulate these results.

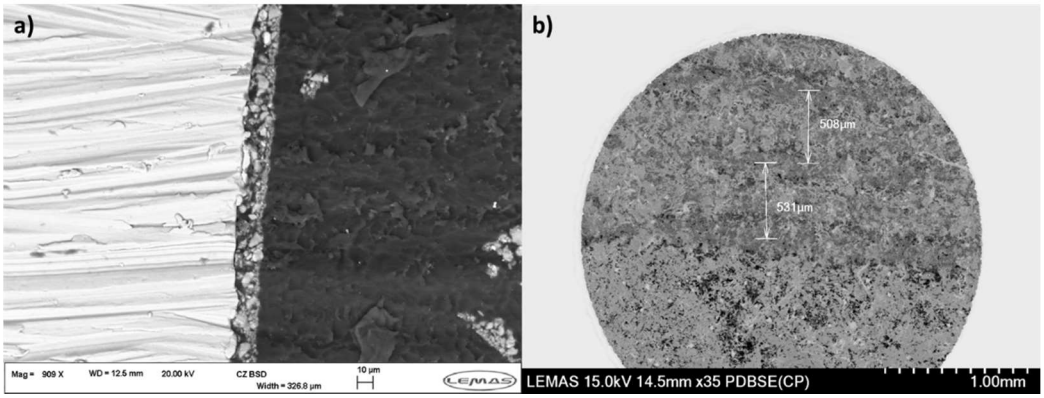

Figure 5.8: a) cross section of the coated Ti-6Al-4V substrate, b) laser path over the coated substrate.

Firstly, it should be noted that in order for the laser to interact with the underlying substrate, the thickness of the coating should be nominal. Figure 5.8(a) shows a cross section of the coating of 10% FeHAp onto the Ti-6Al-4V, to be approximately 10µm in thickness. This coating was then processed with a 100µm diameter beam spot and rastered at a rate of 0.1mm/s, with an energy of 18uJ to give and energy density of 0.22 J/cm^2, slightly above the ablation threshold of the substrate. The upper part of the image, Figure 5.8(b), shows the track lines made with these parameters onto 0% FeHAp, the lower part of the image showing unprocessed coating.

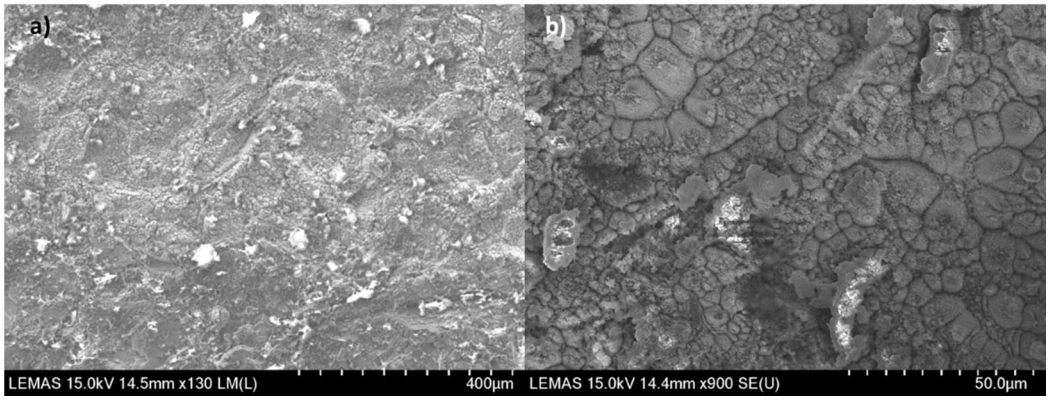

Figure 5.9: SEM images of the processed region of the substrate

Further SEM images of the laser track path, showed that there was little apparent coating remaining and the surface was quite heavily disrupted and patterned, Figure 5.9. However, upon further inspection, there did appear to be some crystallites bonded to the disrupted titanium substrate, Figure 5.10. EDX mapping of this area revealed that there were high constituent parts of calcium, phosphorus and oxygen on the surface of the substrate. We have therefore demonstrated with some efficacy the results reported by Symeitz et al. [83]

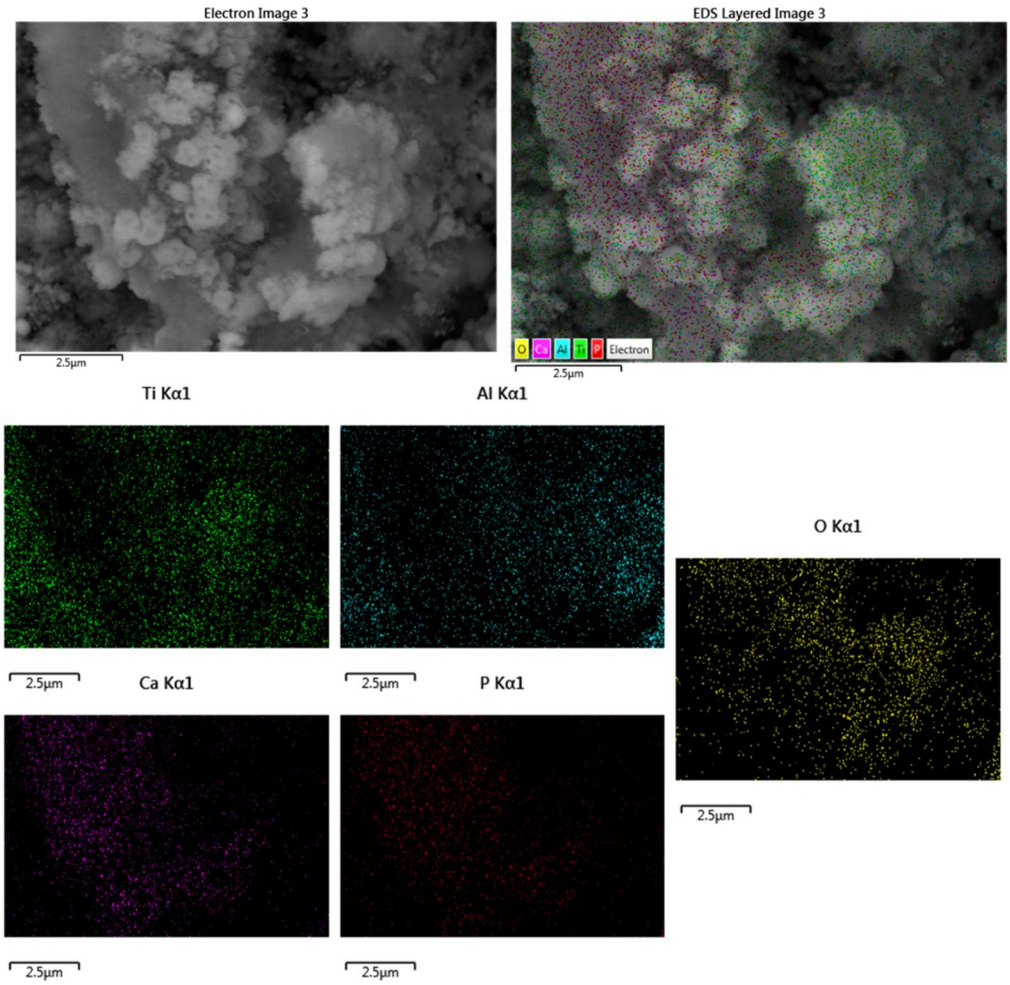

Figure 5.10: SEM and EDX mapping of the processed coated substrate

A Ti-6Al-4V substrate was then coated with 10% Fe^{3+} doped hydroxyapatite and the same procedure run again. After processing, the substrate was coated again, and then processed another two times, in order to try and obtain more material bonded to the substrate. SEM and EDX mapping was performed, and as can be seen in Figure 5.11, a much less disrupted surface is apparent. EDX mapping showed a fairly homogenous spread of calcium, phosphorus, oxygen and iron. Indicating a successful coating of the substrate in the processed parts, however the coating thickness available with this method is obviously dependent on the laser being able to transmit through the coating and interact with the

underlying substrate. Therefore limiting the use of this approach should coatings greater than a few microns be required.

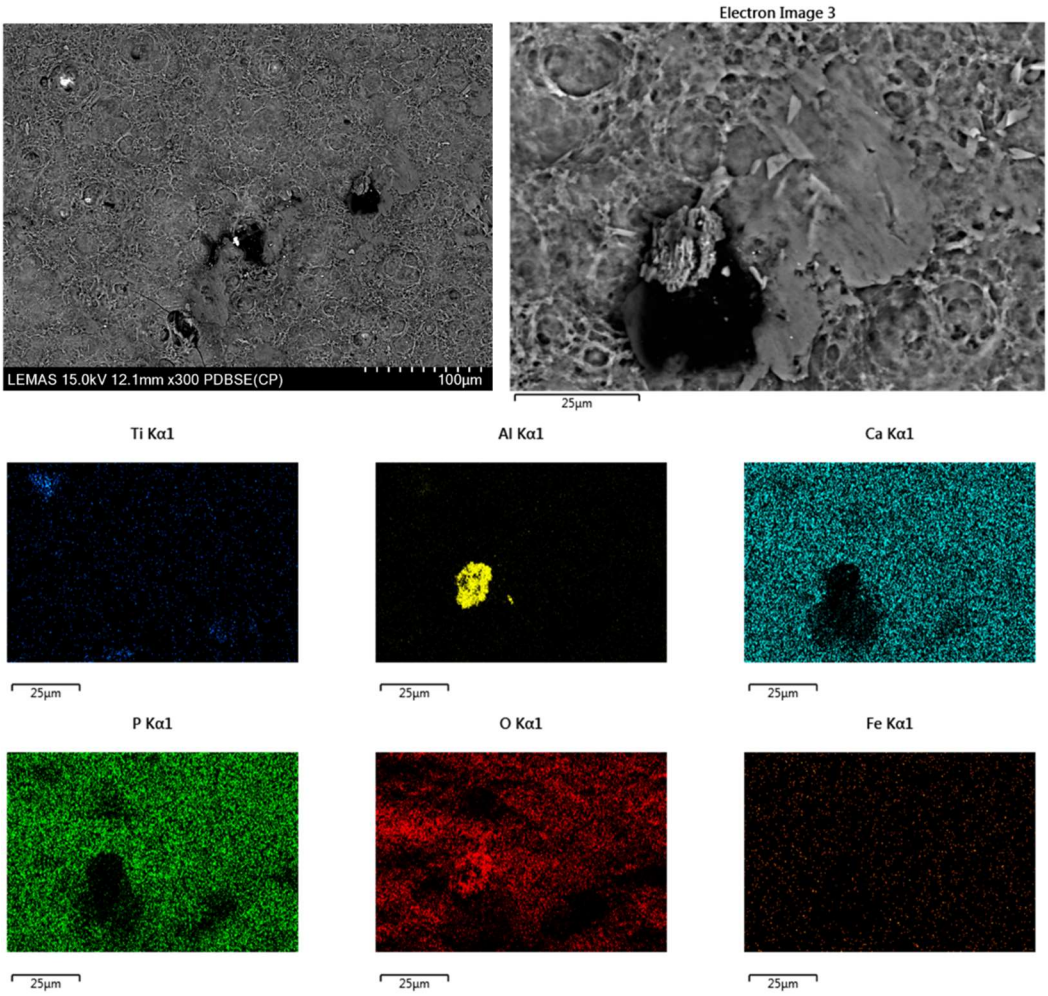

Figure 5.11: SEM and EDX mapping of the 10% FeHAp coated processed substrate,

5.4 Conclusions

Processing of 0% and 10% Fe^{3+} doped hydroxyapatite with 1kHz laser proved to be unsuccessful at generating any material change except ablation. This is likely due to the high reflectivity in the 0% FeHAp case, disallowing any energy to be absorbed. For the 10% FeHAp case, any linearly absorbed energy is likely dissipated before the next pulse in the pulse train.

High energy, high pulse number processing only proved to yield clean ablation of the materials. This was not synonymous to the experiments conducted by Chickov et al, in metals and semiconductors, expectedly due to the much higher band gaps within these materials requiring higher order photon processes.

Attempts onto the substrates showed that on a coated enamel surface, the material is solely ablated away despite the low processing conditions, expectedly. However, following reports from Symeitz et al. and Paitel et al, we have further demonstrated adhesion of calcium phosphates onto the surface of a titanium substrate. The efficacy of this technique appears valid and may improve the osseointegration of the titanium part coated in this manner. Further processing iterations in this way can lead to further coating of the substrate, although this will be limited in thickness due to the absorption of the laser energy by the coating layer.

6 Moderate repetition rate femtosecond laser interactions with Calcium Phosphates.

Considering there was an absence of modification outside ablation of the material with the 1 kHz system, mostly due to a lack linear absorption and heat accumulation, it becomes natural to increase the repetition rate in order to obtain faster depositions for accumulating energy and driving modification within the material surface.

In this chapter, then, the objectives of the given experiments are to observe the efficacy of 500 kHz repetition rate femtosecond laser pulses on the materials and substrates for modifying the materials thereof.

The first section, 6.1, considers the laser systems used and certain experimental parameters. Section 6.2, investigates the threshold modification energy for use of these materials and demonstrates sub-ablation threshold energy processing of the pellets and what material changes occur, and finally, section 6.3 discusses the main findings

6.1 Methods

Materials were prepared as per §3.4.

6.1.1 Laser system

The laser system was located at a project partner facility, LaserINN, in Italy, and utilising the system and laboratory was accomplished with the aid of Cesare Bonsario and Dr. Aurora Losecco.

The experiments were conducted using a Light Conversion, Pharos solid state Ytterbium laser which had a 290fs pulse duration, centre wavelength of 1028nm ± 5 nm, maximum repetition rate of 500 kHz, maximum average power of 10W and maximum pulse energy of 0.2 mJ. The laser energy was controlled with an inbuilt attenuator and was measured with a pyroelectric energy meter.

The laser beam was then directed through a 2x objective lens and onto a motion stage set up on an optical bench. The motion stage was a 5-axis motion stage with vacuum bed to secure the sample and was controlled via specialist programmable software.

The spot size at the surface of the samples in these experiments was verified by working in a region prior to the lens focus, similarly to §4.1.2. The focus of the lens focus being determined with a fairly high accuracy through a camera viewing port on the rear side of the focusing lens. By observing the surface of the sample through the lens visually, and bringing it into focus by eye, there is an accuracy in the focal plane that is related to the depth of field of the lens. Since visible light is shorter in wavelength the NIR source, the depth of field and

therefore Rayleigh length of the laser focus would be within the bounds of the laser depth of field and Rayleigh length.

6.2 Processing of materials

6.2.1 Investigation of the energy minima

Attempts were made at trying to establish the onset of material change by altering the power and speed of the laser. However, there were a few difficulties in trying to obtain exact values due to sporadic results, laser fluences and number of pulses seemed to have little correlation across the samples.

As can be seen by the microscopy images in Figure 6.1, the laser modified material has become much darker, almost black, a colour that was not realised through conventional heating. This meant that as the test was occurring there is a change in the optical properties of the material. The onset of this change in the optical properties appeared to be random, as triggering of this event was generated by an absorption locality. Anastasiou et al. reported similar results in performing high repetition rate processing of brushite [197], where sintering could be 'ignited' by placing a defect or absorbing medium on the surface to trigger a cascade absorption within the material.

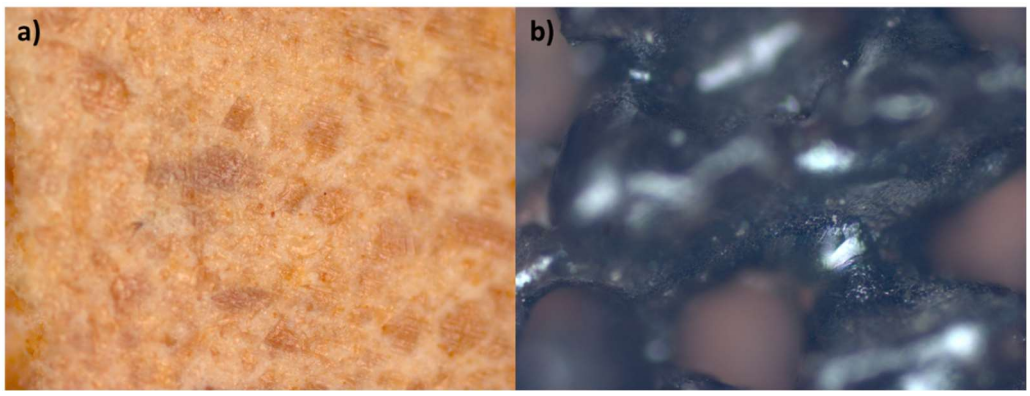

Figure 6.1: 10x optical microscope image of 5% FeHAp, a) before and b) after processing

For this reason, the following experiments were conducted with exactly the same laser parameters, in the attempt at reducing variables other than the material. The laser power was kept at 1.5W at 500 kHz, a pulse energy of 3μJ, and a spot diameter of 300μm, equating to an energy density of 4.25 mJ/cm^2, two orders of magnitude lower than the multiple pulse ablation threshold and a laser rastering speed of 1mm/s. The reason for the choosing these values for processing the pellet materials was that it was above the band of onset values for the initial materials test, but also lower than the darkening of the material and cascade absorption events.

6.2.2 Processing of Fe^{3+} doped hydroxyapatite pellets

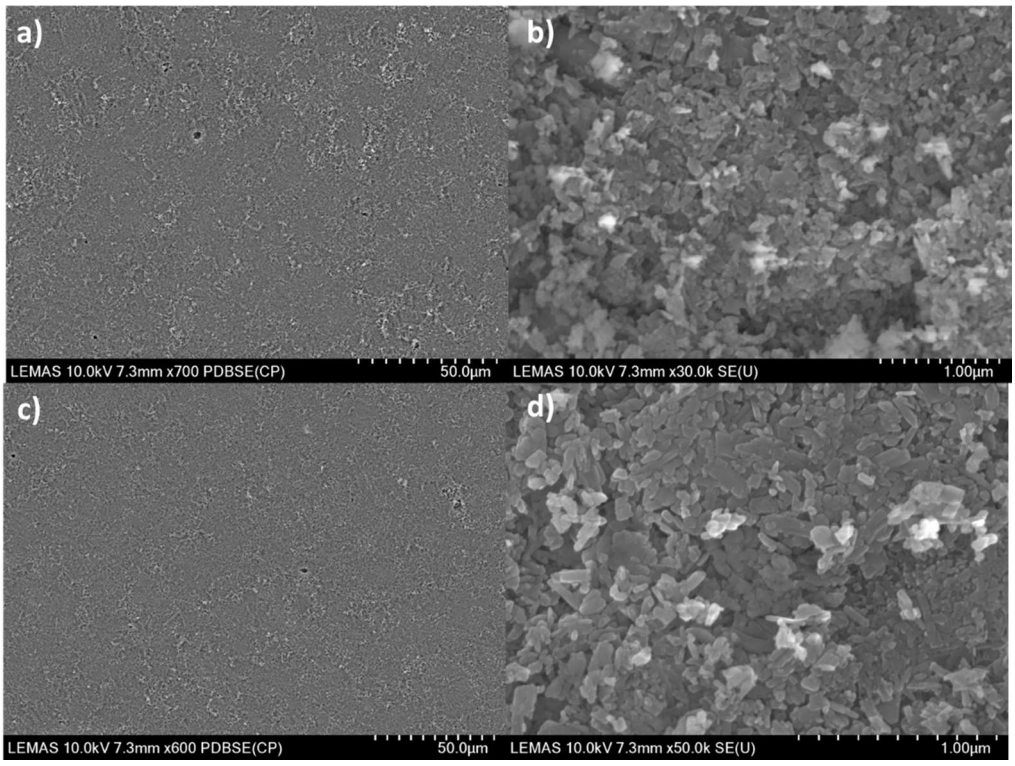

Figure 6.2: 0% FeHAp a, b) before and c, d) after processing

SEM images, Figure 6.1, of the 0% FeHAp before and after processing showed there is little change to the morphology of the surface. This is expected given that 97% of all the energy from the laser has been reflected away and with

nominal energy values. XRD of these surfaces, Figure 6.3, also confirms that there is no structural change post processing with the 500 kHz system.

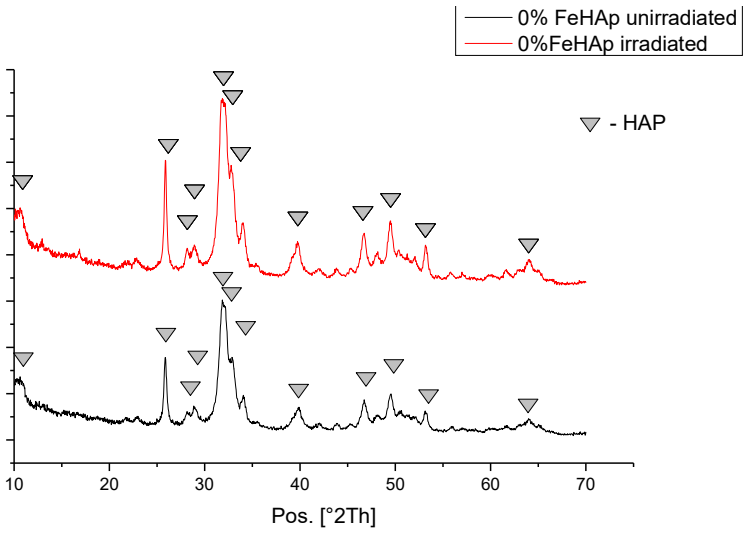

Figure 6.3: XRD of 0% FeHAp pre, and post irradiation.

SEM images of the 5% FeHAp before irradiation are shown in Figure 6.4, and after irradiation in Figure 6.5. In stark comparison to the results of the 0% FeHAp pellet irradiation trials, there is a definite difference between the raw and processed surfaces of the 5% FeHAp pellet. The raw pellet, Figure 6.4, shows compaction of agglomerates with cavities and morphological inhomogeneity.

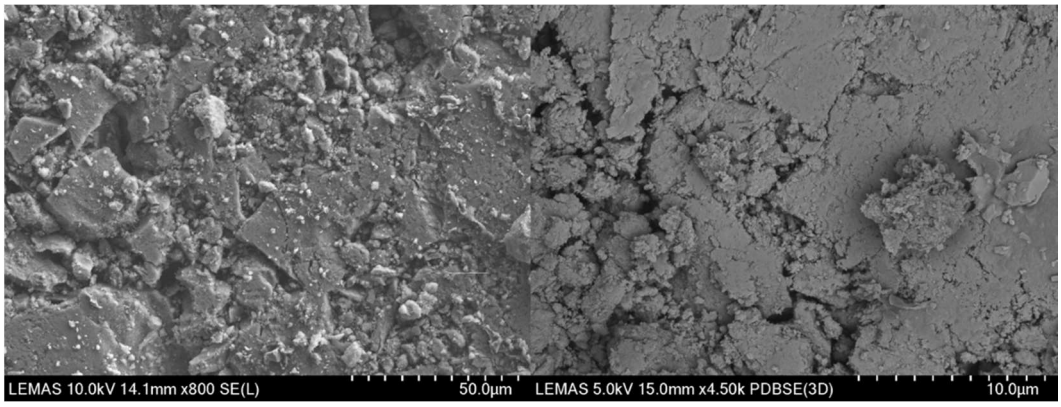

Figure 6.4: SEM images of the un-irradiated surface of 5% FeHAp pellet

Figure 6.5(a) shows the edge of the processed region, the bottom left of the image displaying the unprocessed region of the pellet surface, which is synonymous with Figure 6.4, and the right hand side of the image showing a clearly densified surface. Higher magnification of the densified region showed hexagonal features, approximately 10μm across, where minute dots, and regions of larger lighter tones amongst a clearly densified layer. The centre of these regions also had these lighter shaded dots, in back scattered electron images.

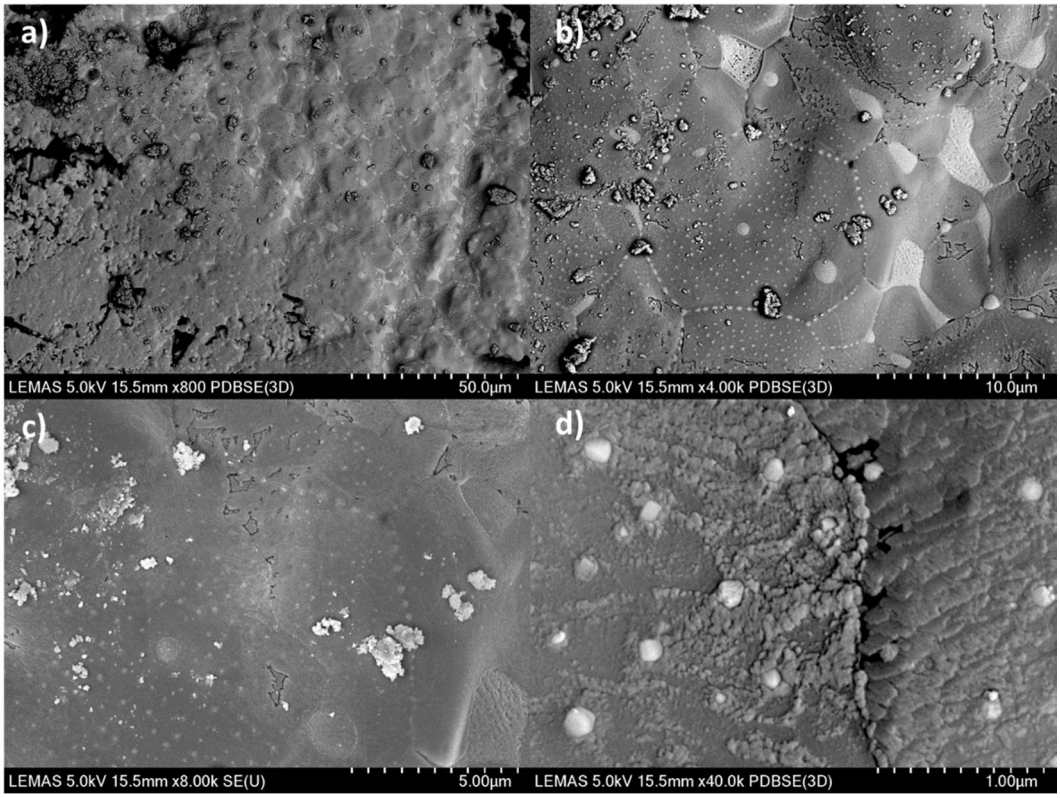

Figure 6.5: SEM images of the processed surface of 5% FeHAp pellet

X-Ray diffraction spectra of the post processed surface shows clear structural changes in comparison to the raw surface. The hydroxyapatite peaks have disappeared and weak peaks of Iron phosphate and β-Tricalcium Phosphate are now present.

This is in contention with the conventionally heated samples which produced a calcium iron phosphate and β-tricalcium phosphate mixture. The rapid heating and cooling of the material surface during processing is clearly too rapid. Melting is not apparent in the SEM images, therefore this is a solid-solid reaction, the solubility of the iron phase in the material at high temperature is discernibly low, and upon rapid cooling, this secondary phase is excreted.

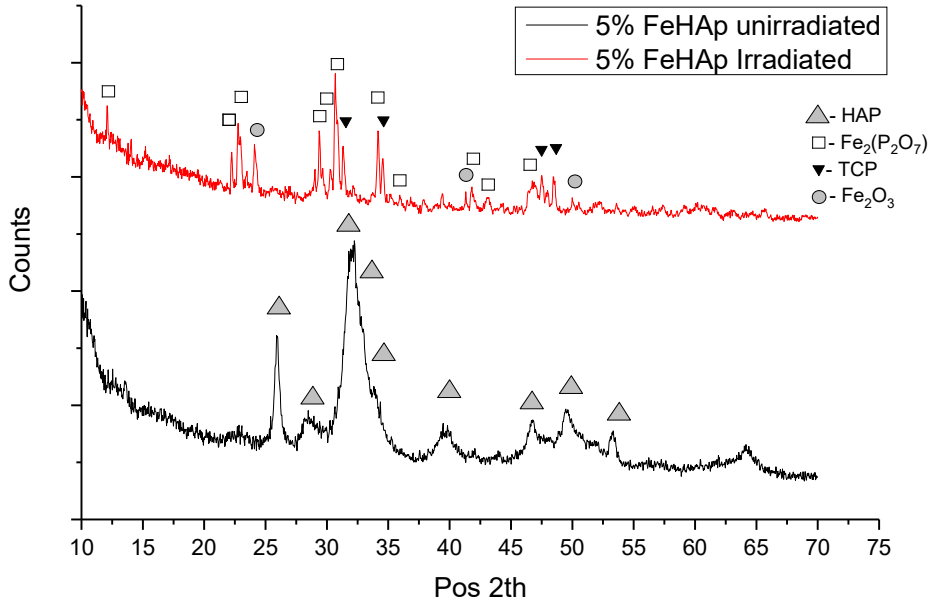

Figure 6.6: XRD of the 5% FeHAp pellet surfaces, pre and post processing

SEM images of the 10% FeHAp pellet, raw Figure 6.7, and processed Figure 6.8, show similar results to the 5% FeHAp. A clear morphological change has occurred between the samples showing successful modification of the material surface. In the processed sample, Figure 6.8, there is apparent cracking of the sample surface, in comparison to 5% FeHAp. This is likely due to excessive dehydration and mass loss, and also contraction of the densified parts. Since the material has higher optical absorption properties than the preceding sample, it's assumed that the energy deposited in to the material surface will be higher.

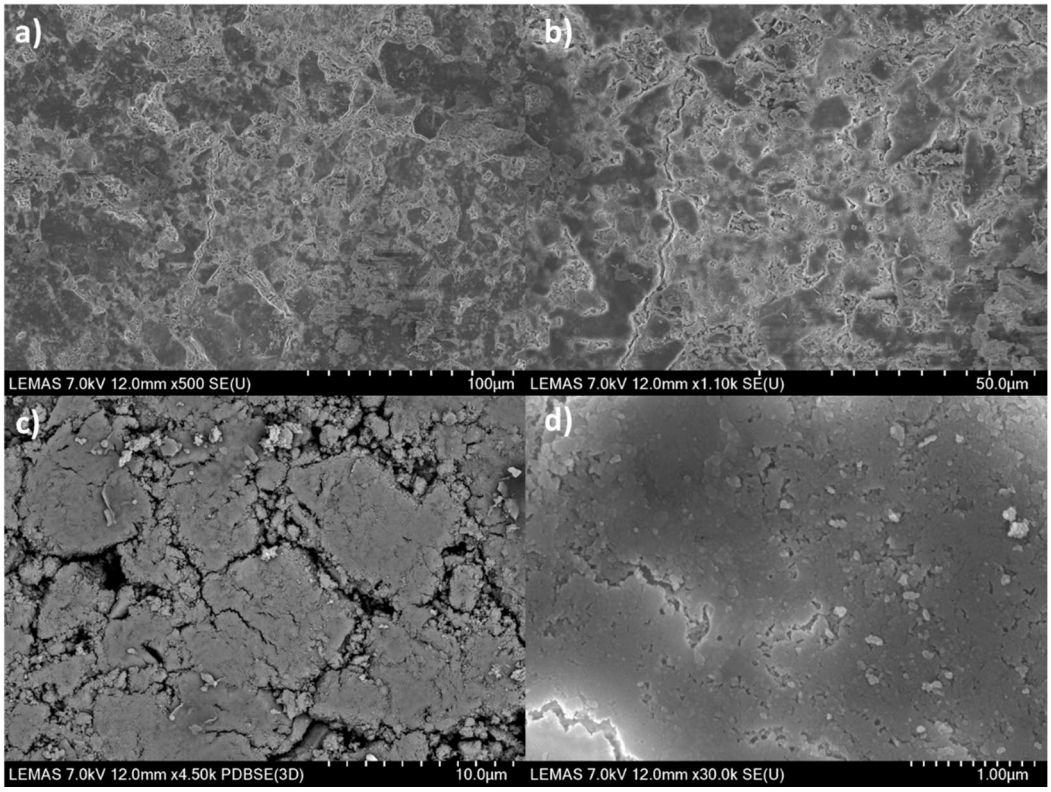

Figure 6.7: SEM images of the raw pellet surface of 10% FeHAp

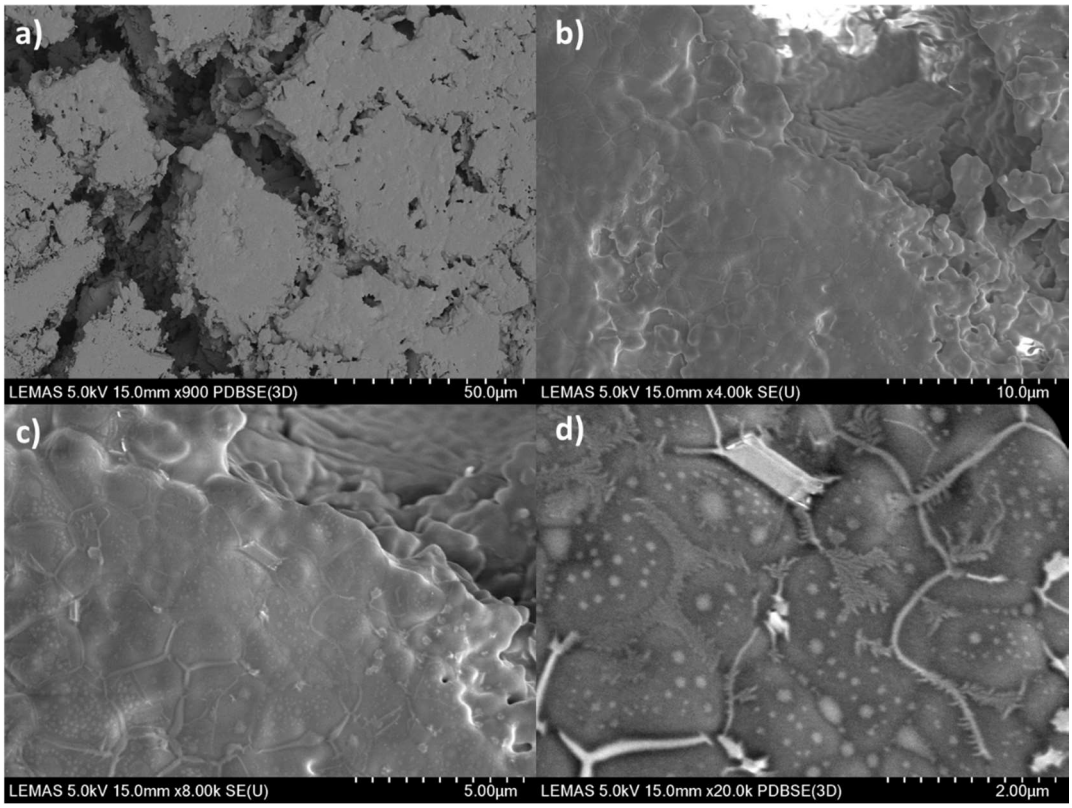

Figure 6.8: SEM images of the processed pellet surface of 10% FeHAp

Higher magnification of the densified regions, Figure 6.8(b, c & d) show a clear homogeneity, with hexagonal features appearing again. The dimensions of these hexagonal features appear to be smaller, however, of the region of 2µm. Further inspection, Figure 6.8(d) shows that in between these hexagonal sites there are strange dendritic features forming around edge, with veins connecting some of them, and a mottling of condensation like blotches. This is likely to be leaching of the in soluble parts of the solid solution anneal quickly forming these structures

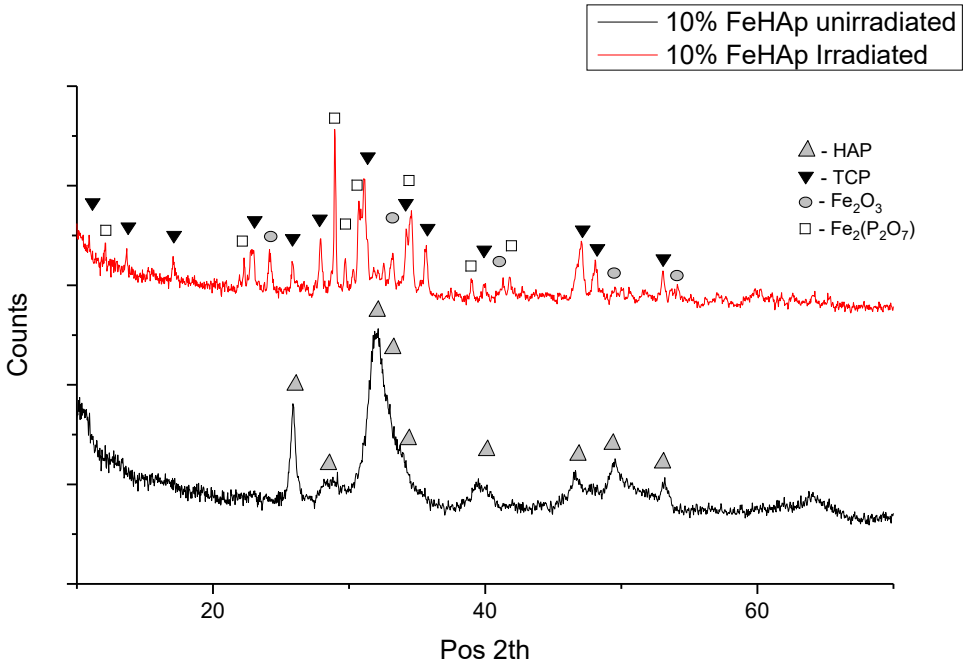

Figure 6.9: XRD comparison of un-irradiated and sintered 10% FeHAp pellets

XRD of the processed 10% FeHAp surface, Figure 6.9, reveals that the structural change from hydroxyapatite to iron phosphate, tricalcium phosphate and hematite. Conventional heating of this material resulted in solely calcium iron phosphate, suggesting that the ejected material surrounding the hexagonal structures is iron oxide.

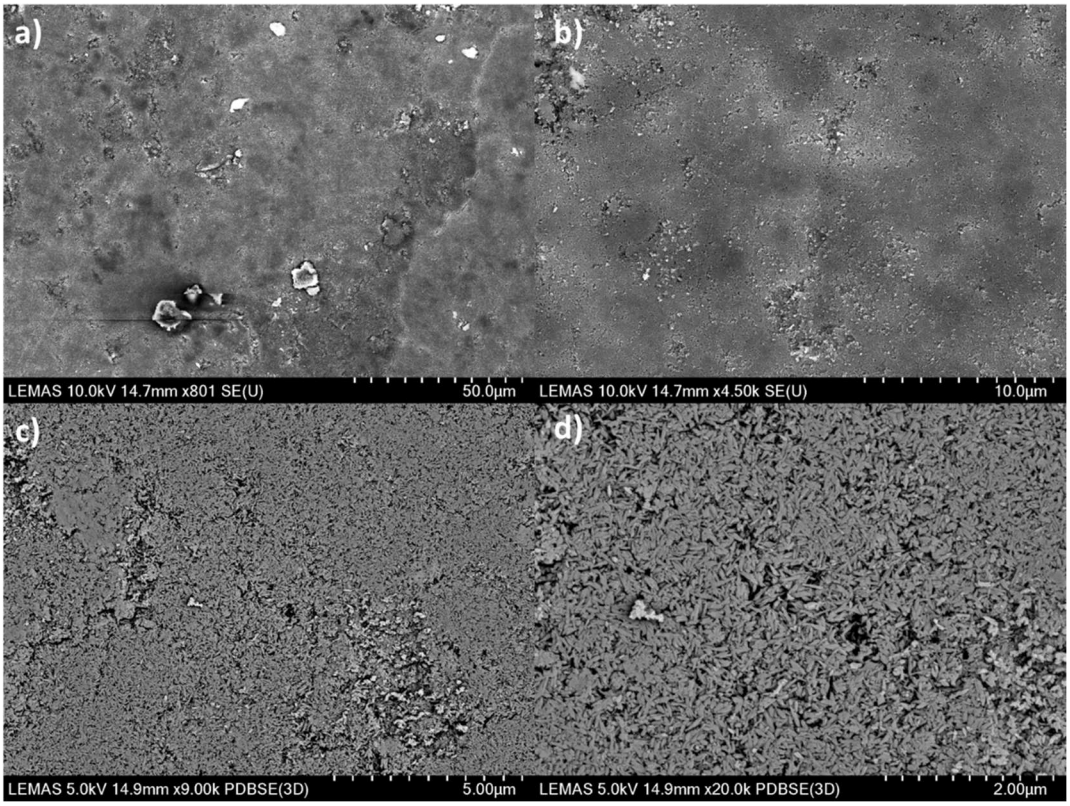

Figure 6.10: SEM images of the raw pellet surface of 20% FeHAp

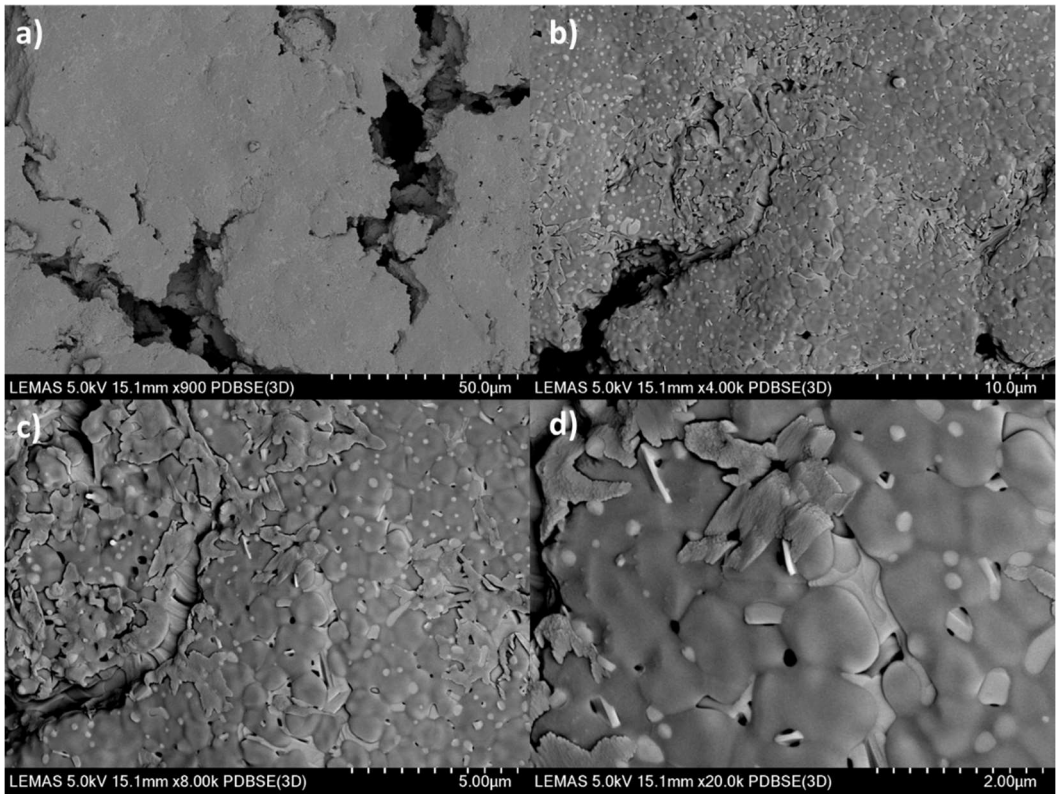

Figure 6.11: SEM images of the processed pellet surface of 20% FeHAp

SEM images of the raw, Figure 6.10, and processed, Figure 6.11, 20% FeHAp pellet surfaces shows similar results to 10% FeHAp. Clear modification of the material surface with cracking, hexagonal crystallites forming, however, these features are smaller again at approximately 1µm across, although this might be a function of preceding crystallite size, as discussed in §3.3.2. Ejections in the form of mottling and dendritic structures appears to be greatly reduced, instead, there is an abundance of secondary interstitial phase.

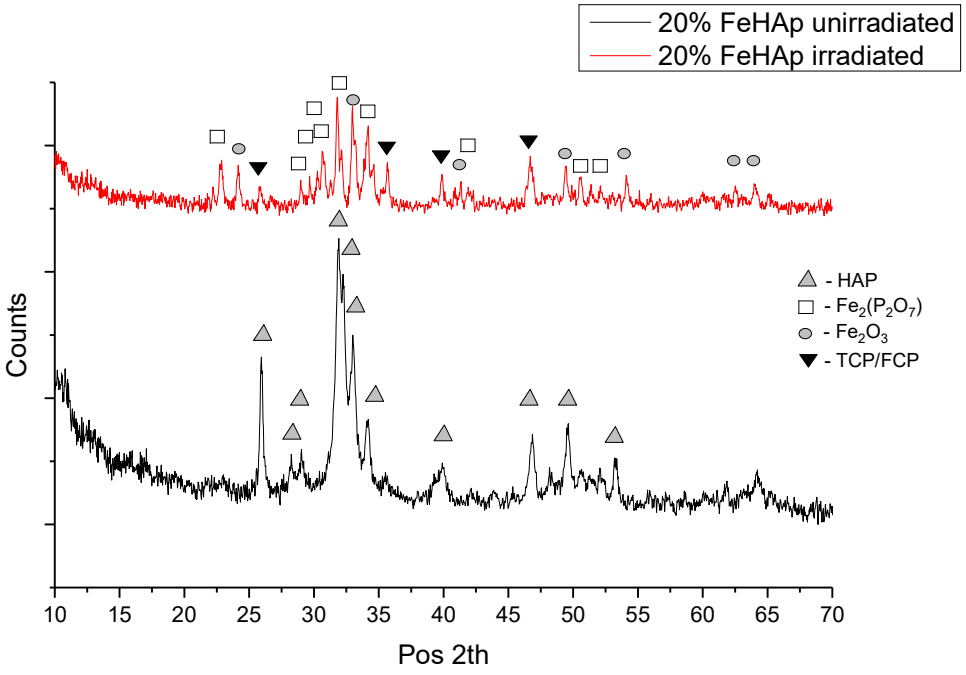

Figure 6.12: XRD of 20% FeHAp pellets, before and after processing.

XRD spectra of the processed 20% FeHAp, Figure 6.12, shows increased intensity in hematite peaks. However, less intensity in other phases, Iron phosphate being the other prominent phase. This is unexpected, as we would expect the higher absorption properties of the 20% FeHAp material to allow for higher energy deposition into the material surface. The SEM images show clear densification and yet the XRD spectra is weakly crystalline.

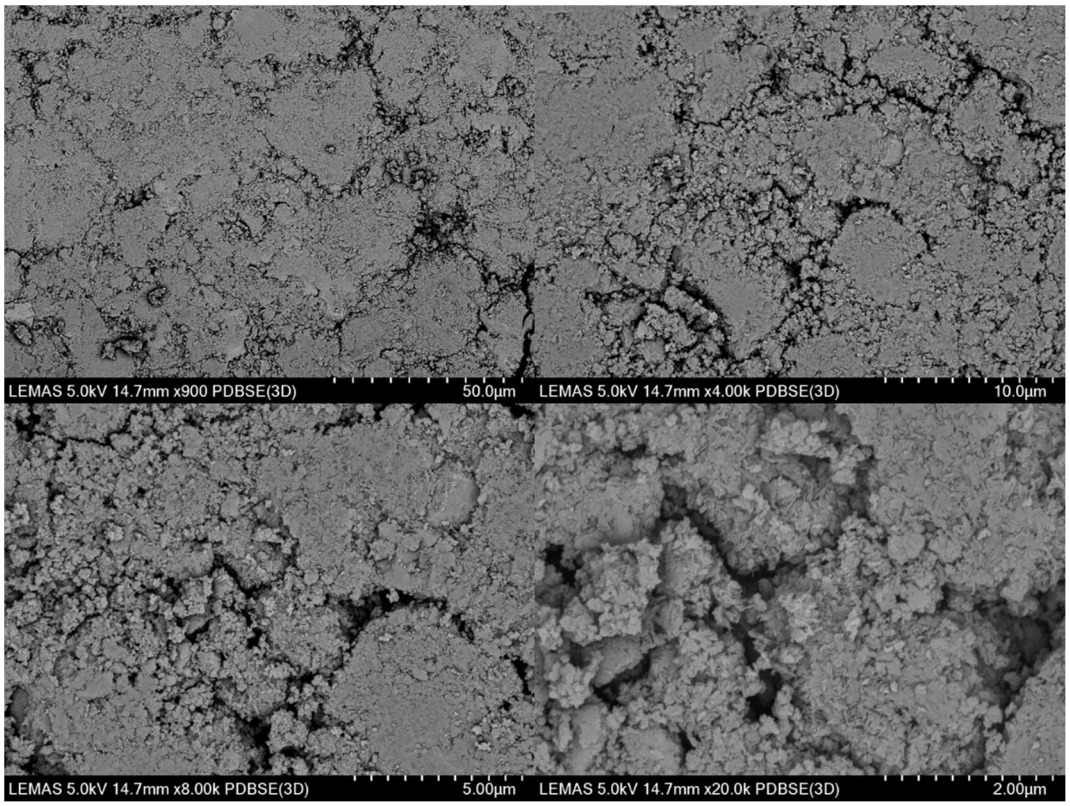

Figure 6.13: SEM images of the raw pellet surface of 30% FeHAp

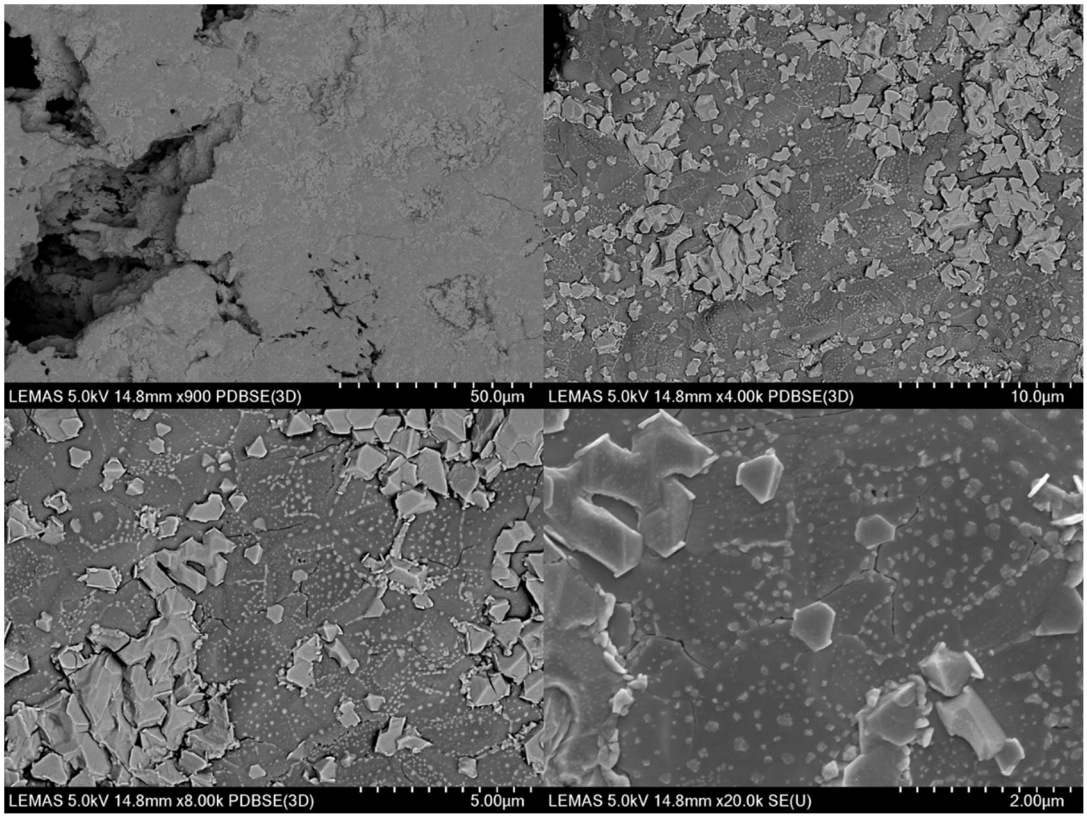

Figure 6.14: SEM images of the processed pellet surface of 30% FeHAp

The difference in morphology between 10% FeHAp and 20% FeHAp samples, appears to have been scaled further with the 30% FeHAp. SEM images of the raw, Figure 6.13, and processed, Figure 6.14, surfaces of the 30% FeHAp demonstrate again clear modification of the material surface. Cracking is still present, however, the underlying layer is now consolidated, with no hexagonal features of the underlying material. There is, however, a much increased abundance of secondary crystallite phase, rhombohedral in shape.

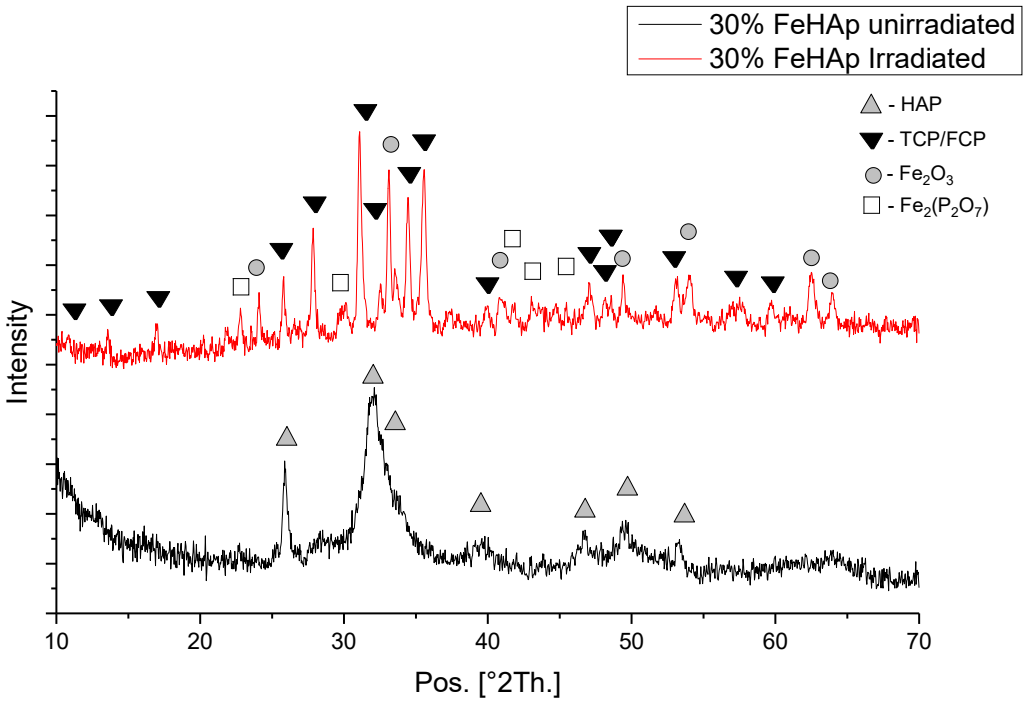

Figure 6.15: XRD spectra of the raw and processed 30% FeHAp pellets

The XRD spectra of the raw and processed 30% FeHAp pellets, Figure 6.15, showed a much more crystalline pattern. Much stronger hematite peaks are present, confirming that the rhombohedral surface crystals are Iron oxide. Secondary calcium iron oxide peaks are prominent, in contrast to the 20% FeHAp sample.

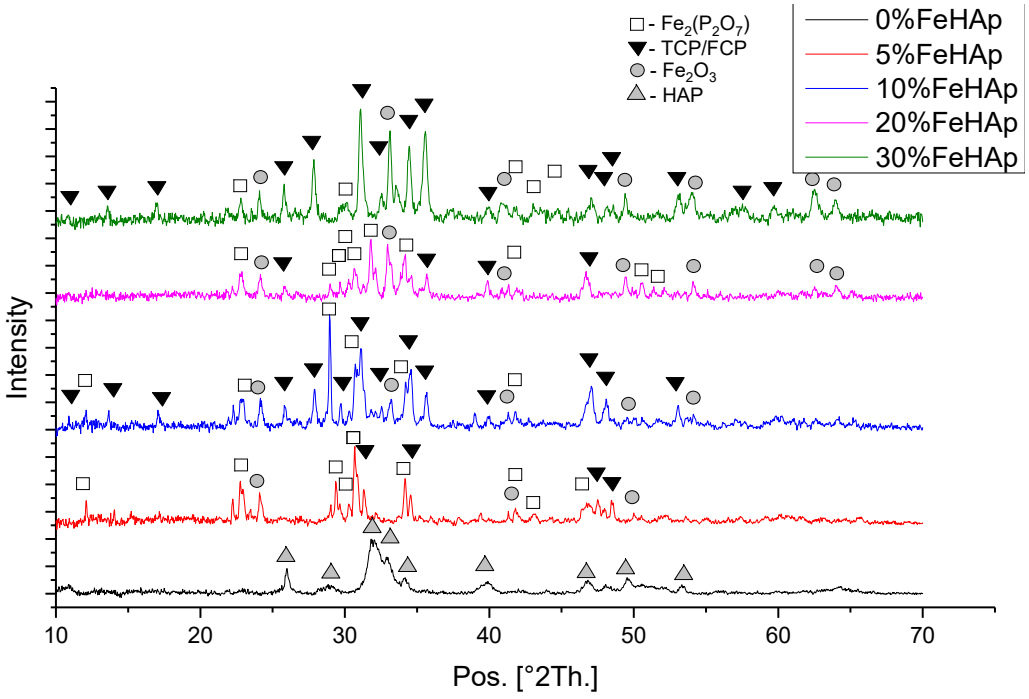

Figure 6.16: XRD spectra for processed 0-30% FeHAp

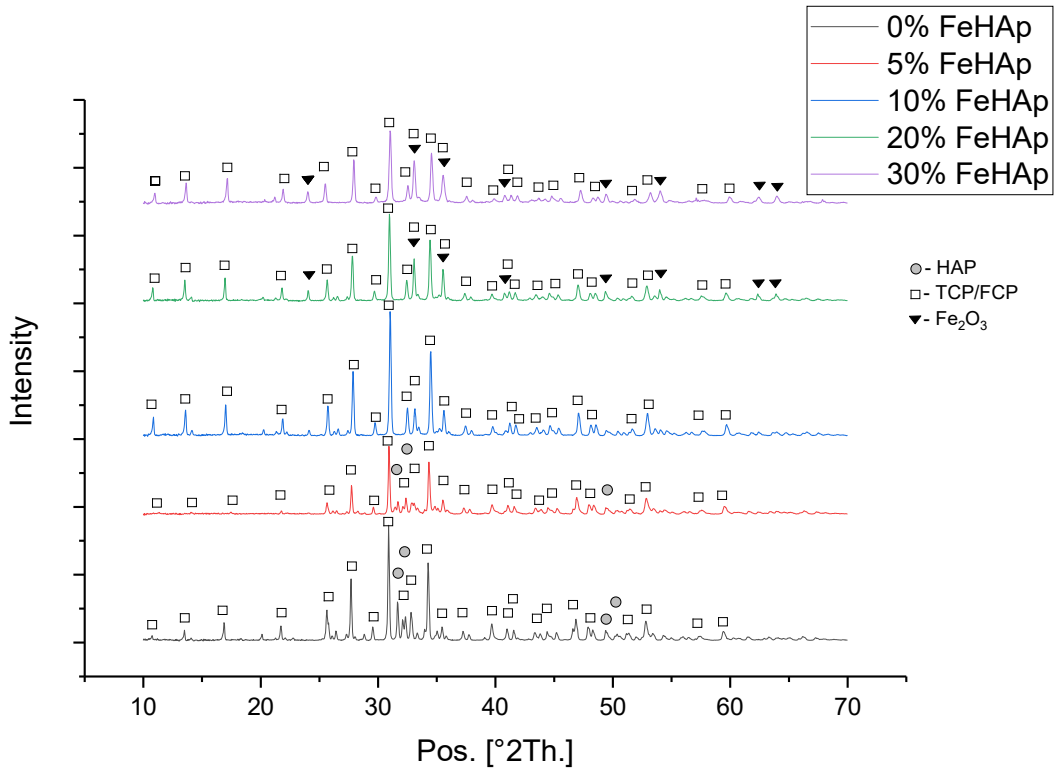

Figure 6.17: XRD of generically heated samples

Comparison of all the sintered samples can be seen in Figure 6.16. The most noticeable difference between samples in this case is not only the intensity of hematite peaks with increasing doping concentration, but also the emergence of the iron phosphate phase in the 5% and 10% FeHAp samples, which disappears at 20% and 30% FeHAp, this is most perceptible with the peak at 2Θ = 28.948. After 20% the main phase reverts to calcium iron phosphate. It is perhaps this transition that has limited the crystallinity and peak intensity in the 20% FeHAp sample.

Absorbed laser energy will scale with the doping concentration due to the increased optical absorption properties of the materials with increased Fe^{3+} concentration. We can therefore expect the 30% FeHAp sample to have achieved the highest temperature out of all the samples considering the processing conditions remained constant. The maximum temperature of the laser affected volume will be obtained in a second or so, as the laser spot will only reside on the same point for fractions of a second. With an extremely rapid heating rate and upper temperature limit, there may have been a phase transition that we couldn't have observed in either the thermal analysis or heated XRD. Comparing the laser processed samples to the conventionally heated samples, Figure 6.17, shows a dramatic difference in the product of the different processing methods.

Since such a small volume will have been heated in comparison to the bulk, there will be extremely high temperature gradients across the material surface. This will also cause rapid cooling or quenching to occur as heat will travel with respect to the gradient vector. Solid solutions that are in equilibrium at high

temperature may not be stable at room temperature, and would therefore eject from the solid solution, which is likely represented by the emission of hematite phase onto the material surface.

Unfortunately, shortly after these experiments were conducted LaserINN went into administration and further study with the use of this laser system was not possible.

6.3 Conclusions

500 kHz laser processing of all the synthesised materials was accomplished. Initially, investigation into the energy minima required for material interaction was undertaken, however, this produced anomalous results due to random highly absorbing points on the material surface enabling sintering ignition.

The formation of a black surface post processing also generated issues when considering the amount of deposited energy to the surface, as the darker hue present in the material will have caused a non-steady state absorption profile in the material.

Sintering was accomplished with some efficacy, as densification was apparent on all but the 0% FeHAp surface. Large scale uniform sintered layers were hindered due to cracking, a product of surface material shrinkage compared to the bulk. SEM investigation of the processed surfaces revealed increasing ejection of a secondary phase to the material surface with increasing doping concentration. XRD analysis of the surfaces then confirmed and increased

presence of Iron (III) oxide, which further explains the black colour formed on the material surface post processing.

Comparison of the conventionally heated samples and the laser processed samples showed drastic differences across all the materials. This is due to the rapid heating and cooling rates that are present in the laser affected region. The speed and rates could account for previously unseen phases in the material, such as iron phosphate, that were not present in the conventionally processed results. Due to the short time frames in processing, thermal stability of these phases upon rapid cooling will likely have been nominal, and therefore caused the phase separation observed in the SEM and XRD spectra.

7 High repetition rate femtosecond laser interactions with Calcium Phosphates.

The rapid heating and cooling cycles and relatively low duty cycles accomplished in the previous chapter had a clear effect on the final product of the sintering process. Utilisation of a higher duty cycle, lower powered system may generate results that are more successful at creating homogenous sintered layers on the material and substrates.

In this chapter a 1GHz femtosecond laser system is used, the objectives of the given experiments are to observe the efficacy of this repetition rate on the materials and substrates for modifying the materials thereof.

The first section, 7.1, considers the laser systems used and certain experimental parameters. Section 7.2, investigates modification of the synthesised material pellets with this laser system. In section 7.3 and 7.4, coated titanium and dental substrates are processed with the synthesised materials. Finally, section 7.5 discusses the main findings and observations.

7.1 Methods

Materials were prepared as per §3.4.

7.1.1 Laser system

The laser system used for these experiments was a custom made Yb:KGW solid state laser, situated and made by colleagues at the University of St. Andrews, Physics and Astronomy department. Utilisation of this system and the control software was accomplished with the aid of Dr. Tom Edwards, and Dr. Caroline Thompson.

The laser had a centre wavelength of 1020nm, a 1GHz repetition rate, 120fs pulse duration, and a maximum average power of 0.4W. The laser energy could be controlled with a variable optical density filter and was measured with a pyroelectric energy meter.

The laser was housed on a breadboard optical bench and the beam was directed out the housing through a lens onto a Thorlabs MT3-Z8 3-axis motion stage which was controlled through LabView.

The spot size was characterised via a beam profiler to be 30μm at the focal spot, the centre of which was determined by writing lines into a dark piece of card. The card was then inspected under a microscope and the relative position of the narrowest line was correlated to the motion stage z-axis, and therefore the central position of the laser focus.

Being a custom made research laser system, the stability of the output was often disrupted by variations in temperature or vibration, which often caused problems during experimentation.

7.2 Pellet experiments

The pellets were placed onto the motion stage and the appropriate height of the stage was set to obtain the spot focus onto the surface of the pellet. The laser was then set to full power at the time of experimentation, yielded 0.34W, and the raster speed was 100µm/s, in order to maintain the same exposure duration per unit spot area as the previous 500 kHz results, as the spot was 30µm. With these parameters the fluence was therefore 4.81×10^{-5} J/cm^2, nearly two orders of magnitude lower than the previous experiments, and far below the multi-pulse ablation threshold.

7.2.1 SEM results

SEM results for the 0% FeHAp, Figure 7.1, showed little material change across the surface of the pellets. There was an increase in abundance of pits on the surface, as can be seen in Figure 7.1(b) on the right hand side of the image, this is assumed to be removal of small localities from the pellet surface.

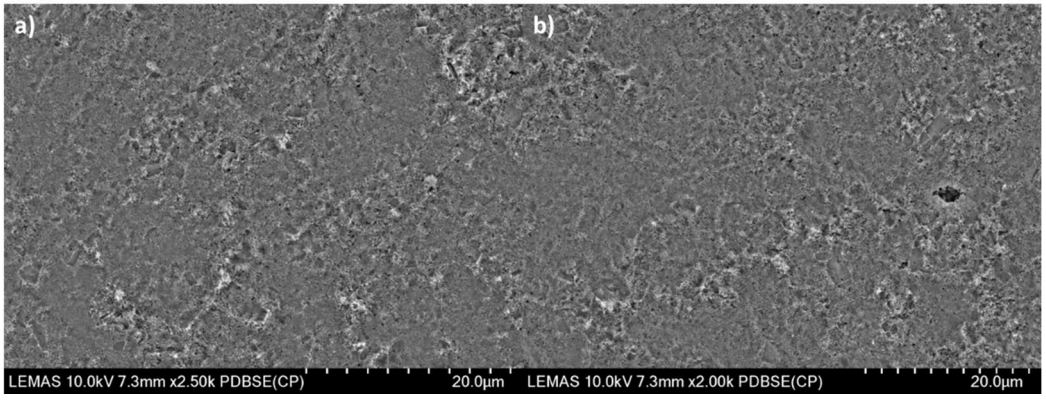

Figure 7.1: SEM images of 0% FeHAp a) before and b) after

5% FeHAp displayed crack formation and layer peeling, Figure 7.2, this is indicative of mild heating and dehydration of the material surface. 10% FeHAp displayed more curious results, and clear morphological change, Figure 7.3. The

surface appears to have become plastic during irradiation. The sweeping patterns, as shown most clearly in Figure 7.3(d), and across the surface of the irradiated area is suggested to be due to the motion of the stepper motor driving the rastering.

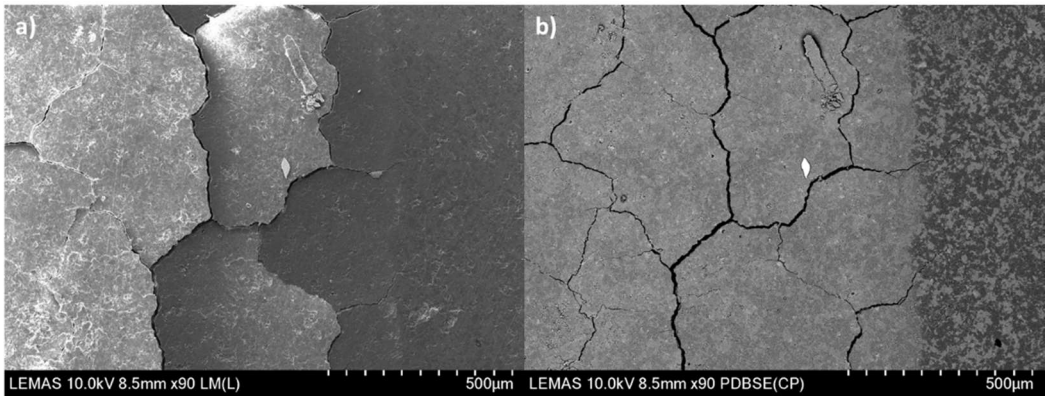

Figure 7.2: SE SEM and BSE SEM of 5% FeHAp processed boundary

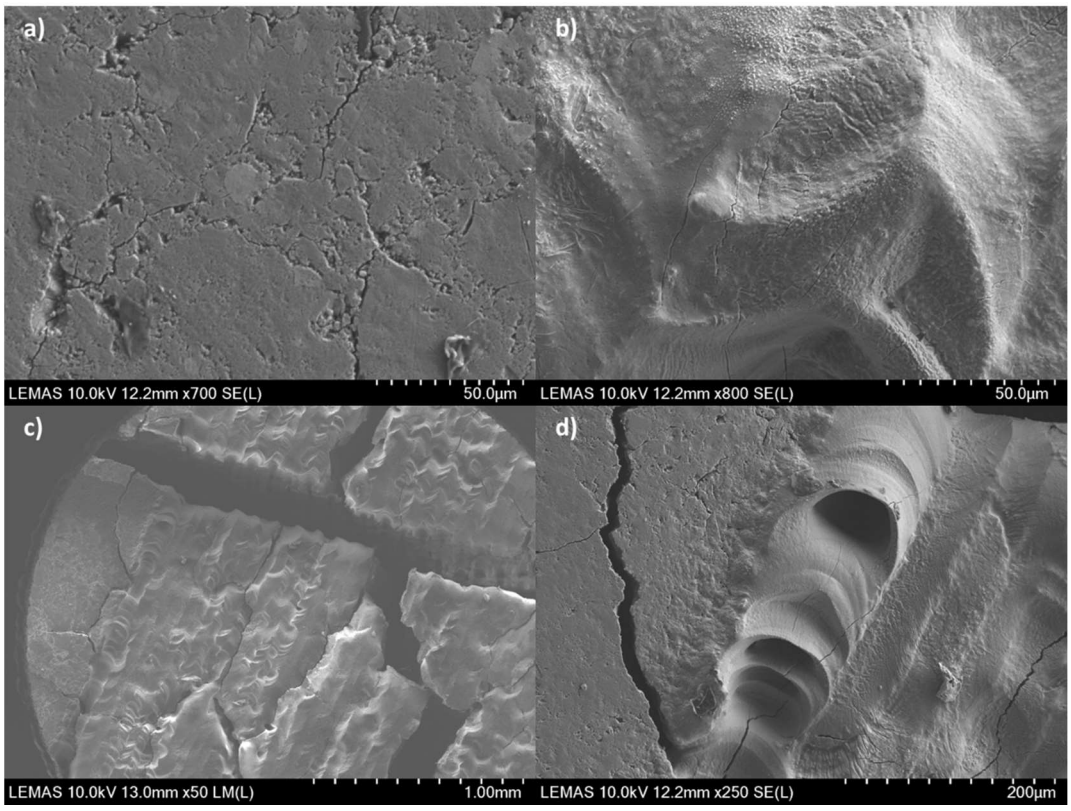

Figure 7.3: SEM of 10% FeHAp for a) unprocessed, b) processed, c) macro area of processed region and d) processed region edge

The 10%, 20%, and 30% FeHAp surfaces after irradiation were all black in colour and resembled the macro image in Figure 7.3(c), in morphology. Huge faults and cracks formed amongst rows of trough and peaks of material that mirrored the raster spacing of 30µm.

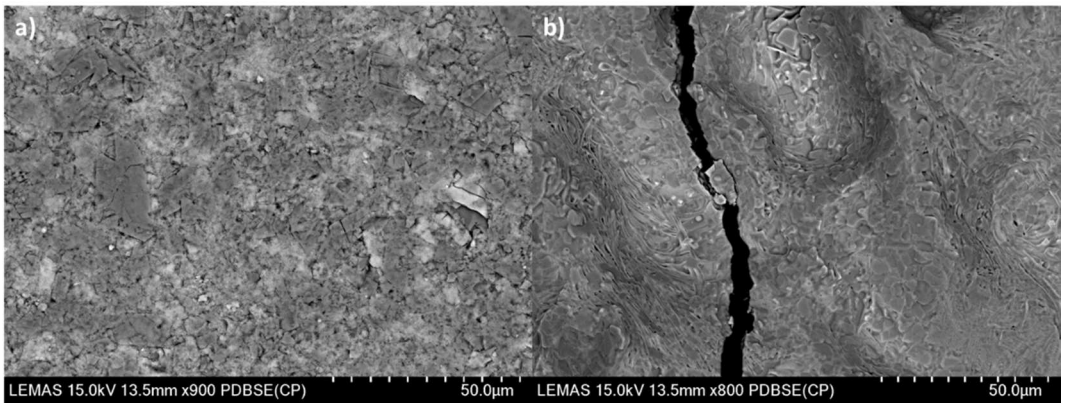

Figure 7.4: SEM of a) unprocessed and b) processed 20% FeHAp

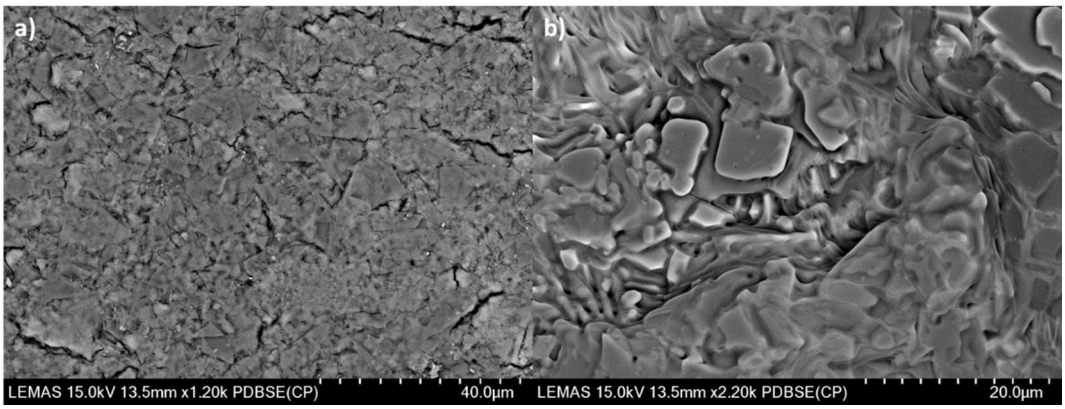

Figure 7.5: SEM of a) unprocessed and b) processed 30% FeHAp

Figure 7.4 and Figure 7.5 show the pre and post processed SEM images of 20% FeHAp and 30% FeHAp, respectively. The processed surfaces show undulations of the raster track path, and small crystallite, approximately 5µm in dimensions on the surface, which appears densified and crystalline. There are no apparent hexagonal features or ejections from the material surface.

7.2.2 XRD results

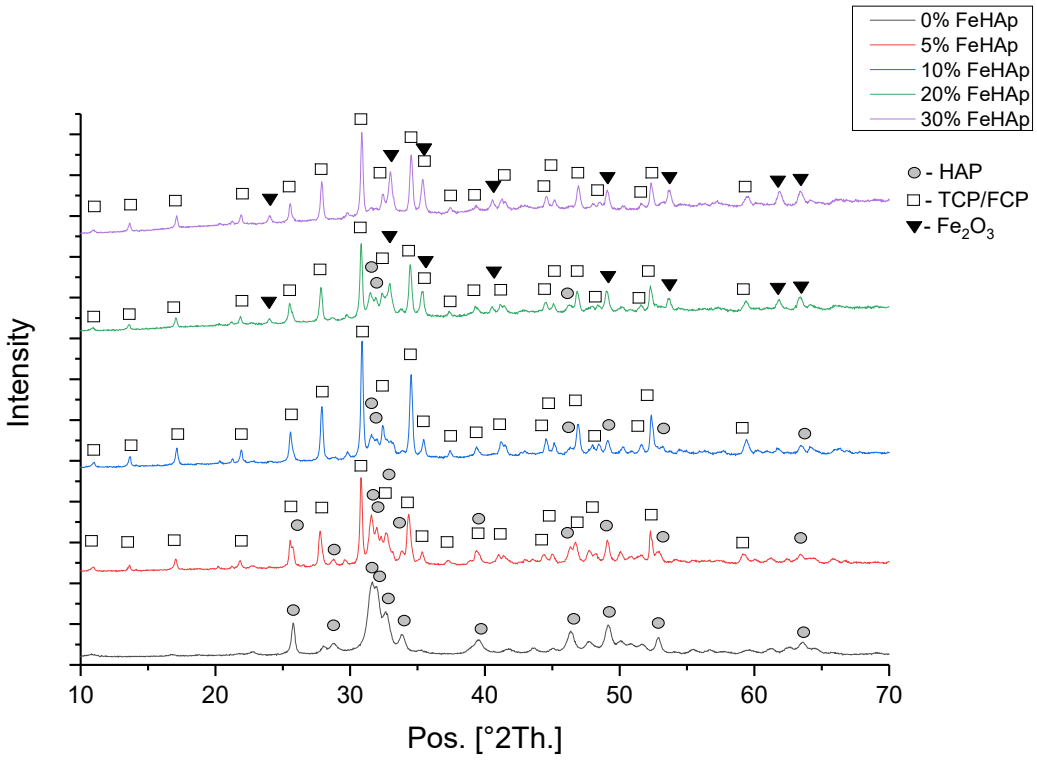

Figure 7.6: XRD spectra of the processed pellets

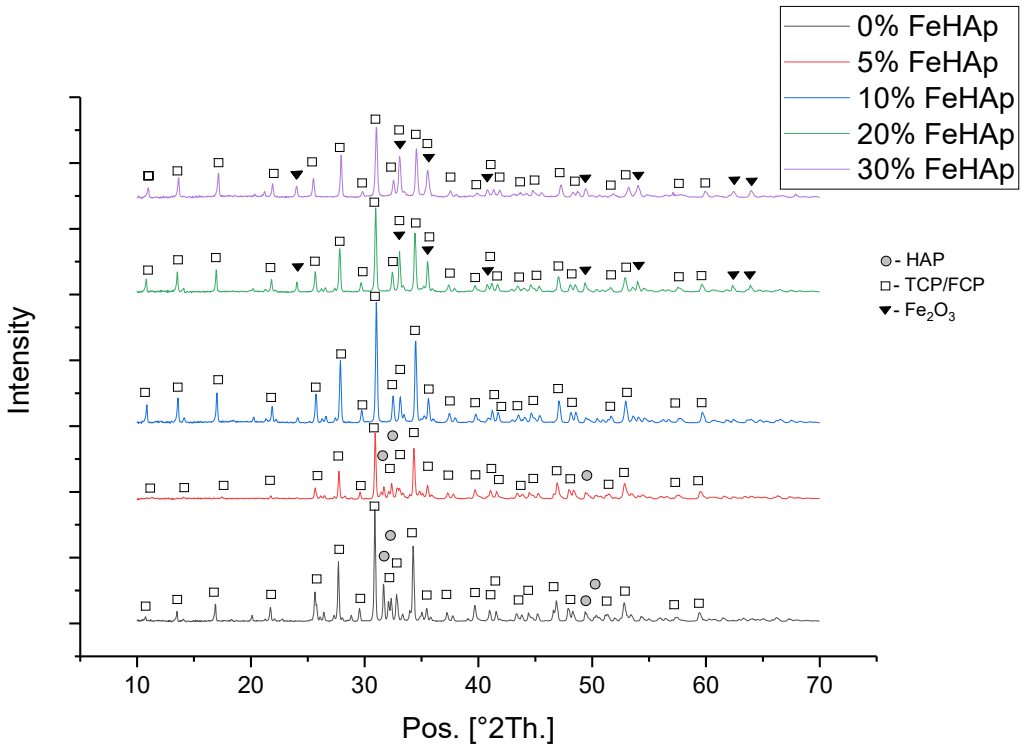

Figure 7.7: XRD spectra for the conventionally heated samples

The XRD spectra of the processed samples, Figure 7.6, show that the 5%-20% FeHAp samples still have remnant hydroxyapatite peaks in the material as well as forming the calcium iron phosphate peaks. Weak iron oxide peaks begin to form at the 20-30% region, not nearly as prominent as the prior 500 kHz results. However, there is a lot more coherence in the results in terms of peaks and intensities.

7.2.3 Discussion

The smooth undulating surfaces and lack of ejected secondary phase appears to hold a different result to the previous 500 kHz. The explanation for this would be that the duty cycling of the lower energy pulse train does not cause such rapid heating and cooling cycles that might shock the material in and out of the saturation point of the structural iron content.

The colour of the processed surface is not so easily explained with the presence of surface iron oxide, and can only therefore be explained by the presence of calcium iron phosphate, a reddish hue material normally, but much like hematite, the iron oxidation state dictates the colour of the material.

The XRD spectra reveals that there is prominent hydroxyapatite still within the structure of the processed layers of most of the materials, this indicates that a temperature of 700°C has been achieved, on the surface layer, not enabling all of the material to decompose. It can be assumed also, that due to the speed of this heating and cooling rate that there isn't time for the water in the material to escape. This could perhaps explain the presence of the undulations and plastic like response of the material with the laser, where the hydrated crystals allow for flexible movement amongst one another during heating.

7.3 Coated Ti-6Al-4V substrates

7.3.1 Results & discussion

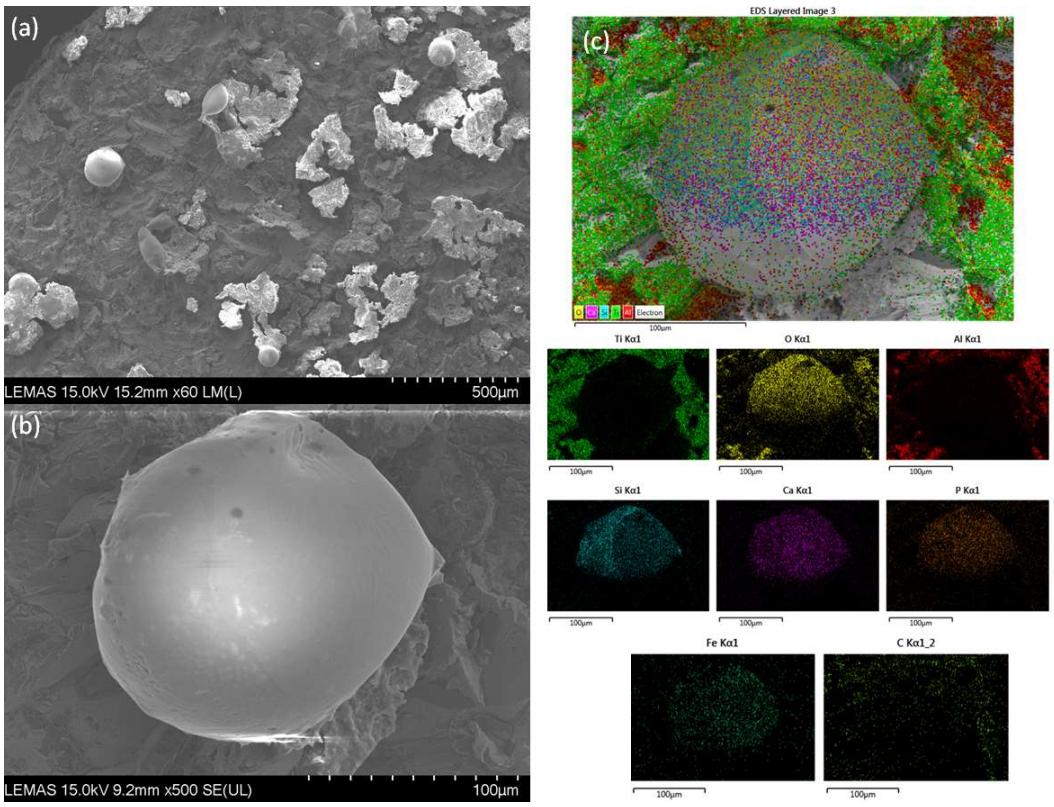

Figure 7.8: SEM and EDX mapping of processed 10% FeHAp on Ti-6Al-4V substrate

Ti-6Al-4V substrates were coated and processed with the same conditions as the pellets. The results in Figure 7.8 are of 10% FeHAp on the Titanium surface post processing. It can be seen that the laser has managed to interact readily with the material coating, and cause a wake of material in the laser path. Along the laser raster line are bulbous balls of FeHAp on the titanium surface.

EDX mapping of the bulbous feature confirms the presence of iron, calcium, phosphorus and oxygen. Proving that these are indeed features generated by the laser and the coated material.

The titanium surface appeared to be unscathed by the processing of the laser, the bulbous material clearly not being able to wet adequately onto the titanium surface.

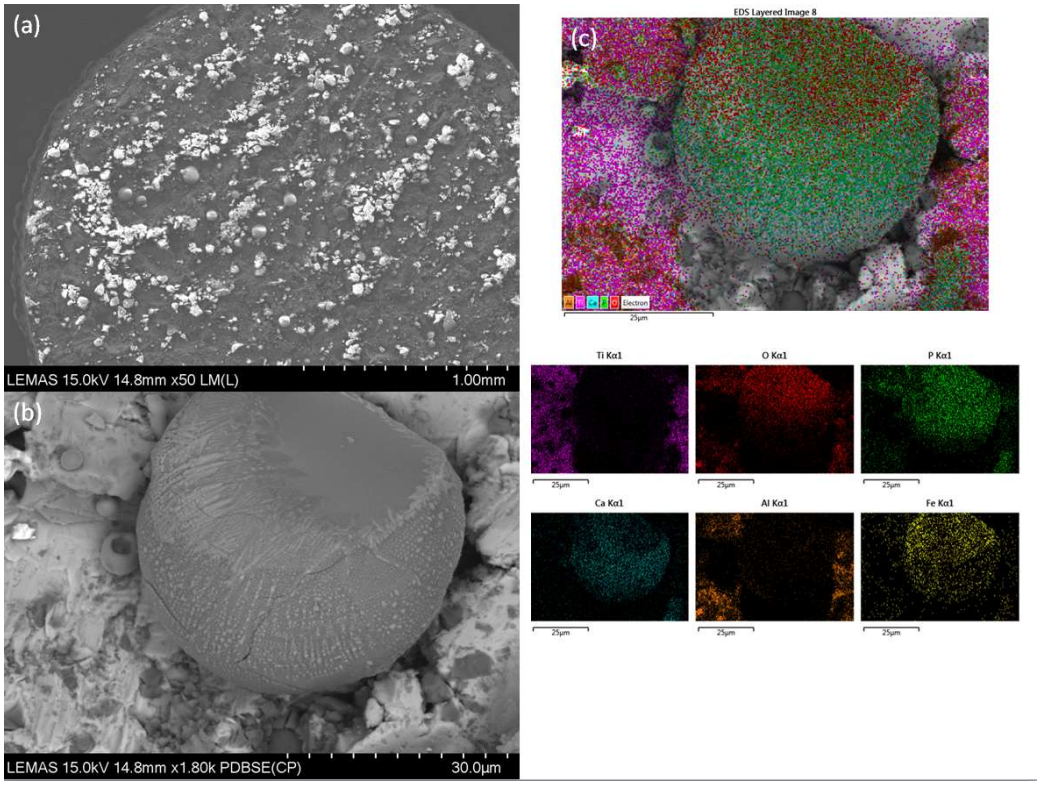

Figure 7.9: SEM and EDX mapping of processed 20% FeHAp on Ti-6Al-4V substrate

Figure 7.9 shows another experiment with 20% FeHAp on the Ti-6Al-4V substrate and has almost exactly similar results to the 10% FeHAp. In the case of the bulbous feature in the 20% FeHAp example, however, there are mottled striations of ejected iron rich material on the ball surface. These appear synonymous with the hexagonal ejections seen in the 500 kHz experiments. This may indicate the generated ejections observed earlier are either a result of the heating or cooling process, as material confined onto a metal substrate will likely have increased thermal diffusive abilities in comparison to bulk.

7.4 Coated enamel substrates

7.4.1 Results & discussion.

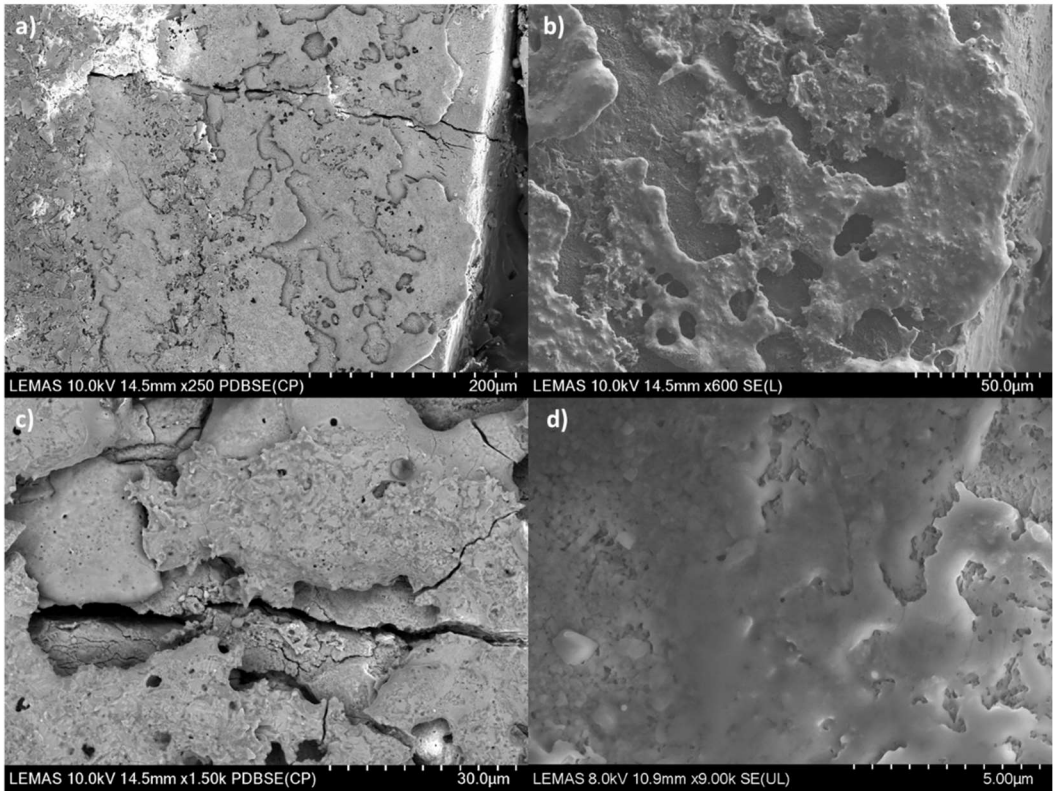

Figure 7.10: SEM of coated processed 10% FeHAp on dental enamel

The enamel coated surface was processed with the same conditions as the pellet. In Figure 7.10, we see a 10% FeHAp coating on the enamel surface that has managed to create an apparent melt. The smooth edges and neck between conjoined parts of the coating suggest that. It is apparent though that the coating does not appear to have welded with the surface of the enamel particularly well.

The melting of the material surface with the same conditions suggests that there is an effect of thermal diffusivity and confinement with the coating layer on the enamel. This would mean that the energy deposited is solely going into a thin layer, which explains why a melt has formed on this occasion.

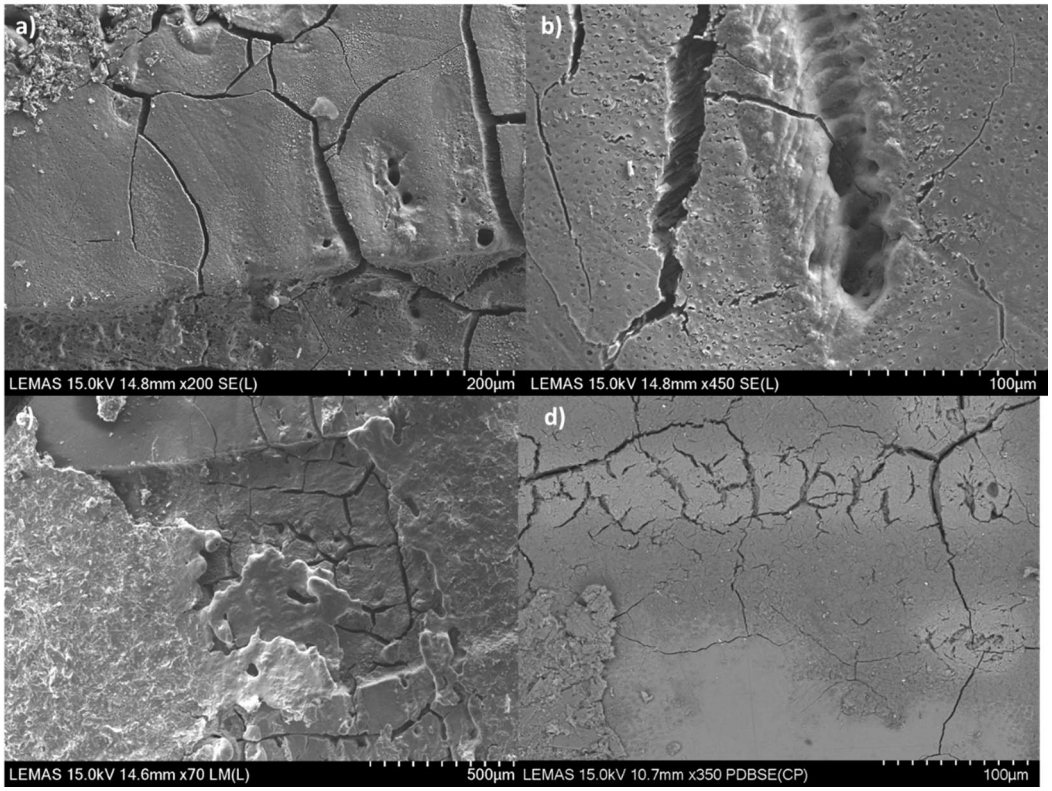

Figure 7.11: SEM of enamel surrounding the processed regions

It is clear however, Figure 7.11, that across these 4 different samples, the enamel substrate may also burn and char with the laser in this regime. Decomposition of the underlying enamel substrate, like triggered by this ignition method, as discussed in §6.2, organic parts of the enamel structure evaporate and decompose at 350°C.

7.5 Conclusions

1 GHz repetition rate laser source can be utilised to process the surface of Fe^{3+} doped hydroxyapatite materials. The results are in stark comparison to the 500 kHz repetition rate examples. This is likely due to the lower peak power/intensity and higher duty cycle, allowing for slower more even deposition of the laser energy.

Strange undulating morphology in the processed materials surfaces was determined to be a plastic like response to mobile water in the structure that could not escape in the heating/cooling cycle time frame.

The XRD spectra determined that the temperature of these materials did not excess 700°C due to the presence of hydroxyapatite for all samples. This temperature also not adequate to separate any iron phases from the material, the colour of the processed material surface must therefore come from the calcium iron phosphate phase, and iron oxidation in the structure of that.

Coating and processing Ti-6Al-4V substrates proves successful in sintering some of the layer onto the substrate. However, wetting of the bulbous particulates was poor, and likely would not withstand any mechanical aggravation.

Enamel coatings were also successfully prepared and processed, but similarly to the titanium substrate, adhesion of the layer onto the enamel surface did not appear to be adequate. Processing of the enamel substrates with this system could also generate decomposition of the underlying enamel itself, which brings the question of patient safety should this method be utilised if it has been demonstrated to damage the enamel substrate surface.

8 Conclusions

The outlined problems of hip replacement revisions and dental hypersensitivity are troubling issues that are yet to find an effective solution. The proposed solution of utilising modern laser technologies and materials science certainly gave an idea of an approach that could be exploited in solving these problems.

The aims of the study then were to adapt calcium phosphates for to the use with femtosecond laser sources to modify them subsequently as a solution to the outlined problems. The literature was fairly short of studies in this regard with the exception of my predecessors and colleagues. This presented itself an opportunity to explore this region of understudied research and attempt to generate a solution.

Hydroxyapatite was chosen as the base calcium phosphate mineral for this study due to its presence in bone and teeth, excellent bioactive and bio-reabsorption properties, and flexibility in modifying its structure in synthesis.

Considering that the laser sources to be utilised were also in the near infrared, in order to be within the 'biological window' of tissue penetration depth, Iron was selected as a material dopant, as its near infrared absorption properties

lead to efficient non-radiative multiphonon emissions, therefore transmitting any absorbed energy into the lattice.

The synthesised materials were prepared with doping concentration profiles of 0%, 5%, 10%, 20%, and 30% Fe^{3+} substituting ions into the hydroxyapatite structure. Characterisation of the synthesised powders showed that the iron had entered into the crystal structure, however, in the process disrupting it and the crystallites bound together readily forming agglomerates in the powder of various size. Further analysis proved that hydroxyl groups was being attracted into the structures with the introduction of the more valent Fe^{3+} cation.

Optical spectroscopic techniques proved that the incorporated ion was more absorbing in the near infrared region as intended, and was not radiatively remitting absorbed photons. However, exact band gap measurements were not able to be achieved due to the limitations of the detector.

Thermal analyses also confirmed the presence of water within the structure with increasing ion concentration and heated XRD results provided information as to how the materials might behave at high temperature.

Ablation threshold experiments were then performed in order to obtain an energy maxima for the proceeding experiments and found the ablation thresholds as 0.647±0.052, 0.628±0.050, 0.583±0.047, 0.611±0.049 and 0.571±0.046 J/cm^2 , for 0%, 5%, 10%, 20% and 30% Fe^{3+} doped hydroxyapatite respectively. This is in agreement with the literature for hydroxyapatite in this regime. No correlation was found between these thresholds and doping concentration, confirming the presence of a UV band edge outside the limitations of the integrating sphere detector. Mutli-pulse ablation thresholds

also trended as expected given the material and the thresholds measure of the substrates were within a degree of accuracy of previously reported values.

Low repetition rate experiments provided no success in modifying the material outside of ablation. This is due to the long relative time between pulses where the diffusivity of any absorbed energy is faster than the pulse train. It was suggested that an increase in repetition rate, might allow for increased thermal accumulation and there for material modification.

Low repetition rate experiments onto Ti-6Al-4V substrates, utilising the methods reported by Symietz et al. [83], proved successful in coating the substrate with some particulates at least. Repeating the method twice more allowed for some parts of the substrate surface to be covered adequately.

Moderate repetition rate laser source of 500 kHz, was then tested with the synthesised materials, and shown to have a strong interaction, often unpredictably, disallowing any correlative measurements of energy minima. However, processing of the materials with the same parameters generated quite radical morphological and structural change in the materials. A black colour was produced post processing of the materials, which also caused issues in trying to consider total absorbed energy, and was determined to be due to ejection of iron oxide phases during the rapid heating/cooling process. In comparison to the heated XRD samples, this procedure showed differing results, which could have utility in applications elsewhere. Unfortunately, further study with this system could no longer resume as access to the laser was compromised.

Finally, high repetition rate trials were accomplished with a non-commercial laser source with low average power but extremely high repetition rate. This

allowed for more controlled heating of the substrates, whilst creating some odd patterning in the material surface. This was concluded to be due to structural water movement between the crystals during the short irradiation time. The materials were found to have been modified more modestly, but within the expected results given the conventionally heated results.

Processing of coatings on Ti-6Al-4V and enamel substrates proved successful in modifying the coating material, however, poor wetting of the condensed coating material cause an issue, making the particulates ball up with high surface tension.

Whilst processing some of the enamel substrates when attempting to perform a sintering layer, it was found that this laser, with the instigation of heat, defects or other ignition points, could quite easily destroy the surface of the enamel, either through decomposition of the organic parts of the enamel or the hydroxyapatite itself. This along with the resultant product being black, is unlikely to make this method or any of the methods explored in these experiments attractive to a dentist or health professional who might be looking for new ways to solve the hypersensitivity problem.

The efficacy of adhesion to the substrates with these systems and methods was not able to be proved easily. Solely heating of the coating layer does not appear to be adequate despite generating material and crystal growth in small localities. In this regard also, the use of a femtosecond laser is fairly redundant as the extremely small pulse duration does not allow for easy deposition of energy and thermal accumulation. This would be a large factor when considering the cost of the overall for a system of this kind, where cheap

picosecond fibre sources are dominating the laser marketplace, and would provide an adequate source for heating a material.

8.1 Future work

Future work to be considered around the studies presented in this thesis would be:

1. Utilise the results of Symeitz et al. to make a wetable surface for processing further with another laser source. This would allow for the material to be adhered to the substrate in the first instance, and then sinter further material onto this material may present a solution in the titanium substrate case
2. Experiments with high peak powers at around 500 kHz. Integrating the use of modifying the titanium substrates and being able to adequately sinter the material through thermal accumulation
3. Longer pulse duration studies in order to have more control over thermal accumulation deposition.
4. A different absorbing ion than iron into the hydroxyapatite structure that doesn't turn black post irradiation

References

[1] S. Kurtz, K. Ong, E. Lau, F. Mowat, and M. Halpern, "Projections of primary and revision hip and knee arthroplasty in the United States from 2005 to 2030," *J. Bone Joint Surg. Am.*, vol. 89, no. 4, pp. 780–785, Apr. 2007.

[2] N. N. Mahomed, J. A. Barrett, J. N. Katz, C. B. Phillips, E. Losina, R. A. Lew, E. Guadagnoli, W. H. Harris, R. Poss, and J. A. Baron, "Rates and outcomes of primary and revision total hip replacement in the United States medicare population," *J. Bone Joint Surg. Am.*, vol. 85-A, no. 1, pp. 27–32, Jan. 2003.

[3] I. D. Learmonth, C. Young, and C. Rorabeck, "The operation of the century: total hip replacement," *The Lancet*, vol. 370, no. 9597, pp. 1508–1519, Oct. 2007.

[4] E. Losina, J. Barrett, N. N. Mahomed, J. A. Baron, and J. N. Katz, "Early failures of total hip replacement: Effect of surgeon volume," *Arthritis Rheum.*, vol. 50, no. 4, pp. 1338–1343, Apr. 2004.

[5] G. A. Brown, K. Firoozbakhsh, T. A. Decoster, J. R. J. Reyna, and M. Moneim, "RAPID PROTOTYPING: THE FUTURE OF TRAUMA SURGERY?," *JBJS*, vol. 85, p. 49, 2003.

[6] P. L. Jacobsen and G. Bruce, "Clinical dentin hypersensitivity: understanding the causes and prescribing a treatment.," *J. Contemp. Dent. Pract.*, vol. 2, no. 1, pp. 1–12, Feb. 2001.

[7] P. Bartold, "Dentinal hypersensitivity: a review," *Aust. Dent. J.*, vol. 51, no. 3, pp. 212–218, Sep. 2006.

[8] R. G. Craig, D. Welker, J. Rothaut, K. G. Krumbholz, K.-P. Stefan, K. Dermann, H.-J. Rehberg, G. Franz, K. M. Lehmann, and M. Borchert, "Dental Materials," in *Ullmann's Encyclopedia of Industrial Chemistry*, American Cancer Society, 2006.

[9] R. A. White, J. N. Weber, and E. W. White, "Replamineform: A New Process for Preparing Porous Ceramic, Metal, and Polymer Prosthetic Materials," *Science*, vol. 176, no. 4037, pp. 922–924, May 1972.

[10] M. L. Wang, P. F. Sharkey, and R. S. Tuan, "Particle bioreactivity and wear-mediated osteolysis," *J. Arthroplasty*, vol. 19, no. 8, pp. 1028–1038, Dec. 2004.

[11] W. Cao and L. L. Hench, "Bioactive materials," *Ceram. Int.*, vol. 22, no. 6, pp. 493–507, Jan. 1996.

[12] M. Niemz, *Laser-Tissue Interactions: Fundamentals and Applications*, 3rd ed. Berlin Heidelberg: Springer-Verlag, 2007.

[13] Z. Amjad, Ed., *Calcium Phosphates in Biological and Industrial Systems*. Springer US, 1998.

[14] K. de Groot, J. G. Wolke, and J. A. Jansen, "Calcium phosphate coatings for medical implants," *Proc. Inst. Mech. Eng. [H]*, vol. 212, no. 2, pp. 137–147, 1998.

[15] M. Vallet-Regí and J. M. González-Calbet, "Calcium phosphates as substitution of bone tissues," *Prog. Solid State Chem.*, vol. 32, no. 1, pp. 1–31, Jan. 2004.

[16] F. C. M. Driessens, *Formation and Stability of Calcium Phosphates in Relation to the Phase Composition of the Mineral in Calcified Tissues* |

Bioceramics Calcium Phosphate | Taylor & Francis Group. Taylor Francis, 1983.

[17] C. P. a. T. Klein, A. A. Driessen, K. de Groot, and A. van den Hooff, "Biodegradation behavior of various calcium phosphate materials in bone tissue," *J. Biomed. Mater. Res.*, vol. 17, no. 5, pp. 769–784, Sep. 2004.

[18] C. A. van Blitterswijk, J. J. Grote, H. K. Koerten, and W. Kuijpers, "The biological performance of calcium phosphate ceramics in an infected implantation site. III: Biological performance of beta-whitlockite in the noninfected and infected rat middle ear," *J. Biomed. Mater. Res.*, vol. 20, no. 8, pp. 1197–1217, Oct. 1986.

[19] C. A. van Blitterswijk, S. C. Hesseling, J. J. Grote, H. K. Koerten, and K. de Groot, "The biocompatibility of hydroxyapatite ceramic: a study of retrieved human middle ear implants," *J. Biomed. Mater. Res.*, vol. 24, no. 4, pp. 433–453, Apr. 1990.

[20] J. A. Jansen, J. P. van der Waerden, H. B. van der Lubbe, and K. de Groot, "Tissue response to percutaneous implants in rabbits," *J. Biomed. Mater. Res.*, vol. 24, no. 3, pp. 295–307, Mar. 1990.

[21] J. A. Jansen, J. R. de Wijn, J. M. Wolters-Lutgerhorst, and P. J. van Mullem, "Ultrastructural study of epithelial cell attachment to implant materials," *J. Dent. Res.*, vol. 64, no. 6, pp. 891–896, Jun. 1985.

[22] C. A. van Blitterswijk, J. J. Grote, W. Kuÿpers, C. J. Blok-van Hoek, and W. T. Daems, "Bioreactions at the tissue/hydroxyapatite interface," *Biomaterials*, vol. 6, no. 4, pp. 243–251, Jul. 1985.

[23] H. W. Denissen and K. de Groot, "Immediate dental root implants from synthetic dense calcium hydroxylapatite," *J. Prosthet. Dent.*, vol. 42, no. 5, pp. 551–556, Nov. 1979.

[24] E. C. Moreno and R. T. Zahradnik, "Chemistry of enamel subsurface demineralization in vitro," *J. Dent. Res.*, vol. 53, no. 2, pp. 226–235, Apr. 1974.

[25] P. R. Patel and W. E. Brown, "Thermodynamic Solubility Product of Human Tooth Enamel: Powdered Sample," *J. Dent. Res.*, vol. 54, no. 4, pp. 728–736, Jul. 1975.

[26] W. E. Brown, "Solubilities of phosphates and other sparingly soluble compounds," *Environ. Phosphorus Handb.*, pp. 203–239, 1973.

[27] M. Corno, R. Orlando, B. Civalleri, and P. Ugliengo, "Periodic B3LYP study of hydroxyapatite (001) surface modelled by thin layer slabs," *Eur. J. Mineral.*, vol. 19, no. 5, pp. 757–767, Oct. 2007.

[28] A. Dosen and R. F. Giese, "Thermal decomposition of brushite, CaHPO4·2H2O to monetite CaHPO4 and the formation of an amorphous phase," *Am. Mineral.*, vol. 96, no. 2–3, pp. 368–373, Feb. 2011.

[29] R. Z. LeGeros, "Calcium phosphate materials in restorative dentistry: a review," *Adv. Dent. Res.*, vol. 2, no. 1, pp. 164–180, Aug. 1988.

[30] A. J. Ambard and L. Mueninghoff, "Calcium phosphate cement: review of mechanical and biological properties," *J. Prosthodont. Off. J. Am. Coll. Prosthodont.*, vol. 15, no. 5, pp. 321–328, Oct. 2006.

[31] M. Bohner, U. Gbureck, and J. E. Barralet, "Technological issues for the development of more efficient calcium phosphate bone cements: A critical assessment," *Biomaterials*, vol. 26, no. 33, pp. 6423–6429, Nov. 2005.

[32] A. Boger, M. Bohner, P. Heini, S. Verrier, and E. Schneider, “Properties of an injectable low modulus PMMA bone cement for osteoporotic bone,” *J. Biomed. Mater. Res. B Appl. Biomater.*, vol. 86, no. 2, pp. 474–482, Aug. 2008.

[33] A. Reinstorf, M. Ruhnow, M. Gelinsky, W. Pompe, U. Hempel, K. W. Wenzel, and P. Simon, “Phosphoserine--a convenient compound for modification of calcium phosphate bone cement collagen composites,” *J. Mater. Sci. Mater. Med.*, vol. 15, no. 4, pp. 451–455, Apr. 2004.

[34] Y. Miyamoto, K. Ishikawa, M. Takechi, T. Toh, T. Yuasa, M. Nagayama, and K. Suzuki, “Basic properties of calcium phosphate cement containing atelocollagen in its liquid or powder phases,” *Biomaterials*, vol. 19, no. 7–9, pp. 707–715, May 1998.

[35] M. Jarcho, “Biomaterial aspects of calcium phosphates. Properties and applications.,” *Dent. Clin. North Am.*, vol. 30, no. 1, pp. 25–47, Jan. 1986.

[36] J. G. C. Wolke, J. M. A. de Blieck-Hogervorst, W. J. A. Dhert, C. P. a. T. Klein, and K. de Groot, “Studies on the thermal spraying of apatite bioceramics,” *J. Therm. Spray Technol.*, vol. 1, no. 1, pp. 75–82, Mar. 1992.

[37] S. D. Cook, K. A. Thomas, J. F. Kay, and M. Jarcho, “Hydroxyapatite-coated titanium for orthopedic implant applications,” *Clin. Orthop.*, no. 232, pp. 225–243, Jul. 1988.

[38] J. Disam, K. Luebbers, U. Neudert, and A. Sickinger, “Effect of LPPS spray parameters on the structure of ceramic coatings,” *J. Therm. Spray Technol.*, vol. 3, no. 2, pp. 142–147, Jun. 1994.

[39] Y. C. Tsui, C. Doyle, and T. W. Clyne, “Plasma sprayed hydroxyapatite coatings on titanium substrates Part 1: Mechanical properties and residual stress levels,” *Biomaterials*, vol. 19, no. 22, pp. 2015–2029, Nov. 1998.

[40] H. Oguchi, K. Ishikawa, S. Ojima, Y. Hirayama, K. Seto, and G. Eguchi, “Evaluation of a high-velocity flame-spraying technique for hydroxyapatite,” *Biomaterials*, vol. 13, no. 7, pp. 471–477, Jan. 1992.

[41] P. Ducheyne, W. Van Raemdonck, J. C. Heughebaert, and M. Heughebaert, “Structural analysis of hydroxyapatite coatings on titanium,” *Biomaterials*, vol. 7, no. 2, pp. 97–103, Mar. 1986.

[42] P. Ducheyne, S. Radin, M. Heughebaert, and J. C. Heughebaert, “Calcium phosphate ceramic coatings on porous titanium: effect of structure and composition on electrophoretic deposition, vacuum sintering and in vitro dissolution,” *Biomaterials*, vol. 11, no. 4, pp. 244–254, May 1990.

[43] P. Ducheyne, L. L. Hench, A. Kagan, M. Martens, A. Bursens, and J. C. Mulier, “Effect of hydroxyapatite impregnation on skeletal bonding of porous coated implants,” *J. Biomed. Mater. Res.*, vol. 14, no. 3, pp. 225–237.

[44] M. Shirkhanzadeh, “Electrochemical fabrication of bioactive composite coatings on Ti6A14V surgical alloy,” *Mater. Lett.*, vol. 14, no. 1, pp. 27–30, Jun. 1992.

[45] S. Ban, S. Maruno, N. Arimoto, A. Harada, and J. Hasegawa, “Effect of electrochemically deposited apatite coating on bonding of bone to the HA-G-Ti composite and titanium,” *J. Biomed. Mater. Res.*, vol. 36, no. 1, pp. 9–15.

[46] J. G. C. Wolke, K. van Dijk, H. G. Schaeken, K. de Groot, and J. A. Jansen, "Study of the surface characteristics of magnetron-sputter calcium phosphate coatings," *J. Biomed. Mater. Res.*, vol. 28, no. 12, pp. 1477–1484.

[47] J. A. Jansen, J. G. C. Wolke, S. Swann, J. P. C. M. V. D. Waerden, and K. D. Groof, "Application of magnetron sputtering for producing ceramic coatings on implant materials," *Clin. Oral Implants Res.*, vol. 4, no. 1, pp. 28–34.

[48] C. M. Cotell, D. B. Chrisey, K. S. Grabowski, J. A. Sprague, and C. R. Gossett, "Pulsed laser deposition of hydroxylapatite thin films on Ti-6Al-4V," *J. Appl. Biomater.*, vol. 3, no. 2, pp. 87–93.

[49] L. Zheng, F. Yang, H. Shen, X. Hu, C. Mochizuki, M. Sato, S. Wang, and Y. Zhang, "The effect of composition of calcium phosphate composite scaffolds on the formation of tooth tissue from human dental pulp stem cells," *Biomaterials*, vol. 32, no. 29, pp. 7053–7059, Oct. 2011.

[50] H. H. K. Xu, S. Takagi, J. B. Quinn, and L. C. Chow, "Fast-setting calcium phosphate scaffolds with tailored macropore formation rates for bone regeneration," *J. Biomed. Mater. Res. A*, vol. 68A, no. 4, pp. 725–734.

[51] F. P. Knudsen, "Dependence of Mechanical Strength of Brittle Polycrystalline Specimens on Porosity and Grain Size," *J. Am. Ceram. Soc.*, vol. 42, no. 8, pp. 376–387.

[52] M. Akao, H. Aoki, and K. Kato, "Mechanical properties of sintered hydroxyapatite for prosthetic applications," *J. Mater. Sci.*, vol. 16, no. 3, pp. 809–812, Mar. 1981.

[53] W. R. Rao and R. F. Boehm, "A Study of Sintered Apatites," *J. Dent. Res.*, vol. 53, no. 6, pp. 1351–1354, Nov. 1974.

[54] R. Z. LeGeros, S. Lin, R. Rohanizadeh, D. Mijares, and J. P. LeGeros, "Biphasic calcium phosphate bioceramics: preparation, properties and applications," *J. Mater. Sci. Mater. Med.*, vol. 14, no. 3, pp. 201–209, Mar. 2003.

[55] A. J. Ruys, M. Wei, C. C. Sorrell, M. R. Dickson, A. Brandwood, and B. K. Milthorpe, "Sintering effects on the strength of hydroxyapatite," *Biomaterials*, vol. 16, no. 5, pp. 409–415, Jan. 1995.

[56] G. Muralithran and S. Ramesh, "The effects of sintering temperature on the properties of hydroxyapatite," *Ceram. Int.*, vol. 26, no. 2, pp. 221–230, Mar. 2000.

[57] A. Chanda, S. Dasgupta, S. Bose, and A. Bandyopadhyay, "Microwave sintering of calcium phosphate ceramics," *Mater. Sci. Eng. C*, vol. 29, no. 4, pp. 1144–1149, May 2009.

[58] D. Veljović, I. Zalite, E. Palcevskis, I. Smiciklas, R. Petrović, and D. Janaćković, "Microwave sintering of fine grained HAP and HAP/TCP bioceramics," *Ceram. Int.*, vol. 36, no. 2, pp. 595–603, Mar. 2010.

[59] R. Comesaña, F. Lusquiños, J. del Val, T. Malot, M. López-Álvarez, A. Riveiro, F. Quintero, M. Boutinguiza, P. Aubry, A. De Carlos, and J. Pou, "Calcium phosphate grafts produced by rapid prototyping based on laser cladding," *J. Eur. Ceram. Soc.*, vol. 31, no. 1, pp. 29–41, Jan. 2011.

[60] C. Shuai, P. Li, J. Liu, and S. Peng, "Optimization of TCP/HAP ratio for better properties of calcium phosphate scaffold via selective laser sintering," *Mater. Charact.*, vol. 77, pp. 23–31, Mar. 2013.

[61] Y. Khan, M. J. Yaszemski, A. G. Mikos, and C. T. Laurencin, “Tissue Engineering of Bone: Material and Matrix Considerations,” *JBJS*, vol. 90, p. 36, Feb. 2008.

[62] C. K. Chua, K. F. Leong, K. H. Tan, F. E. Wiria, and C. M. Cheah, “Development of tissue scaffolds using selective laser sintering of polyvinyl alcohol/hydroxyapatite biocomposite for craniofacial and joint defects,” *J. Mater. Sci. Mater. Med.*, vol. 15, no. 10, pp. 1113–1121, Oct. 2004.

[63] R. L. Simpson, F. E. Wiria, A. A. Amis, C. K. Chua, K. F. Leong, U. N. Hansen, M. Chandrasekaran, and M. W. Lee, “Development of a 95/5 poly(L-lactide-co-glycolide)/hydroxylapatite and β-tricalcium phosphate scaffold as bone replacement material via selective laser sintering,” *J. Biomed. Mater. Res. B Appl. Biomater.*, vol. 84B, no. 1, pp. 17–25.

[64] K. H. Tan, C. K. Chua, K. F. Leong, C. M. Cheah, W. S. Gui, W. S. Tan, and F. E. Wiria, “Selective laser sintering of biocompatible polymers for applications in tissue engineering,” *Biomed. Mater. Eng.*, vol. 15, no. 1,2, pp. 113–124, Jan. 2005.

[65] M. L. Walter, M. E. Domes, R. A. Diller, J. Sproedt, and U. H. Joosten, “Photoablation of bone by excimer laser radiation,” *Lasers Surg. Med.*, vol. 25, no. 2, pp. 153–158.

[66] N. M. Fried and D. Fried, “Comparison of Er:YAG and 9.6-μm TE CO2 lasers for ablation of skull tissue,” *Lasers Surg. Med.*, vol. 28, no. 4, pp. 335–343.

[67] M. Frentzen, W. Götz, M. Ivanenko, S. Afilal, M. Werner, and P. Hering, “Osteotomy with 80-μs CO<Subscript>2</Subscript> laser pulses – histological results,” *Lasers Med. Sci.*, vol. 18, no. 2, pp. 119–124, May 2003.

[68] M. Abu-Serriah, H. Critchlow, C. J. Whitters, and A. Ayoub, “Removal of partially erupted third molars using an Erbium (Er):YAG laser: a randomised controlled clinical trial,” *Br. J. Oral Maxillofac. Surg.*, vol. 42, no. 3, pp. 203–208, Jun. 2004.

[69] K.-U. Lewandrowski, C. Lorente, K. T. Schomacker, T. J. Fiotte, J. W. Wilkes, and T. F. Deutsch, “Use of the Er:YAG laser for improved plating in maxillofacial surgery: Comparison of bone healing in laser and drill osteotomies,” *Lasers Surg. Med.*, vol. 19, no. 1, pp. 40–45.

[70] K. Glockner, J. Rumpler, K. Ebeleseder, and P. Städtler, “Intrapulpal Temperature during Preparation with the Er:YAG Laser Compared to the Conventional Burr: An in Vitro Study,” *J. Clin. Laser Med. Surg.*, vol. 16, no. 3, pp. 153–157, Jun. 1998.

[71] S. Alves, V. Oliveira, and R. Vilar, “Femtosecond laser ablation of dentin,” *J. Phys. Appl. Phys.*, vol. 45, no. 24, p. 245401, 2012.

[72] Y. Liu and M. Niemz, “Ablation of femural bone with femtosecond laser pulses—a feasibility study,” *Lasers Med. Sci.*, vol. 22, no. 3, pp. 171–174, Sep. 2007.

[73] B. Girard, D. Yu, M. R. Armstrong, B. C. Wilson, C. M. L. Clokie, and R. J. D. Miller, “Effects of femtosecond laser irradiation on osseous tissues,” *Lasers Surg. Med.*, vol. 39, no. 3, pp. 273–285.

[74] B.-M. Kim, M. D. Feit, A. M. Rubenchik, B. M. Mammini, and L. B. Da Silva, “Optical feedback signal for ultrashort laser pulse ablation of

tissue1Work performed at Lawrence Livermore National Laboratory under the auspices of the US Department of Energy under contract No. W-7405-ENG-48.1," *Appl. Surf. Sci.*, vol. 127–129, pp. 857–862, May 1998.

[75] R. F. Z. Lizarelli, M. M. Costa, E. Carvalho-Filho, F. D. Nunes, and V. S. Bagnato, "Selective ablation of dental enamel and dentin using femtosecond laser pulses," *Laser Phys. Lett.*, vol. 5, no. 1, p. 63, Sep. 2007.

[76] J. Krüger, W. Kautek, and H. Newesely, "Femtosecond-pulse laser ablation of dental hydroxyapatite and single-crystalline fluoroapatite," *Appl. Phys. A*, vol. 69, no. 1, pp. S403–S407, Dec. 1999.

[77] A. Y. Vorobyev and C. Guo, "Femtosecond laser surface structuring technique for making human enamel and dentin surfaces superwetting," *Appl. Phys. B*, vol. 113, no. 3, pp. 423–428, Dec. 2013.

[78] A. S. Kabas, T. Ersoy, M. Gülsoy, and S. Akturk, "Femtosecond laser etching of dental enamel for bracket bonding," *J. Biomed. Opt.*, vol. 18, no. 9, p. 098003, Sep. 2013.

[79] R. H. Stern, J. Vahl, and R. F. Sognnaes, "Lased Enamel: Ultrastructural Observations of Pulsed Carbon Dioxide Laser Effects," *J. Dent. Res.*, vol. 51, no. 2, pp. 455–460, Mar. 1972.

[80] D. G. A. Nelson, M. Shariati, R. Glena, C. P. Shields, and J. D. B. Featherstone, "Effect of Pulsed Low Energy Infrared Laser Irradiation on Artificial Caries-Like Lesion Formation," *Caries Res.*, vol. 20, no. 4, pp. 289–299, 1986.

[81] H. Yamamoto and K. Ooya, "Potential of yttrium-aluminum-garnet laser in caries prevention," *J. Oral Pathol. Med.*, vol. 3, no. 1, pp. 7–15.

[82] T. Oho and T. Morioka, "A Possible Mechanism of Acquired Acid Resistance of Human Dental Enamel by Laser Irradiation," *Caries Res.*, vol. 24, no. 2, pp. 86–92, 1990.

[83] C. Symietz, E. Lehmann, R. Gildenhaar, R. Koter, G. Berger, and J. Krüger, "Fixation of bioactive calcium alkali phosphate on Ti6Al4V implant material with femtosecond laser pulses," *Appl. Surf. Sci.*, vol. 257, no. 12, pp. 5208–5212, Apr. 2011.

[84] S. R. Paital and N. B. Dahotre, "Laser surface treatment for porous and textured Ca–P bio-ceramic coating on Ti–6Al–4V," *Biomed. Mater.*, vol. 2, no. 4, p. 274, 2007.

[85] S. R. Paital, K. Balani, A. Agarwal, and N. B. Dahotre, "Fabrication and evaluation of a pulse laser-induced Ca–P coating on a Ti alloy for bioapplication," *Biomed. Mater.*, vol. 4, no. 1, p. 015009, 2009.

[86] E. Elmadani, A. Jha, T. Perali, C. Jappy, D. Walsh, C. Leburn, T. Brown, W. Sibbett, M. Duggal, and J. Toumba, "Characterization of Rare-Earth Oxide Photoactivated Calcium Phosphate Minerals for Resurfacing Teeth," *J. Am. Ceram. Soc.*, vol. 95, no. 9, pp. 2716–2724.

[87] A. D. Anastasiou, S. Strafford, O. Posada-Estefan, C. L. Thomson, S. A. Hussain, T. J. Edwards, M. Malinowski, N. Hondow, N. K. Metzger, C. T. A. Brown, M. N. Routledge, A. P. Brown, M. S. Duggal, and A. Jha, "β-pyrophosphate: A potential biomaterial for dental applications," *Mater. Sci. Eng. C*, vol. 75, pp. 885–894, Jun. 2017.

[88] A. D. Anastasiou, S. Strafford, C. L. Thomson, J. Gardy, T. J. Edwards, M. Malinowski, S. A. Hussain, N. K. Metzger, A. Hassanpour, C. T. A. Brown, A. P. Brown, M. S. Duggal, and A. Jha, "Exogenous mineralization of hard

tissues using photo-absorptive minerals and femto-second lasers; the case of dental enamel," *Acta Biomater.*, vol. 71, pp. 86–95, Apr. 2018.

[89] L. D. Landau, J. S. Bell, M. J. Kearsley, L. P. Pitaevskii, E. M. Lifshitz, and J. B. Sykes, *Electrodynamics of Continuous Media*. Elsevier, 2013.

[90] E. G. Gamaly, A. V. Rode, B. Luther-Davies, and V. T. Tikhonchuk, "Ablation of solids by femtosecond lasers: Ablation mechanism and ablation thresholds for metals and dielectrics," *Phys. Plasmas*, vol. 9, no. 3, pp. 949–957, Feb. 2002.

[91] P. P. Pronko, S. K. Dutta, J. Squier, J. V. Rudd, D. Du, and G. Mourou, "Machining of sub-micron holes using a femtosecond laser at 800 nm," *Opt. Commun.*, vol. 114, no. 1, pp. 106–110, Jan. 1995.

[92] P. Simon and J. Ihlemann, "Machining of submicron structures on metals and semiconductors by ultrashort UV-laser pulses," *Appl. Phys. A*, vol. 63, no. 5, pp. 505–508, Nov. 1996.

[93] P. T. Mannion, J. Magee, E. Coyne, G. M. O'Connor, and T. J. Glynn, "The effect of damage accumulation behaviour on ablation thresholds and damage morphology in ultrafast laser micro-machining of common metals in air," *Appl. Surf. Sci.*, vol. 233, no. 1, pp. 275–287, Jun. 2004.

[94] B. N. Chichkov, C. Momma, S. Nolte, F. von Alvensleben, and A. Tünnermann, "Femtosecond, picosecond and nanosecond laser ablation of solids," *Appl. Phys. A*, vol. 63, no. 2, pp. 109–115, Aug. 1996.

[95] G. Kamlage, T. Bauer, A. Ostendorf, and B. N. Chichkov, "Deep drilling of metals by femtosecond laser pulses," *Appl. Phys. A*, vol. 77, no. 2, pp. 307–310, Jul. 2003.

[96] J. Kim and S. Na, "Metal thin film ablation with femtosecond pulsed laser," *Opt. Laser Technol.*, vol. 39, no. 7, pp. 1443–1448, Oct. 2007.

[97] A. Borowiec and H. K. Haugen, "Femtosecond laser micromachining of grooves in indium phosphide," *Appl. Phys. A*, vol. 79, no. 3, pp. 521–529, Aug. 2004.

[98] N. Bärsch, K. Körber, A. Ostendorf, and K. H. Tönshoff, "Ablation and cutting of planar silicon devices using femtosecond laser pulses," *Appl. Phys. A*, vol. 77, no. 2, pp. 237–242, Jul. 2003.

[99] P. Simon and J. Ihlemann, "Ablation of submicron structures on metals and semiconductors by femtosecond UV-laser pulses," *Appl. Surf. Sci.*, vol. 109–110, pp. 25–29, Feb. 1997.

[100] M. D. Perry, B. C. Stuart, P. S. Banks, M. D. Feit, V. Yanovsky, and A. M. Rubenchik, "Ultrashort-pulse laser machining of dielectric materials," *J. Appl. Phys.*, vol. 85, no. 9, pp. 6803–6810, Apr. 1999.

[101] S. Guizard, A. Semerok, J. Gaudin, M. Hashida, P. Martin, and F. Quéré, "Femtosecond laser ablation of transparent dielectrics: measurement and modelisation of crater profiles," *Appl. Surf. Sci.*, vol. 186, no. 1, pp. 364–368, Jan. 2002.

[102] M. Lenzner, J. Krüger, W. Kautek, and F. Krausz, "Precision laser ablation of dielectrics in the 10-fs regime," *Appl. Phys. A*, vol. 68, no. 3, pp. 369–371, Mar. 1999.

[103] M. Lenzner, "Femtosecond laser-induced damage of dielectrics," *Int. J. Mod. Phys. B*, vol. 13, no. 13, pp. 1559–1578, May 1999.

[104] J. Krüger and W. Kautek, "Ultrashort Pulse Laser Interaction with Dielectrics and Polymers," in *Polymers and Light*, Springer, Berlin, Heidelberg, pp. 247–290.
[105] R. R. Gattass and E. Mazur, "Femtosecond laser micromachining in transparent materials," *Nat. Photonics*, vol. 2, no. 4, pp. 219–225, Apr. 2008.
[106] K. M. Davis, K. Miura, N. Sugimoto, and K. Hirao, "Writing waveguides in glass with a femtosecond laser," *Opt. Lett.*, vol. 21, no. 21, pp. 1729–1731, Nov. 1996.
[107] A. van Brakel, C. Grivas, M. N. Petrovich, and D. J. Richardson, "Micro-channels machined in microstructured optical fibers by femtosecond laser," *Opt. Express*, vol. 15, no. 14, pp. 8731–8736, Jul. 2007.
[108] D. N. Vitek, D. E. Adams, A. Johnson, P. S. Tsai, S. Backus, C. G. Durfee, D. Kleinfeld, and J. A. Squier, "Temporally focused femtosecond laser pulses for low numerical aperture micromachining through optically transparent materials," *Opt. Express*, vol. 18, no. 17, pp. 18086–18094, Aug. 2010.
[109] C. B. Schaffer, A. Brodeur, J. F. García, and E. Mazur, "Micromachining bulk glass by use of femtosecond laser pulses with nanojoule energy," *Opt. Lett.*, vol. 26, no. 2, pp. 93–95, Jan. 2001.
[110] R. R. Gattass, L. R. Cerami, and E. Mazur, "Micromachining of bulk glass with bursts of femtosecond laser pulses at variable repetition rates," *Opt. Express*, vol. 14, no. 12, pp. 5279–5284, Jun. 2006.
[111] S. R. Paital, W. He, C. Daniel, and N. B. Dahotre, "Laser process effects on physical texture and wetting in implantable Ti-alloys," *JOM*, vol. 62, no. 6, pp. 76–83, Jun. 2010.
[112] S. Sakabe, M. Hashida, S. Tokita, S. Namba, and K. Okamuro, "Mechanism for self-formation of periodic grating structures on a metal surface by a femtosecond laser pulse," *Phys. Rev. B*, vol. 79, no. 3, p. 033409, Jan. 2009.
[113] Y. Yang, J. Yang, L. Xue, and Y. Guo, "Surface patterning on periodicity of femtosecond laser-induced ripples," *Appl. Phys. Lett.*, vol. 97, no. 14, p. 141101, Oct. 2010.
[114] B. K. Nayak, M. C. Gupta, and K. W. Kolasinski, "Formation of nano-textured conical microstructures in titanium metal surface by femtosecond laser irradiation," *Appl. Phys. A*, vol. 90, no. 3, pp. 399–402, Mar. 2008.
[115] N. G. Semaltianos, W. Perrie, P. French, M. Sharp, G. Dearden, and K. G. Watkins, "Femtosecond laser surface texturing of a nickel-based superalloy," *Appl. Surf. Sci.*, vol. 255, no. 5, Part 2, pp. 2796–2802, Dec. 2008.
[116] X. C. Wang, H. Y. Zheng, C. W. Tan, F. Wang, H. Y. Yu, and K. L. Pey, "Femtosecond laser induced surface nanostructuring and simultaneous crystallization of amorphous thin silicon film," *Opt. Express*, vol. 18, no. 18, pp. 19379–19385, Aug. 2010.
[117] Z. Li, B. K. Nayak, V. V. Iyengar, D. McIntosh, Q. Zhou, M. C. Gupta, and J. C. Campbell, "Laser-textured silicon photodiode with broadband spectral response," *Appl. Opt.*, vol. 50, no. 17, pp. 2508–2511, Jun. 2011.

[118] X. Wang, F. Chen, H. Liu, W. Liang, Q. Yang, J. Si, and X. Hou, "Femtosecond laser-induced mesoporous structures on silicon surface," *Opt. Commun.*, vol. 284, no. 1, pp. 317–321, Jan. 2011.
[119] S. K. Sundaram and E. Mazur, "Inducing and probing non-thermal transitions in semiconductors using femtosecond laser pulses," *Nat. Mater.*, vol. 1, no. 4, pp. 217–224, Dec. 2002.
[120] J. Meijer, "Laser beam machining (LBM), state of the art and new opportunities," *J. Mater. Process. Technol.*, vol. 149, no. 1, pp. 2–17, Jun. 2004.
[121] H. Huang, L.-M. Yang, S. Bai, and J. Liu, "Femtosecond fiber laser welding of dissimilar metals," *Appl. Opt.*, vol. 53, no. 28, pp. 6569–6578, Oct. 2014.
[122] A. Hu, P. Peng, H. Alarifi, X. Y. Zhang, J. Y. Guo, Y. Zhou, and W. W. Duley, "Femtosecond laser welded nanostructures and plasmonic devices," *J. Laser Appl.*, vol. 24, no. 4, p. 042001, Jul. 2012.
[123] A. Ben-Yakar, A. Harkin, J. Ashmore, R. L. Byer, and H. A. Stone, "Thermal and fluid processes of a thin melt zone during femtosecond laser ablation of glass: the formation of rims by single laser pulses," *J. Phys. Appl. Phys.*, vol. 40, no. 5, p. 1447, 2007.
[124] T. Tamaki, W. Watanabe, J. Nishii, and K. Itoh, "Welding of Transparent Materials Using Femtosecond Laser Pulses," *Jpn. J. Appl. Phys.*, vol. 44, no. 5L, p. L687, May 2005.
[125] I. Miyamoto, "Fusion Welding of Glass Using Femtosecond Laser Pulses with High-repetition Rates," *J. Laser MicroNanoengineering*, vol. 2, no. 1, pp. 57–63, Mar. 2007.
[126] S. Richter, S. Döring, A. Tünnermann, and S. Nolte, "Bonding of glass with femtosecond laser pulses at high repetition rates," *Appl. Phys. A*, vol. 103, no. 2, pp. 257–261, May 2011.
[127] Y. Ozeki, T. Inoue, T. Tamaki, H. Yamaguchi, S. Onda, W. Watanabe, T. Sano, S. Nishiuchi, A. Hirose, and K. Itoh, "Direct Welding between Copper and Glass Substrates with Femtosecond Laser Pulses," *Appl. Phys. Express*, vol. 1, no. 8, p. 082601, Aug. 2008.
[128] I. Miyamoto, "Welding of glass/glass and Si/glass using ultrashort laser pulses," in *2013 Conference on Lasers and Electro-Optics - International Quantum Electronics Conference (2013), paper CM_3LIM_1*, 2013, p. CM_3LIM_1.
[129] Y. Son, T. W. Lim, J. Yeo, S. H. Ko, and D.-Y. Yang, "Fabrication of Nano-scale Conductors by Selective Femtosecond Laser Sintering of Metal Nanoparticles," in *10th IEEE International Conference on Nanotechnology*, 2010, pp. 390–393.
[130] Y. Son, J. Yeo, C. W. Ha, S. Hong, S. H. Ko, and D.-Y. Yang, "Fabrication of submicron-sized metal patterns on a flexible polymer substrate by femtosecond laser sintering of metal nanoparticles," *Int. J. Nanomanufacturing*, vol. 9, no. 5–6, pp. 468–476, Jan. 2013.
[131] C. W. Cheng and J. K. Chen, "Femtosecond laser sintering of copper nanoparticles," *Appl. Phys. A*, vol. 122, no. 4, p. 289, Apr. 2016.
[132] C. J. Huang, H. T. Cheng, C. N. Kuo, C. W. Cheng, W. L. Tsai, and Y. H. Yang, "Fabrication of porous Ti surface by femtosecond laser sintering of Ti powder," in *2012 Conference on Lasers and Electro-Optics (CLEO)*, 2012, pp. 1–2.

[133] T. Watson, I. Mabbett, H. Wang, L. Peter, and D. Worsley, "Ultrafast near infrared sintering of TiO2 layers on metal substrates for dye-sensitized solar cells," *Prog. Photovolt. Res. Appl.*, vol. 19, no. 4, pp. 482–486.
[134] R. Rolli, M. Montagna, S. Chaussedent, A. Monteil, V. K. Tikhomirov, and M. Ferrari, "Erbium-doped tellurite glasses with high quantum efficiency and broadband stimulated emission cross section at 1.5 μm," *Opt. Mater.*, vol. 21, no. 4, pp. 743–748, Feb. 2003.
[135] H. Büning-Pfaue, "Analysis of water in food by near infrared spectroscopy," *Food Chem.*, vol. 82, no. 1, pp. 107–115, Jul. 2003.
[136] A. Deptuła, W. Łada, T. Olczak, A. Borello, C. Alvani, and A. di Bartolomeo, "Preparation of spherical powders of hydroxyapatite by sol-gel process," *J. Non-Cryst. Solids*, vol. 147–148, pp. 537–541, Jan. 1992.
[137] M. Vallet-Regí, M. T. Gutiérrez-Ríos, M. P. Alonso, M. I. de Frutos, and S. Nicolopoulos, "Hydroxyapatite Particles Synthesized by Pyrolysis of an Aerosol," *J. Solid State Chem.*, vol. 112, no. 1, pp. 58–64, Sep. 1994.
[138] M. G. S. Murray, J. Wang, C. B. Ponton, and P. M. Marquis, "An improvement in processing of hydroxyapatite ceramics," *J. Mater. Sci.*, vol. 30, no. 12, pp. 3061–3074, Jun. 1995.
[139] G. K. Lim, J. Wang, S. C. Ng, and L. M. Gan, "Processing of fine hydroxyapatite powders via an inverse microemulsion route," *Mater. Lett.*, vol. 28, no. 4, pp. 431–436, Oct. 1996.
[140] T. Hattori and Y. Lwadate, "Hydrothermal Preparation of Calcium Hydroxyapatite Powders," *J. Am. Ceram. Soc.*, vol. 73, no. 6, pp. 1803–1805.
[141] M. Yoshimura, H. Suda, K. Okamoto, and K. Ioku, "Hydrothermal synthesis of biocompatible whiskers," *J. Mater. Sci.*, vol. 29, no. 13, pp. 3399–3402, Jan. 1994.
[142] B. O. Fowler, "Infrared studies of apatites. I. Vibrational assignments for calcium, strontium, and barium hydroxyapatites utilizing isotopic substitution," *Inorg. Chem.*, vol. 13, no. 1, pp. 194–207, Jan. 1974.
[143] A. López-Macipe, R. Rodríguez-Clemente, A. Hidalgo-López, I. Arita, M. V. García-Garduño, E. Rivera, and V. M. Castaño, "Wet Chemical Synthesis of Hydroxyapatite Particles from Nonstoichiometric Solutions," *J. Mater. Synth. Process.*, vol. 6, no. 1, pp. 21–26, Jan. 1998.
[144] H. Tagai and H. Aoki, "Preparation of synthetic hydroxyapatite and sintering of apatite ceramics: Mechanical properties of biomaterials," *Chapter*, vol. 39, p. 213, 1978.
[145] M. Jarcho, C. H. Bolen, M. B. Thomas, J. Bobick, J. F. Kay, and R. H. Doremus, "Hydroxylapatite synthesis and characterization in dense polycrystalline form," *J. Mater. Sci.*, vol. 11, no. 11, pp. 2027–2035, Nov. 1976.
[146] J. Arends, J. Christoffersen, M. R. Christoffersen, H. Eckert, B. O. Fowler, J. C. Heughebaert, G. H. Nancollas, J. P. Yesinowski, and S. J. Zawacki, "A calcium hydroxyapatite precipitated from an aqueous solution: An international multimethod analysis," *J. Cryst. Growth*, vol. 84, no. 3, pp. 515–532, Sep. 1987.
[147] J. M. Thomann, J. C. Voegel, and P. Gramain, "Kinetics of dissolution of calcium hydroxyapatite powder. III: pH and sample conditioning effects," *Calcif. Tissue Int.*, vol. 46, no. 2, pp. 121–129, Feb. 1990.

[148] S. Raynaud, E. Champion, D. Bernache-Assollant, and P. Thomas, “Calcium phosphate apatites with variable Ca/P atomic ratio I. Synthesis, characterisation and thermal stability of powders,” *Biomaterials*, vol. 23, no. 4, pp. 1065–1072, Feb. 2002.

[149] M. Wakamura, K. Kandori, and T. Ishikawa, “Surface composition of calcium hydroxyapatite modified with metal ions,” *Colloids Surf. Physicochem. Eng. Asp.*, vol. 142, no. 1, pp. 107–116, Nov. 1998.

[150] A. Yasukawa, K. Gotoh, H. Tanaka, and K. Kandori, “Preparation and structure of calcium hydroxyapatite substituted with light rare earth ions,” *Colloids Surf. Physicochem. Eng. Asp.*, vol. 393, pp. 53–59, Jan. 2012.

[151] A. Yasukawa, K. Kandori, H. Tanaka, and K. Gotoh, “Preparation and structure of carbonated calcium hydroxyapatite substituted with heavy rare earth ions,” *Mater. Res. Bull.*, vol. 47, no. 5, pp. 1257–1263, May 2012.

[152] V. Stanić, S. Dimitrijević, J. Antić-Stanković, M. Mitrić, B. Jokić, I. B. Plećaš, and S. Raičević, “Synthesis, characterization and antimicrobial activity of copper and zinc-doped hydroxyapatite nanopowders,” *Appl. Surf. Sci.*, vol. 256, no. 20, pp. 6083–6089, Aug. 2010.

[153] C. S. Ciobanu, F. Massuyeau, L. V. Constantin, and D. Predoi, “Structural and physical properties of antibacterial Ag-doped nano-hydroxyapatite synthesized at 100°C,” *Nanoscale Res. Lett.*, vol. 6, p. 613, Dec. 2011.

[154] X. Li, J. L. Coffer, Y. Chen, R. F. Pinizzotto, J. Newey, and L. T. Canham, “Transition Metal Complex-Doped Hydroxyapatite Layers on Porous Silicon,” *J. Am. Chem. Soc.*, vol. 120, no. 45, pp. 11706–11709, Nov. 1998.

[155] C. Paluszkiewicz, A. Ślósarczyk, D. Pijocha, M. Sitarz, M. Bućko, A. Zima, A. Chróścicka, and M. Lewandowska-Szumieł, “Synthesis, structural properties and thermal stability of Mn-doped hydroxyapatite,” *J. Mol. Struct.*, vol. 976, no. 1, pp. 301–309, Jul. 2010.

[156] J. Terra, E. R. Dourado, J.-G. Eon, D. E. Ellis, G. Gonzalez, and A. M. Rossi, “The structure of strontium-doped hydroxyapatite: an experimental and theoretical study,” *Phys. Chem. Chem. Phys.*, vol. 11, no. 3, pp. 568–577, Jan. 2009.

[157] C. Capuccini, P. Torricelli, E. Boanini, M. Gazzano, R. Giardino, and A. Bigi, “Interaction of Sr-doped hydroxyapatite nanocrystals with osteoclast and osteoblast-like cells,” *J. Biomed. Mater. Res. A*, vol. 89A, no. 3, pp. 594–600.

[158] T. Ishikawa, H. Saito, A. Yasukawa, and K. Kandori, “Adsorption of CO2, CH3OH, and H2O on Fe(III)-Substituted Calcium Hydroxyapatites,” *Bull. Chem. Soc. Jpn.*, vol. 69, no. 4, pp. 899–907, Apr. 1996.

[159] O. Kaygili, S. V. Dorozhkin, T. Ates, A. A. Al-Ghamdi, and F. Yakuphanoglu, “Dielectric properties of Fe doped hydroxyapatite prepared by sol–gel method,” *Ceram. Int.*, vol. 40, no. 7, Part A, pp. 9395–9402, Aug. 2014.

[160] A. Tampieri, T. D’Alessandro, M. Sandri, S. Sprio, E. Landi, L. Bertinetti, S. Panseri, G. Pepponi, J. Goettlicher, M. Bañobre-López, and J. Rivas, “Intrinsic magnetism and hyperthermia in bioactive Fe-doped hydroxyapatite,” *Acta Biomater.*, vol. 8, no. 2, pp. 843–851, Feb. 2012.

[161] R. U. Mene, M. P. Mahabole, K. C. Mohite, and R. S. Khairnar, “Improved gas sensing and dielectric properties of Fe doped hydroxyapatite thick films: Effect of molar concentrations,” *Mater. Res. Bull.*, vol. 50, pp. 227–234, Feb. 2014.

[162] P. Kanchana, N. Lavanya, and C. Sekar, “Development of amperometric l-tyrosine sensor based on Fe-doped hydroxyapatite nanoparticles,” *Mater. Sci. Eng. C*, vol. 35, pp. 85–91, Feb. 2014.
[163] J. V. Rau, I. Cacciotti, A. De Bonis, M. Fosca, V. S. Komlev, A. Latini, A. Santagata, and R. Teghil, “Fe-doped hydroxyapatite coatings for orthopedic and dental implant applications,” *Appl. Surf. Sci.*, vol. 307, pp. 301–305, Jul. 2014.
[164] I. Fontana, A. Lauria, and G. Spinolo, “Optical absorption spectra of Fe2+ and Fe3+ in aqueous solutions and hydrated crystals,” *Phys. Status Solidi B*, vol. 244, no. 12, pp. 4669–4677.
[165] L. Podlowski, R. Heitz, P. Thurian, A. Hoffmann, and I. Broser, “Nonradiative transition rates of Fe2+ in III–V and II–VI semiconductors,” *J. Lumin.*, vol. 58, no. 1, pp. 252–256, Jan. 1994.
[166] P. Köhler and G. Amthauer, “The ligand-field spectrum of Fe3+ in garnets,” *J. Solid State Chem.*, vol. 28, no. 3, pp. 329–343, Jun. 1979.
[167] T. B. Nolan, “Chemistry of iron in water,” *US Geol. Soc.*, vol. Water Analysis, p. 39, 1962.
[168] A. J. C. Wilson, “Elements of X-ray Crystallography,” *ADDISON-WESLEY Publ. CO Read. MASS 1970 256 P*, 1970.
[169] B. D. Cullity, *Elements of X-ray Diffraction*. Addison-Wesley Publishing Company, 1978.
[170] A. F. Wells, *Structural Inorganic Chemistry, by A.F. Wells*. Clarendon Press, 1945.
[171] H. P. Klug and L. E. Alexander, *X-Ray Diffraction Procedures: For Polycrystalline and Amorphous Materials*. Wiley, 1974.
[172] J. M. Stutman, J. D. Termine, and A. S. Posner, “Vibrational Spectra and Structure of the Phosphate Ion in Some Calcium Phosphates*,†,” *Trans. N. Y. Acad. Sci.*, vol. 27, no. 6 Series II, pp. 669–675.
[173] K. Hadjiivanov and H. Knözinger, “Species formed after NO adsorption and NO+O2 co-adsorption on TiO2: an FTIR spectroscopic study,” *Phys. Chem. Chem. Phys.*, vol. 2, no. 12, pp. 2803–2806, Jan. 2000.
[174] W. P. Griffith, “Raman studies on rock-forming minerals. Part II. Minerals containing MO3, MO4, and MO6 groups,” *J. Chem. Soc. Inorg. Phys. Theor.*, vol. 0, no. 0, pp. 286–291, Jan. 1970.
[175] M. Hanesch, “Raman spectroscopy of iron oxides and (oxy)hydroxides at low laser power and possible applications in environmental magnetic studies,” *Geophys. J. Int.*, vol. 177, no. 3, pp. 941–948, Jun. 2009.
[176] P. Kubelka, “New Contributions to the Optics of Intensely Light-Scattering Materials. Part II: Nonhomogeneous Layers*,” *JOSA*, vol. 44, no. 4, pp. 330–335, Apr. 1954.
[177] P. Kubelka and F. Munk, “An article on optics of paint layers,” *Z Tech Phys*, vol. 12, no. 593–601, 1931.
[178] G. Kortüm, W. Braun, and G. Herzog, “Principles and Techniques of Diffuse-Reflectance Spectroscopy,” *Angew. Chem. Int. Ed. Engl.*, vol. 2, no. 7, pp. 333–341.
[179] E. L. Simmons, “Relation of the Diffuse Reflectance Remission Function to the Fundamental Optical Parameters,” *Opt. Acta Int. J. Opt.*, vol. 19, no. 10, pp. 845–851, Oct. 1972.

[180] V. S. Bystrov, C. Piccirillo, D. M. Tobaldi, P. M. L. Castro, J. Coutinho, S. Kopyl, and R. C. Pullar, "Oxygen vacancies, the optical band gap (Eg) and photocatalysis of hydroxyapatite: Comparing modelling with measured data," *Appl. Catal. B Environ.*, vol. 196, pp. 100–107, Nov. 2016.
[181] W. Low and G. Rosengarten, "The optical spectrum and ground-state splitting of Mn2+ and Fe3+ lons in the crystal field of cubic symmetry," *J. Mol. Spectrosc.*, vol. 12, no. 4, pp. 319–346, Apr. 1964.
[182] H. Füredi-Milhofer, V. Hlady, F. S. Baker, R. A. Beebe, N. W. Wikholm, and J. S. Kittelberger, "Temperature-programmed dehydration of hydroxyapatite," *J. Colloid Interface Sci.*, vol. 70, no. 1, pp. 1–9, Jun. 1979.
[183] H. C. W. Skinner, J. S. Kittelberger, and R. A. Beebe, "Thermal instability in synthetic hydroxyapatites," *J. Phys. Chem.*, vol. 79, no. 19, pp. 2017–2019, Sep. 1975.
[184] H. Owada, K. Yamashita, and T. Kanazawa, "High-temperature stability of hydroxyl ions in yttrium-substituted oxyhydroxyapatites," *J. Mater. Sci. Lett.*, vol. 10, no. 1, pp. 26–28, 1991.
[185] M. A. Larmas, H. Häyrynen, and L. H. Lajunen, "Thermogravimetric studies on sound and carious human enamel and dentin as well as hydroxyapatite," *Eur. J. Oral Sci.*, vol. 101, no. 4, pp. 185–191.
[186] M. Sneha and N. M. Sundaram, "Preparation and characterization of an iron oxide-hydroxyapatite nanocomposite for potential bone cancer therapy," *International Journal of Nanomedicine*, 01-Oct-2015. [Online]. Available: https://www.dovepress.com/preparation-and-characterization-of-an-iron-oxide-hydroxyapatite-nanoc-peer-reviewed-fulltext-article-IJN. [Accessed: 17-Jul-2018].
[187] C.-J. Liao, F.-H. Lin, K.-S. Chen, and J.-S. Sun, "Thermal decomposition and reconstitution of hydroxyapatite in air atmosphere," *Biomaterials*, vol. 20, no. 19, pp. 1807–1813, Oct. 1999.
[188] R. Menzel, *Photonics: Linear and Nonlinear Interactions of Laser Light and Matter*. Berlin Heidelberg: Springer-Verlag, 2001.
[189] J. M. Liu, "Simple technique for measurements of pulsed Gaussian-beam spot sizes," *Opt. Lett.*, vol. 7, no. 5, pp. 196–198, May 1982.
[190] M. Lenzner, J. Krüger, W. Kautek, and F. Krausz, "Incubation of laser ablation in fused silica with 5-fs pulses," *Appl. Phys. A*, vol. 69, no. 4, pp. 465–466, Oct. 1999.
[191] O. Armbruster, A. Naghilou, M. Kitzler, and W. Kautek, "Spot size and pulse number dependence of femtosecond laser ablation thresholds of silicon and stainless steel," *Appl. Surf. Sci.*, vol. 396, pp. 1736–1740, Feb. 2017.
[192] J. Ihlemann, B. Wolff, and P. Simon, "Nanosecond and femtosecond excimer laser ablation of fused silica," *Appl. Phys. A*, vol. 54, no. 4, pp. 363–368, Apr. 1992.
[193] X. Liu, D. Du, and G. Mourou, "Laser ablation and micromachining with ultrashort laser pulses," *IEEE J. Quantum Electron.*, vol. 33, no. 10, pp. 1706–1716, Oct. 1997.
[194] A. Cunha, A. P. Serro, V. Oliveira, A. Almeida, R. Vilar, and M.-C. Durrieu, "Wetting behaviour of femtosecond laser textured Ti–6Al–4V surfaces," *Appl. Surf. Sci.*, vol. 265, pp. 688–696, Jan. 2013.

[195] L. Ji, L. Li, H. Devlin, Z. Liu, J. Jiao, and D. Whitehead, “Ti:sapphire femtosecond laser ablation of dental enamel, dentine, and cementum,” *Lasers Med. Sci.*, vol. 27, no. 1, pp. 197–204, Jan. 2012.

[196] P. Kohns, P. Zhou, and R. Störmann, “Effective laser ablation of enamel and dentine without thermal side effects,” *J. Laser Appl.*, vol. 9, no. 3, pp. 171–174, Jun. 1997.

[197] A. D. Anastasiou, C. L. Thomson, S. A. Hussain, T. J. Edwards, S. Strafford, M. Malinowski, R. Mathieson, C. T. A. Brown, A. P. Brown, M. S. Duggal, and A. Jha, “Sintering of calcium phosphates with a femtosecond pulsed laser for hard tissue engineering,” *Mater. Des.*, vol. 101, pp. 346–354, Jul. 2016.